ABSTRACT

Title of Document: CHARACTERIZATION OF COPPER COVETIC BULK AND FILMS: COPPER WITH HIGH CARBON CONTENT

Romaine Isaacs, Doctor of Philosophy, 2016

Directed by: Professor Lourdes Salamanca-Riba
Department of Materials Science and Engineering

Incorporation of carbon nanostructures in metals is desirable to combine the strongly bonded electrons in the metal and the free electrons in carbon nanostructures that give rise to high ampacity and high conductivity, respectively. Carbon in copper has the potential to impact industries such as: building construction, power generation and transmission, and microelectronics.

This thesis focuses on the structure and properties of bulk and thin films of a new material, Cu covetic, that contains carbon in concentrations up to 16 at.%. X-ray photoelectron spectroscopy (XPS) shows C 1s peak with both sp^2 and sp^3 bonded C measuring up to 3.5 wt.% (16 at.%). High resolution transmission electron microscopy and electron diffraction of bulk covetic samples show a modulated structure of ≈ 1.6 nm along several crystallographic directions in regions that have high C content suggesting that the carbon incorporates into the copper lattice forming a network. Electron energy loss spectra (EELS) from covetics reveal that the level of graphitization from the source material, activated carbon, is maintained in

the covetic structure. Bulk Cu covetics have a slight increase in the lattice constant, as well as (111) texturing, or possibly a different structure, compared to pure Cu. Density functional theory calculations predict bonding between C and Cu at the edges and defects of graphene sheets. The electrical resistivity of bulk covetics first increases and then decreases with increasing C content.

Cu covetic films were deposited using e-beam and pulsed laser deposition (PLD) at different temperatures. No copper oxide or any allotropes of carbon are present in the films. The e-beam films show enhanced electrical and optical properties when compared to pure Cu films of the same thickness even though no carbon was detected by XPS or EELS. They also have slightly higher ampacity than Cu metal films. EELS analysis of the C-K-edge in the PLD films indicate that graphitic carbon is transferred from the bulk into the films with uniform carbon distribution. PLD films exhibit flatter and higher transmittance curves and sheet resistance two orders of magnitude lower than e-beam films leading to a high figure of merit as transparent conductors

CHARACTERIZATION OF COPPER COVETIC BULK AND FILMS: COPPER WITH HIGH CARBON CONTENT

by

Romaine Antonio Isaacs

Dissertation submitted to the Faculty of the Graduate School of the
University of Maryland, College Park in partial fulfillment
of the requirements for the degree of
Doctor of Philosophy
2016

Advisory Committee:
Professor Lourdes Salamanca-Riba, Chair/Advisor
Professor Min Ouyang
Professor Oded Rabin
Professor Marc Zupan
Professor Liangbing Hu

Dedication

Dedicated to my mother, Rosemarie Antonette...

Acknowledgments

I would like to thank my advisor, Professor Lourdes Salamanca-Riba, for her guidance throughout this project. Your ideas, insight and patience were valuable to me throughout this process. You gave me an opportunity to get in on the ground floor and study a new material that has a lot of potential and I am grateful for the time you spent teaching, reviewing and critiquing my work.

This project would not have been possible without the various funding agencies that made my tenure as a graduate student possible: MRSEC funding in 2011 and NIST-ARRA Fellowhip from 2012-2013. The University of Maryland funded this work in the beginning when external funding was not forthcoming. This allowed us to garner enough results to secure subsequent funding from DARPA, ONR and DOE-ANL.

Thanks to my dissertation committee: Prof. Min Ouyang, Prof. Salamanca-Riba, Prof. Liangbing Hu, Prof. Oded Rabin and Prof. Marc Zupan for your support and guidance when I needed it and for reading my dissertation.

The study of covetics was made possible by the inventions of Jason Shugart, Roger Shearer who developed the process to incorporate high amounts of carbon in metal lattices. The company they founded, Third Millennium Materials, including the executive team: Lou Luedtke, Harry Couch and Michael Braydich, provided insights into the processing and characterization of covetics. Thank you to these and other collaborators, without whose insights, ideas and hard work this thesis would not have been possible.

Characterization of covetics is quite challenging and it was not possible to do it alone. I relied on Dr. Azzam Mansour at NSWC who performed XPS, H. M. Iftekhar Jaim, M.S. who helped me with Raman and AFM, Dr. Joshua Schumacher and Valery Ray who assisted when I had challenging FIB lamellas, Dr. Sz-Chian Liou who helped me tune the GIF for EELS acquisition, Dr. Karen Gaskell for XPS deconvolution, Dr. Peter Y. Zavalij for XRD analysis, Dr. Sergey Rashkeev for DFT simulation and phonon density of state calculations, and Dr. Daniel Cole for KPFM measurements. For insights into transparent conductors and measurements I thank Jiayu Wan, Dr. Colin Preston, Dr. Hongli Zhu and Dr. Wenzhong Bao in the group of Prof. Liangbing Hu. The staff of the University of Maryland Nanocenter FabLab who kept the equipment running, especially Tom Loughran who made it possible to deposit e-beam films. Special thanks to Prof. Oded Rabin, who opened up his lab, and PLD chamber to help me deposit many PLD films.

To my colleagues and group members: Joshua Taillon who introduced me to Hyperspy for EELS analysis, H. M. Iftekhar Jaim and XiaoXiao Ge who also worked on covetics and shared their ideas. Thanks to my friend and computational physicist, Adam Iaizzi, who reviewed an early manuscript of my thesis and provided useful feedback. The extended group who also worked on covetics - Prof. Marc Zupan from UMBC who had new ways about thinking about results and for challenging me to think outside of the box. Dr. Rick Everett, Dr. David Forrest and Prof. Iwona Kasiuk, who provided insight, direction and shared their results.

To my mother, Rosemarie, who provided moral and financial support. You have always been supportive of my dreams, through good times and bad. You

listened to me talk about my work even though you are not a scientist; empathized when it was frustrating and celebrated when I had breakthroughs. You motivated me to keep going even when the road was rocky. I will be forever grateful to you.

Table of Contents

List of Figures viii

List of Abbreviations xii

1 Introduction 1
1.1 Background . . . 1
1.1.1 Carbon Nanostructures . . . 3
1.1.2 Carbon in Metals . . . 4
1.1.3 Metal-Carbon Nanostructures . . . 5
1.1.4 Cu-Carbon Nanostructures . . . 8
1.2 Cu Covetics . . . 11
1.2.1 Transparent Electrodes . . . 13

2 Experimental Approach 17
2.1 Overview . . . 17
2.1.1 Bulk Metal Fabrication . . . 18
2.1.2 Thin Film Fabrication . . . 18
2.1.3 Mechanical Polishing . . . 20
2.2 Characterization Techniques . . . 23
2.2.1 Transmission Electron Micropscopy . . . 23
2.2.1.1 Electron Energy Loss Spectroscopy . . . 26
2.2.2 X-ray Diffraction . . . 28
2.2.3 Atomic Force Microscopy . . . 29
2.2.4 X-ray Photoelectron Spectroscopy . . . 34
2.2.5 Time of Flight Mass Spectrometry . . . 36
2.2.6 Raman Spectroscopy . . . 37
2.2.7 Ellipsometry . . . 38

3 Incorporation of C into the Cu lattice 41
3.1 Characterization . . . 41
3.1.1 Modeling Bulk Cu covetics . . . 65
3.1.2 Electrical Properties of bulk Cu covetic . . . 73

4 E-beam deposited Films 76
4.1 Structural Characterization 76
4.1.1 Optoelectrical properties of e-beam deposited films 78
4.2 Improvement in Ampacity 88

5 Pulsed Laser Deposited Films 90
5.1 Fabrication 90
5.1.1 Structural Characterization 93
5.1.2 Electrical and Optical Properties of PLD Films 100

6 Conclusion 106
6.1 Summary 106
6.2 Future Work 108

Bibliography 111

List of Figures

1.1 Low carbon region of the Iron-carbon phase diagram 6
1.2 Low carbon region of the Copper-Carbon phase diagram (*31*) 9
1.3 (a) Average price of Indium in the decades up to 2008, (b) cracks in ITO film that can lead to increased electrical resistivity and eventual device failure. (*22*) 14

2.1 Schematic showing electron beam interaction with a sample in the TEM 25
2.2 Schematic of AFM apparatus.(*51*) 31
2.3 The XPS photoemission process whereby an incoming photon causes the ejection of a photoelectron.(*52*) 35
2.4 Raman spectroscopy of graphene showing the G peak emblematic of pristine graphite and D peaks which is observed at the edges of the graphene sheet.(*53*) 38
2.5 Schematic showing the J.A.Woollam Co. Inc. spectrometer.(*55*) . . . 39

3.1 Optical images of (a) an extruded Cu cv 3% sample cut to reveal the bulk structure, polished surface (b) 5x, (c) 10x, (d) 20x, (e) 50x and (f) 80x 42
3.2 (a) SEM-EDS spectrum of a Cu covetic bulk sample with nominally 5 wt.% C showing 3.67 wt.% ($\approx 15.32 \pm 0.7$ at.%) C (b) SEM secondary electron image of the region acquired, with mapping showing the presence of (b) Cu, (c) O, and (d) C with false color images overlaying the secondary electron image 44
3.3 XPS survey spectra of a Cu covetic and Cu metal sample showing atomic concentration of C 1s, O 1s and Cu $2p_{3/2}$ (a) before and (b) after sputtering. Depth profile of the (c) Cu metal and (d) Cu covetic samples showing average C concentration of 2 at.% ($\approx$ 0.38 wt.%) and 16 at.% ($\approx$ 3.5 wt.%) respectively after 50 min and 60 min of sputtering respectively. Photoemission spectra of the C 1s peaks after 30 minutes of sputtering of the (e) Cu metal and (f) Cu covetic samples with deconvolution 46
3.4 TOF-SIMS mapping and mass spectra of Cu and Cu cv 5% sample. . 50

3.5 XRD spectra of Cu cv 5%, 10% and 15% showing slightly increase in the lattice constant compared to bulk Cu and texturing in <111> . . 51
3.6 (a) Bright field TEM image of a sample with nominally 5 wt.% C in the Cu covetic bulk, (b) is the HRTEM image from the area shown in (a) showing a modulated structure. (c) Electron diffraction pattern from the modulated region, (d) EDS spectrum from the area in (a) . 54
3.7 EELS C K-edge spectrum of (a) different allotropes of C: diamond, amorphous C and graphite,(*58*) (b) single crystals of single walled CNTs formed by self-assembly.(*59*) 55
3.8 (a) HAADF image of Cu cv 5% bulk sample showing the regions where a spectrum image was obtained. (b) High magnification of spectrum image from the area shown in (a), (c) C K-edge after background subtraction of one pixel labeled 1 in (b) showing pre-peak at 285 eV and peak at 290 eV, (d) Gaussian fitting to edge in (c), (e) C-K edge of activated carbon fitted with Gaussian peaks 57
3.9 (a) EELS spectrum from a single pixel of the Cu M edge before decomposition, (b) Spectrum after PCA decomposition, (c) scree plot showing three principal components. 58
3.10 Decomposition of the C K-edge from the spectrum shown in Figure 3.8(b) resulting in the (a) signal space and (b) navigation space . . . 61
3.11 (a)SEM image of surface of a Cu cv 3% sample showing inclusions (b) Cross-section of the same sample showing that inclusions are persistent within the bulk, (c) Low magnification TEM image of lamella made from the same sample showing a few inclusions, (d) a single inclusion, elliptical in shape, measuring $\approx$ 830 nm $\times$1090 nm 62
3.12 HRTEM image of a region outside the inclusion. The inset of (a) is the $[1\bar{1}1]$ electron diffraction pattern from the same region, (b) HRTEM image of a region inside the inclusion with a d-spacing measuring 0.233 and 0.283. The inset of (b) is an electron diffraction pattern taken inside the inclusion. TEM-EDS spectrum of regions (c) outside and (d) inside the inclusion, showing 0 wt.% and 2.33 wt.% C respectively. 64
3.13 Decomposition of the C K-edge from the inclusion in the Cu cv 3% sample resulting in the (a) navigation space and (b) signal space . . . 65
3.14 (a) 2D model showing the graphene plane (yellow) superimposed on the B and C sites of the Cu (111) plane (blue), (b) 3D model showing the C atoms (blue) at the interstitial sites in the Cu (red) fcc lattice . 66
3.15 DFT model of the covetic supercell after relaxation to the lowest energy state 69

3.16 (a) Average Raman Spectrum from 20 points along a 300 μm line from Ag cv 6%, each spectrum is shown in the inset, (b) Average Raman spectrum from 10 points along a 400 μm line of a Cu cv 5% sample with each spectrum is shown in the inset, (c) Phonon Density of states shows a good fit with the experimental data acquired in (a), (d) Phonon density of states plotted with the experimental average data in (b) indicates the best fit occurs when only one layer of graphene nanoribbons is bonded to the top Cu plane. 71
3.17 Model of the Cu covetic generated using CrystalMaker®, (b) simulated electron difraction pattern from the structure in (a) using SingleCrystal™ 72
3.18 Electrical conductivity of Cu cv 3% and Cu metal wires as a function of temperature 75

4.1 (a) SEM-EDS of an 18 nm thick Cu cv 5% film deposited by e-beam on Si. (b) AFM of surface of the film with roughness ≈1 nm (c) cross section HRTEM image of a region within this film, (d) XRD spectrum of the same film displaying a crystalline structure with Cu [111] texture. 77
4.2 (a) HAADF survey image showing target region for EELS spectrum imaging in green and spectra sum in red, (b) integrated spectra of the target (red) region showing Cu M-edge, C K-edge and O K-edge, (c) Magnified spectrum image of target region. Maps of (d) Cu M-edge, (e) C K-edge, (f) O K-edge and (g) line profiles of the Cu, C and O respectively. 79
4.3 (a) Optical Image of 10 nm, 20nm and 30 nm e-beam Cu covetic films (b) Transmittance measurement comparing Cu metal (0% C) with e-beam nominal Cu cv 5% films of 10, 20 and 30 nm thickness. (c) Stability measurement comparing the resistivity of Cu metal with Cu cv 5% films in air. (d) Transmittance vs. sheet resistance of the e-beam covetic and Cu films measured at 550 nm 81
4.4 (a)Transmittance measurement comparing e-beam Cu cv 5% and Cu cv 15% films grown at room temperature, (b) Electrical stability measurement of the Cu cv 15% films grown at room temperature (25^0 C), (c) Transmittance measurement so Cu cv 15% films grown at 25^0 C and 350^0 C, (d) Electrical stability of the films Cu cv 15% films grown at high temperature (350^0 C). 84
4.5 AFM height and phase of a Cu cv 15% film grown at 350^0C measured over a three month period shows very little change in the height and phase contrast, indicating a stable structure. 86
4.6 Ellipsometry of Cu cv 5% and Cu metal e-beam films on Si substrate using the same B-spline model and the corresponding optical constants. 87
4.7 Current at thermal limit as a function of the sample width for 20 nm films. 89

5.1 AFM images comparing the grain structure in the height image (left column) the phase contrast (center column) and KPFM images (right column) mapping the surface potential of a Cu covetic and Cu metal sample 94
5.2 (a) X-ray diffraction of the Cu cv 4% films grown via PLD described in table 3, (b) XPS of film (7) showing 0.55 wt.% (2.87 at.%) C concentration in the film region, with the inset showing the C 1s peak. 96
5.3 (a) Low resolution image of a TEM cross section lamella made using FIB, (b) TEM bright field image of the Cu cv 4% PLD film (7) measuring 21.16 nm on Si (100) with Pt protection layer, (c) HRTEM of film and substrate, (d) nanodiffraction from film region. 97
5.4 (a) HAADF survey image showing target region for EELS spectrum imaging in green and region for spectra sum in red, (b) Magnified HAADF image of target region, (c) spectrum image of the target region in the energy range of the C K-edge, (d) integrated spectra from region highlighted in red after background subtraction, (e) Line profile across the scanned region, (f) C K-edge distribution in scanned region. 99
5.5 Decomposition of the Spectrum image of Film 7 using Blind Source Separation, shows three clear regions in the navigation and signal spaces: background, C contamination and C from the covetic film region. 101
5.6 (a) TEM bright field image of a cross section lamella of the Cu cv 4% PLD film (8) made using FIB measuring 50.23 nm (b) Diffraction from film region including some of the substrate, (c) EELS spectrum from the film after background subtraction. 102
5.7 (a) Transmittance of Cu cv 4% PLD films, (b) Stability measurement of Cu cv 4% - Film 8, (c) Figure of Merit comparing Cu covetic films with various materials.(*36*),(*37*),(*3*),(*4*),(*47*),(*88*),(*78*) 104
5.8 (a) Spectroscopic data of Cu coveitc film (8) deposited by PLD, (b) derived optical constant from the data in (a) 105

List of Abbreviations

AFM	**A**tomic **F**orce **M**icroscopy
BSS	**B**lind **S**ource **S**eparation
CNT	**C**arbon **N**anotube
CVD	**C**hemical **V**apor **D**eposition
EDS	**E**nergy **D**ispersive x-ray **S**pectroscopy
EELS	**E**lectron **E**nergy **L**oss **S**pectroscopy
FIB	**F**ocused **I**on **B**eam
KPFM	**K**elvin **P**robe **F**orce **M**icroscopy
MVA	**M**ulti **V**ariate **A**nalysis
PCA	**P**rincipal **C**omponent **A**nalysis
PLD	**P**ulsed **L**aser **D**eposition
SEM	**S**canning **E**lectron **M**icroscopy
SIMS	**S**econdary **I**on **M**ass **S**pectroscopy
TEM	**T**ransmission **E**lectron **M**icroscopy

Chapter 1: Introduction

1.1 Background

Copper is an essential component in motors for wiring, radiators, connectors, brakes, and bearings used in vehicles, communication equipment and power generation. Any improvement in the electrical and/or thermal properties of copper could have wide ranging implications as losses in high voltage transmission lines alone can be calculated in the billions of dollars. Additionally, the ubiquity of copper in consumer electronic devices, which use copper wire as conductors would mean lower power demands and higher efficiency if the electrical, thermal and mechanical properties of copper are improved.

Conductors must be able to transmit electrical power or data signals with minimal loss. The material properties used in these conductors are of critical importance to their performance. In high-tension power cables, the tensile strength and stability of the material are important factors to withstand high thermal loads. High-tension wires are typically made from an aluminum alloy with steel reinforced cores. In data servers, cables made from Cu are used to transmit data with high carrier frequencies. Cu is also used in interconnects in integrated circuits within servers.(*1*),(*2*) An interconnect in an integrated circuit (IC) distributes clock and signal, as well as

provides a path for the current and ground. Its performance is determined by the current-carrying capacity, resistance, inductance and capacitance.(*2*) Engineering solutions have made it possible for Cu to be used in IC interconnects in a layered structure,(*1*) but problems with exposed Cu persist, especially as dimensions shrink due to the high propensity of copper to oxidize when exposed to the environment.

In aerospace and naval applications, cabling is used for communication systems, power supply and navigation. NASA has been on a mission to improve the payload and fuel efficiency of aircraft. Since cabling is a major component of the total mass of aircraft, any substantial improvements in the ampacity would aid in achieving this goal. On naval ships and aircraft carriers corrosion due to the sea salt environment presents a unique challenge. In these environments, reliability is important, and conductors must be able to withstand large changes in pressure and temperature without large variations in resistivity. Cu conductors face some challenges in this regard. They have limitations such as poor cycling fatigue, lower electrical conductivity as temperature increases. Hence, there is great demand for an electrical conductor that has >50% higher conductivity per mass and superior mechanical properties than comparable rated Cu wires, particularly when operating at high temperatures (500^0 - 600^0 F). In addition to electrical conductivity new conductors must also have high strength, low AC loss characteristics and be rugged enough for real world applications where corrosion, wear and tear and other factors are a reality. Volume density is also crucial, since a new conducting wire could be lighter, with equal resistivity but have a large diameter or cross section compared to Cu, which would increase the weight of insulation coating.

1.1.1 Carbon Nanostructures

Recent developments of carbon-based conductors, carbon nanotubes (CNTs) and graphene, have shown superior properties to traditional conductors like Cu. (*3*)(*4*)(*5*)(*6*) CNT's have current carrying density of $\approx 4 \times 10^9 A/cm^2$, three orders of magnitude higher than Cu. A cable made of CNTs could reduce traditional cable mass per unit length by up to 50%. They have also been able to withstand >200,000 bending cycles without increase resistivity, and exhibit no increase resistivity after 80 days in a corrosive environment.(*7*) The major challenge with CNTs is the inability to produce bulk quantity with suitable purity in a reproducible manner. CNTs suffer from lower conductivity than traditional conductors like Cu. Wires made from CNTs have shown electrical conductivities of up to $3 \times 10^4 S/m$,(*6*) but this is an order of magnitude below the conductivity of Cu metal (5.8×10^5 S/cm). Further improvements in CNT growth would make such wires a true contender for a new class of commercial electrical conductors.

Another form of carbon with impressive properties is graphene. It has high electron mobilities $\approx 1500\ cm^2V^{-1}s^{-1}$, low resistivity $\approx 10^6$ Ohm-cm and high optical transmittance (95% for 2 nm thick film).(*8*) Fabrication and performance of graphene has improved steadily over the past decade. Bae et. al. have demonstrated large scale roll-to-roll production of graphene grown on flexible Cu substrates with sheet resistance of $\approx$ 125 Ohm/sq with 97.4% optical transmittance and layer by layer stacking to fabricate a HNO_3 doped four layer film with 30 Ohm/sq at 90% transmittance.(*4*) Khrapach et. al. have intercalated $FeCl_3$ into few layer graphene

(FLG) to achieve sheet resistance of 8.8 Ohm/sq with an optical transmittance of 84%. $FeCl_3$ enhances the electrical conductivity of FLG while maintaining the high optical transparency of graphene.(*3*) The challenge of graphene has been maintaining the high electrical conductivity at large scale. With further improvements, graphene based materials could be the likely replacement for ITO as a transparent conductor.

1.1.2 Carbon in Metals

Incorporating carbon in the lattice of metals can improve the performance of the base metal. There are three main ways to accomplish this: metal carbide formation, nanocarbon catalysis reactions and metal-nanocarbon composite formations. The resulting mixture can exist as a compound e.g. Fe_3C, an alloy or a composite. In a compound, such as Iron carbide, the arrangement of the atoms occurs in a fixed stoichiometry and forms a stable structure. An alloy forms when there is local order for a range of concentrations of the two (or more) elements in the alloy. In a composite, the two components are phase separated and may form particles. In steel, iron and a small amount of carbon (1 - 2 wt.%) are mixed and form various phases as shown in Figure 1.1. Carbon increases the strength of the base metal by preventing the atomic planes of the metal from slipping under stress or strain. The precise amount of carbon in steel is quite important; too low concentration and the alloy becomes soft and weak, too much and it becomes brittle. As the carbon content increases the ductility, strength and hardness changes. Therefore, the solubility

of C in the metal is very important. $\alpha - Fe$ (BCC structure) can only accommodate 0.022 wt.% of carbon, while the $\gamma - Fe$ (FCC structure) has a solubility limit of 2.14 wt.%. Due to the impressive results obtained by incorporating carbon in iron and wide industrial applications of steel, researchers have sought to exploit the possibility of incorporating carbon into other metals that would result in the possible formation of new carbides or metal-carbon alloys. However, since the discovery and isolation of graphene, (*9*)(*10*)(*11*)(*12*) the development of fabrication techniques have produced new designs that allow for the incorporation of nanocarbon structures into metals. (*13*)(*14*)(*15*)(*16*) These metal-nanocarbon composites aim to enhance the properties of metals by incorporating the superior strength electrical and thermal conductivity of carbon nanostructures into the metal. The expectation is that the resulting structure will maintain or even enhance the properties of the metal-carbon composite. Metal-CNTs (*5*)(*17*) and metal-graphene (*8*)(*18*)(*19*) composites have been attempted, but the main challenge is to create a homogeneous structure where the carbon resides in the metal matrix without migration or precipitation. These designs have yet to prove commercially viable because traditional fabrication techniques such as roll-to-roll or sintering process would destroy the composite structure.

1.1.3 Metal-Carbon Nanostructures

Carbon can bond to metals during nanocarbon catalysis reactions. Nanocarbon structures such as carbon nanotubes (CNT) and graphene have been grown

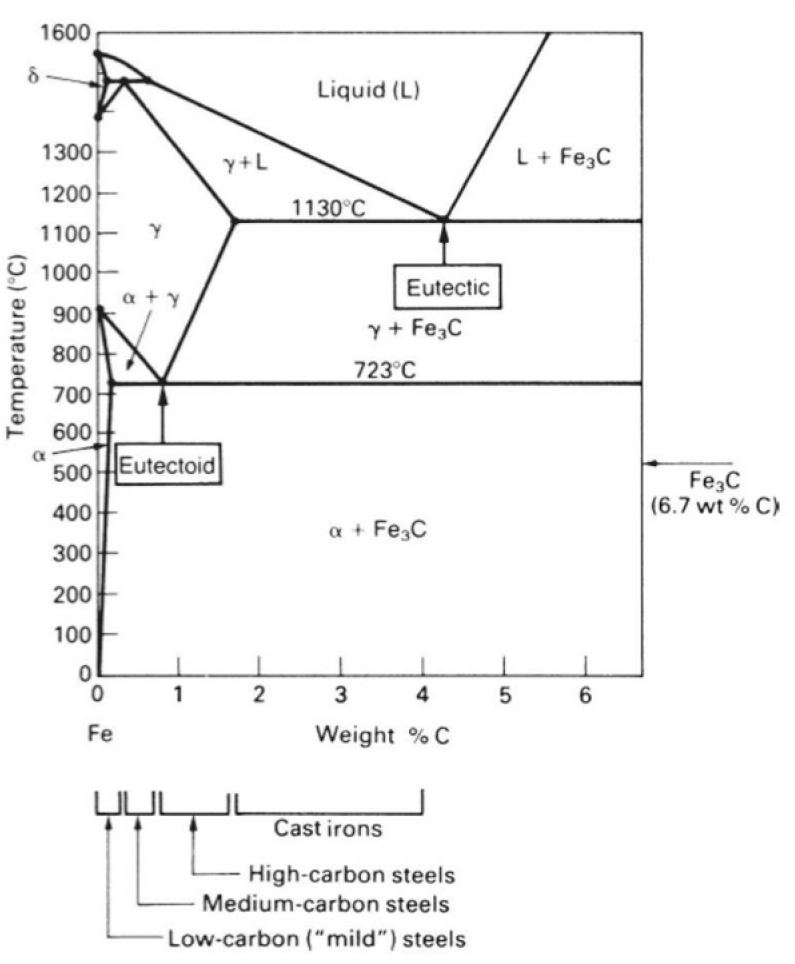

Figure 1.1: Low carbon region of the Iron-carbon phase diagram

Dr. Ali Salami Golezani - `http://kiau.ac.ir/~materialsscience/index_files/6-Iron\%20\&\%20Steel.pdf`

on metals using chemical vapor deposition(CVD).(*4*)(*13*)(*15*)(*20*)(*21*)(*22*)(*23*) In CVD, a hydrocarbon precursor undergoes a catalytic decomposition using a transition metal. At elevated temperatures carbon is soluble in most transition metals. The most effective transition metals Cu,(*13*)(*23*) Co, Ni,(*24*) and Fe act as catalysts by facilitating the decomposition of volatile carbon compounds. These metals are also known to form metastable carbides and carbon is able to diffuse over the surface and into the metal quite rapidly. The formation of nanocarbon structures occurs via different mechanisms depending on the metal used. In the case of Ni, the carbon dissolves into the metal to form a solid solution and upon cooling precipitates to the surface as a continuous film of highly crystalline graphite with the graphite basal planes oriented parallel to the substrate surface. Though the mechanism is similar for CNT and graphene growth, the form of carbon produced depends on the physical dimensions of the catalyzed reactions.(*25*) Instead of metal foils used in the growth of graphene, metal particles with spherical or pear shaped geometry can be used to produce CNTs.

The CVD of graphene on copper is done under low (0.5 - 50 Torr) or atmospheric pressure of methane and hydrogen gas mixture in various ratios. The growth mechanism on Cu is surface related, but not due to diffusion from the bulk.(*23*) Cu is usually annealed in hydrogen to remove copper oxide, but annealing also has the side effect of increasing grain growth and removing surface defects from a Cu foil. Once the methane is added, uniform nucleation of graphene islands on the Cu surface occurs, where initial graphene domains may have different lattice orientations depending on the orientation of the Cu grains. As time progresses the domains in-

crease and coalesce into a continuous film. Due to the very low interaction between Cu and C the reaction is self-limiting to one monolayer. Cu is a unique catalyst for growing graphene because Cu has closed d-shells and strong free electron-like surface states, has low solubility to C and high catalytic activity from hydrocarbons.

It is of paramount importance to understand the structure and properties of any new alloy or composite. In the case of metal-carbon nanostructures, first principles studies conducted by Gong et, al.(*26*) show that graphene can bond to metal surfaces in predominantly two ways depending on the metal: physisorption or chemisorption. In physisorption the metal substrate and graphene do not form a chemical bond at the interface, but charge transfer takes place while preserving graphene's pi-bond structure. In chemisorption, the interface forms a metal carbide bond that disturbs graphene's electronic structure and forms a hybridized bond between the metal's d-orbital and graphene's pi-orbital. Additionally, graphene can be doped when in contact with a metal. For example, copper, work function (WF) $\approx$ 5.2 eV, has been shown to n-dope graphene, WF $\approx$ 4.6 eV, via Pauli repulsive interaction and electron transfer.(*19*)

1.1.4 Cu-Carbon Nanostructures

There are several advantages to developing metal-carbon composites. Carbon allotropes, such as graphene and CNTs, have been combined with metals to be used as electrodes in lithium batteries,(*17*) heat exchangers in semiconductor devices,(*27*) supercapacitors,(*28*) tribological coatings in fuel cells,(*29*) and as magnets and su-

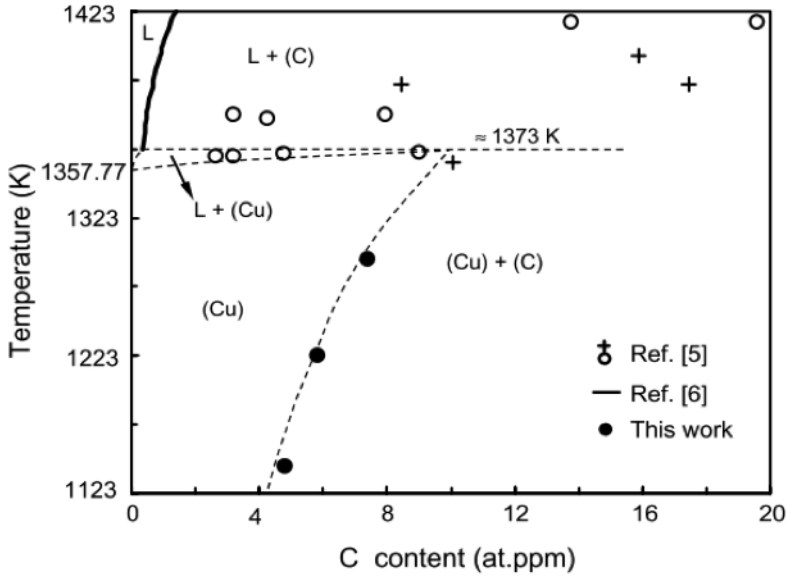

Figure 1.2: Low carbon region of the Copper-Carbon phase diagram (*31*)

perconductors.(*30*) Cu has been of great interest for the formation of metal-carbon composites and carbides in some of these applications as well, but until recently it has had limited success due to the low solubility of C in Cu, which lies in the range of parts per million as shown in Figure 1.2.(*25*) Additionally, Cu-C composites have faced challenges because of the weak adsorptions energies on low dimensional carbon allotropes such as CNTs and graphene; but novel solutions such as those employed by Gong et. al. have shown that it is possible to increase the binding energy of the Cu-graphene interface by 60% by using Pt as the third metal in a metal-graphene-metal sandwich.(*19*)

Graphene can also be used to reinforce soft metals like Cu. Using a technique where dissolution of carbon in a molten metal at a specified temperature and then allowing the dissolved carbon atoms to nucleate and grow on top of the melt at

a lower temperature, Amini et. al. (*24*) have been able to grow a few layers of graphene on molten Cu. In order to achieve uniform distribution throughout the surface a powdered C source is used and in some cases metal particles are added to carbon nanotubes. Despite these advances, there are many challenges involved to get graphene to disperse in metal matrix to form composites with existing conventional metallurgical processes, due to the large density difference between graphene and the metal matrix.(*8*)

Cu-CNT composites have also been used to enhance the mechanical properties of metals.(*17*) Yang et. al. have used a composite containing single walled CNTs to reinforce Cu, improving the micro-hardness of pure Cu while maintaining the electrical conductivity using electrodeposition under and ultrasonic field.(*32*) This technique improves the interfacial adhesion between the CNTs and the Cu matrix, overcoming the intrinsic van der Waal forces among CNTs that always lead to agglomeration and cause the decrease in the conductivity of Cu. Uniform distribution can lead to improved properties, while agglomeration leads to only local improvement and overall reduced performance.

The potential to improve the electrical properties of metals is great. In general, C incorporation in a metal reduces the conductivity of the metal, however with the introduction of graphene and CNTs structures, it may be expected that the overall conductivity will increase since their conductivities are higher than copper. Small amounts of carbon in Cu-graphene composites have already been shown to exhibit good thermal, electrical and mechanical properties in comparison with other Cu-based metal matrix composites and have been considered as replacements for Ag

contacts in electronics.(*33*)(*34*)

1.2 Cu Covetics

Due to the challenges associated with Cu-C composites, there have been ongoing efforts to study different ways to incorporate C in the Cu structure to realize the many potential advantages that such a material could provide. We investigate the structure and properties of a new material formed by the incorporation of carbon in concentrations up to 16 at.% into the crystal structure of copper that we refer to as Cu covetic. "Covetics" are a new class of materials formed by the incorporation of high concentrations of nanoscale carbon embedded in a metal matrix.(*35*) The carbon does not phase separate after subsequent melting and re-solidification despite the absence of a predicted solid solution at such high concentrations in the binary phase diagram.(*31*) The high carbon in Cu covetic could enhance many important properties of the copper host and result in a material that can replace copper in many applications. Cu covetic bulk material can also be sintered into a powder or deposited into a film for applications at the nanoscale.

In this thesis we investigated whether carbon is present in Cu covetic bulk samples by comparing it to the base material, Cu metal (Chapter 3). We used SEM-EDS to study the size and distribution of carbon regions in Cu covetics. Given the challenges associated with hydrocabron contamination at the surface, we found that SEM-EDS was not a sufficient technique for reliably measuring the carbon content in Cu covetic. XPS, a system with high vacuum and the ability to sputter below the

surface, was used to provide a more reliable measurement of the carbon content in Cu covetic. We found that the C 1s photoemission spectra is persistent deep into the bulk of Cu covetic and at much higher levels than the base metal, by sputtering away the surface hydrocarbon contamination. Once we identified the presence of carbon in Cu covetic samples, we sought to elucidate how the carbon incorporated using XRD. No allotropes of carbon were found, but there was a slight increase in lattice constant and texturing in the (111) crystallographic direction, which suggested a change in the structure. In order to further investigate the source of the texturing we used electron diffraction and high resolution TEM. Our results show that carbon is not uniformly distributed in these samples, but in regions where carbon is present there is modulation in the structure and an increase in the interplanar distance (d-spacing). Electron diffraction patterns from these regions show new reflections not associated with Cu metal or any of its oxides (Chapter 3). In order to understand the form of carbon and its bonding in Cu covetic, we acquired EELS data from these regions in scanning TEM mode. A C K-edge with a fine edge structure is clearly identified, which is comprised of features indicative of transitions from the 1s to π^* anti-bonding unoccupied orbital of carbon, which are known to be strongest in graphene-like carbon. This finding is corroborated by deconvolution of the C 1s photoemission spectra which indicated up to 35% sp^2 bonded C in Cu covetic (Chapter 3).

Given that Cu metal is a good conductor, and carbon typically reduces the conductivity of metals, we sought to investigate the effect of carbon incorporation on the properties of Cu covetic (Chapter 3.1.1). As such, the conductivity of bulk

Cu covetic drawn into wires were measured. We found that the conductivity first decreased then increased with the nominal carbon content, slightly surpassing the conductivity of Cu metal at nominally 9%. Cu cv 9% bulk samples were measured to have 2.42 wt.% C and 15% sp^2 C by XPS. Copper is a cheap and ubiquitous metal, and would be a good candidate for a transparent conductor, but its electrical properties are compromised as dimensions shrink due to oxidation. Therefore, we investigated the extent to which Cu coveitc could overcome this challenge, and its suitability as a transparent conductor by depositing thin films using bulk Cu coveitc as a target (Chapter 4).

1.2.1 Transparent Electrodes

Transparent conducting electrodes are a critical component in optoelectronic applications such as displays, solar cells, and touch screens.(*22*) Transparent electrodes are traditionally made of either conductive polymers or transparent conducting metal oxides (TCOs). The current TCO commercial industry standard, indium tin oxide (ITO) has a sheet resistance of 10 Ohm/sq and optical transparency of $\approx 90\%$. (*3*)(*4*)(*36*)(*37*)(*38*) ITO can also be applied at relatively low temperatures compared to other TCOs, and it is easier to etch than materials with comparable conductivities and transmittances. Its primary limitation is that it is too brittle for many device applications, such as flexible displays, because it easily breaks under 2-3% strain.(*4*)(*22*) Any micro cracks that develop from repeated use of devices containing ITO can propagate leading to a sharp decrease in the film's electrical

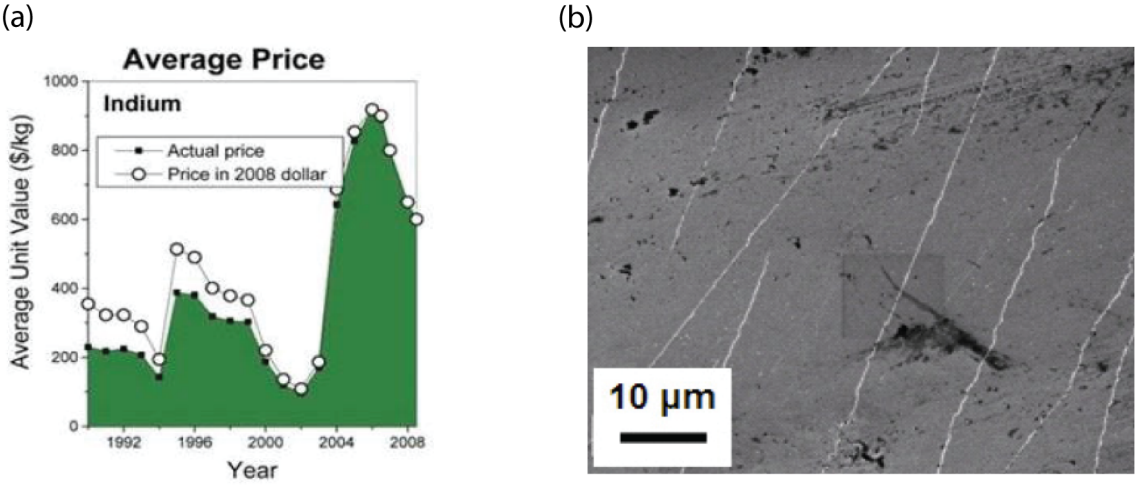

Figure 1.3: (a) Average price of Indium in the decades up to 2008, (b) cracks in ITO film that can lead to increased electrical resistivity and eventual device failure. (*22*)

conductivity. This places a limitation on the durability of the devices. ITO also has a high index of refraction, which leads to unwanted reflections and as such an anti reflective coating has to be added to devices to alleviate this problem, which in turn increases cost. ITO is comprised of 75% indium, which is a rare (occurring naturally at concentrations of 0.05 parts per million) (*36*) and expensive element.(*22*) Price fluctuation and increased demand has pushed for the development of alternative TCOs (seen Figure1.3). By comparison Cu is 1000x more abundant than indium and 100x time less expensive, making it an attractive candidate to replace ITO.(*36*)

Graphene has been proposed as a replacement for ITO because it can resist up to 6% strain (20% for single layer graphene).(*4*) Metal nanostructures may also be used to form transparent conductors with higher performance and better mechanical stability than ITO,(*39*)(*40*)(*41*) but with lower material and manufac-

turing costs. Metal nanostructures such as silver nanowires,(*39*)(*42*)(*43*)(*44*) gold nanowires,(*45*)(*46*) and recently copper nanowires are demonstrated to be excellent potential candidates for replacing ITO electrodes; however, there are still issues that prevent them from being used in practical applications, primarily production cost and scalability. Cu nanowires are particularly attractive due to their low cost and high conductivity; (*4*)(*22*)(*36*)(*39*)(*47*)(*48*) however, copper exhibits poor environmental stability. The long term stability of exposed copper does not yet meet the standard for practical applications.(*37*) though core-shell structures or atomic layer deposition coatings on Cu nanostructures have demonstrated reduced oxidation.(*38*)

We deposited thin films (10 nm - 30 nm) of Cu covetic using e-beam deposition and a Cu covetic target with nominally 5% C (measuring 1.2 wt% C by XPS). Despite not measuring an appreciable amount of C in these film by XPS, our results (Chapter 4) show that Cu covetic e-beam films exhibit higher optical transparency with better electrical conductivity that are more stable in environmental conditions than Cu metal films of the same thickness. We infer that C present below the detectability limit of XPS gives rise to these improvements. In an attempt to increase the carbon concentration, we deposited films using PLD at powers that are higher than can be achieved with e-beam deposition. PLD is known to transfer ions, molecules and larger structures in the ablation process. As such, we sought to employ this method to transfer the structures we observe in the bulk into thin films. Cu covetic PLD films made from nominally 4% target show uniform integration of carbon in these film (Chapter 5), with some modulation, but inclusions observed in bulk samples are not present in these films. These films show up to 4.1 $\pm$ 0.6

wt.% C by XPS, which indicate that under the right conditions PLD can transfer the same concentration of C from the bulk to the films. We observe evidence of sp^2 carbon in PLD Cu covetic films and a peak in the C K-edge in EELS indicative of transitions from 1s to π^* anitbonding unoccupied state similar to that observed in bulk samples, suggesting that the C transferred is graphitic in nature. It is apparent that the high electron mobility of the graphitic structures that form in the Cu lattice enhances the charge transport in the covetic structure without being hindered by highly resistive sites typical of carbon nanostructure films. We measure electrical resistivity two orders of magnitude lower in PLD Cu covetic films than e-beam films of the same thickness. Cu covetic films show good promise as transparent electrodes.

Chapter 2: Experimental Approach

2.1 Overview

Bulk Cu covetic was fabricated by Third Millennium Materials, LLC and prepared for analysis using mechanical polishing. Thin films were fabricated using the as received material as targets in pulsed laser deposition (PLD) and e-beam deposition. X-ray diffraction (XRD) and Transmission Electron Microscopy (TEM) were used for structural analysis of bulk and film samples. Scanning Electron Microscopy (SEM) was used to investigate the surface morphology and uniformity of the carbon distribution which was measured using Energy Dispersive x-ray Spectroscopy (EDS) mapping. Atomic Force Microscopy (AFM) was employed to measure grain size and surface roughness of the copper covetic films. Chemical composition was determined using X-ray Photoelectron Spectroscopy (XPS) and Electron Energy Loss Spectroscopy (EELS). Raman Spectroscopy was used to study carbon bonding in the structure. The electrical properties were measured using a 4-point probe station and optical measurements made using a UV-VIS spectrometer.

2.1.1 Bulk Metal Fabrication

Cu (99.99%) was converted to Cu covetic by adding 3, 4, 5, 9, 10 or 15 wt.% C to Cu by Third Millennium Materials, LLC (e.g. 5 wt.% C in Cu is denoted Cu cv 5%). The conversion process involves melting ($> 1085^0$ C) the metal in an induction furnace and stirring in the desired i.e. 5 wt.% (21.78 at.%) particles of activated carbon with diameter of $\leq 50\ \mu m$ to the liquid metal. A high DC current, ≈ 150 A, is applied to the mixture via graphite electrodes from an arc welder, creating a localized plasma arc.(*49*) The arc initiates a polymerization reaction by ionizing C to C^{n+} or C^{n-}. These carbon ions react with each other and with melted copper atoms forming C-C and Cu-C bonds, in a networked structure. The material is allowed to cool in an argon blanket to prevent oxidation. This process of bonding C to Cu is preserved under cooling and further re-melting and re-solidification.

2.1.2 Thin Film Fabrication

Two deposition techniques were used to deposit copper covetic films: e-beam deposition and pulsed laser deposition (PLD). For e-beam deposition, bulk Cu cv 5% or pure Cu metal, 99.99% (0% C) was used as the target from which material was transferred to Si and glass substrates using a Denton e-beam evaporator. Si purchased from University Wafer was p-type, Boron doped with orientation (100) $\pm$ 0.5 degrees, thickness 380 μm, and resistance of 1 - 10 Ohm-cm. Si (111) wafers had similar properties to Si (100), but a lower resistivity of 0.004 - 0.005 Ohm-cm. The target was placed in a Molybdenum crucible and the substrate mounted at the

top of the chamber in the Denton e-beam evaporator. The chamber was evacuated to a base pressure of $\approx 5 \times 10^{-6}$ Torr. Once the base pressure was achieved a voltage of 8 kV current of 90 - 130 mA were applied; causing electrons to bombard the target until it reached its melting point. The current was adjusted such that the evaporation rate was 0.2 - 0.3 nm/sec. The shutter covering the substrate was then removed allowing material to be deposited on its surface. For some of the depositions the substrate was heated to 500^0 C before deposition commenced.

For PLD film growth the target material was transferred into a thin film using a Blue Wave Semiconductor PLD system, employing a Quantel Brilliant B solid-state Nd:YAG pulsed laser (400 mJ/pulse @ 532 nm, 10 Hz) at powers ranging from $1.8 - 3.55W \pm 0.5W$.(*50*) Evaporation takes place in an Ar (99.9999%) atmosphere with $\leq$ 10 ppb O_2 and $\leq$ 20 ppb H_20, $\leq$ 100 ppb THC, $\leq$ 5 ppb N. Once the base pressure of $\approx 1 \times 10^{-6}$ Torr is reached, the Ar gas was flowed at a rate of 3 sccm. to achieve a deposition pressure of 100 mTorr and the substrate was heated to the desired temperature ranging from 150^0 - 500^0 C. The rotating target was ablated for 1 minute prior to deposition after which the film was deposited on either Si (100), glass and/or quartz substrates for times ranging from 20 - 64 minutes. Glass and quartz slides were purchased from Ted Pella Inc, where the latter is a high purity GE124 quartz that is amorphous and has been fused into a glassy material. Quartz slides had electrical resistivity of 7×10^7 Ohm-cm at 350^0 C and were suitable for high temperature environments up to 1250^0 C. After the deposition the samples were cooled to room temperature in 100 sccm argon gas. Films with various thicknesses of Cu covetic and Cu metal (0% C) were deposited for comparison.

2.1.3 Mechanical Polishing

Bulk Cu covetic and pure Cu samples, were cut from the as cast bulk copper and polished for Scanning Electron Microscopy (SEM) and X-ray photoelectron spectroscopy (XPS) in an iterative process using a platen polishing wheel. The sample was mounted to a TEM thinning fixture which was first place on a hot plate at 150^0 C and hot mounting wax was applied to the surface of the thinning fixture. The sample was placed on the wax on top of the fixture and a level used to ensure accurate alignment. This ensures that the sample surface is parallel to the grinding plane, resulting in a uniform thickness across the sample as it is thinned. The sample was ground and polished using an Allied polishing wheel to ensure a flat surface.

It was necessary to avoid using abrasives that contain carbon to prevent cross contamination of the samples. As such, the samples were polished with a series of aluminum oxide lapping films: 30 μm, 12 μm and 9 μm as presented in Table 2.1. Red Lube, a viscous glycol based lubricant, was used with the lapping films instead of water to reduce surface tension, dissipate heat and improve surface finish. Intermediate polishing was performed with 3 μm aluminum oxide polishing solution and 1 μm deagglomerated alumina suspension on separate DiaMat polishing cloth. DiaMat is a medium-nap, woven wool cloth, which provides good edge retention and surface finish on a wide variety of materials. Deagglomerated alumina suspensions are chemically stable, premixed formulas and are ideal for polishing of metallographic specimens. Final polishing was performed with 0.04 μm colloidal silica suspension, with the addition of hydrogen peroxide (H_2O_2) as an attacking agent.

Table 2.1: Procedure for Polishing Cu metal and Cu covetic bulk samples

Step	1	2	3	4	5	6
Abrasive Size (μm)	30	12	9	3	1	0.04
Type	Aluminum Oxide	Aluminum Oxide	Aluminum Oxide	Aluminum Oxide	Deagg. Alumina	Colloidal Silica
Carrier	Lapping Film	Lapping Film	Lapping Film	Solution	Suspension	Suspension
Polishing Cloth	-	-	-	DiaMat	DiaMat	Final A
Lubricant	RedLube	RedLube	RedLube	-	-	Water*
Platen Speed (RPM)	150	125	75	200	200	200
Target/ Time	Bulk removal (until flat)	Remove 90 μm	Remove 36 μm	2 mins	2 mins	3-5 mins

* Water is only used to pre-soak and rinse the cloth after use

The chemicals from the colloidal silica suspension and H_2O_2 remove the smeared layer on the surface and reveals the true, unaffected metal underneath. H_2O_2 (30% strength) was mixed into the colloidal silica suspension, at 10% H_2O_2 by volume, to enhance the suspension's oxidizing power. This mixture was used on Final A polishing cloth, which is a low nap cloth that produces a smooth, artifact-free condition for most materials; it also has good chemical resistance, which makes it an ideal cloth for polishing. After each grinding and polishing step, the sample and fixture were cleaned with micro organic soap to remove debris and abrasive particulates, and rinsed with water. After polishing, the sample was sonicated in isopropyl alcohol and then dried using compressed air spray. This reduces the likelihood of scratches on the sample due to cloth contamination.

The samples were then removed from the fixture and sonicated first in acetone followed by isopropyl alcohol for five minutes each to remove any loose particles that might be left from the polishing procedure. Samples were characterized using a Hitachi SU-70 field emission SEM, with spatial resolution of 1 nm and attached Bruker EDS Si drift detector (SDD), energy resolution 120 eV. Lamellas for transmission electron microscopy (TEM) were prepared from the bulk samples by mechanical polishing followed by Ar^+ ion milling and from the thin film samples by a Helios 550 FIB/SEM or Tescan GAIA3 FIB/SEM. The samples were plasma cleaned prior to TEM observation to remove organic surface contamination using a South Bay PC-2000 Plasma cleaner with a mixture of Ar/O_2 plasma.

2.2 Characterization Techniques

2.2.1 Transmission Electron Micropscopy

Transmission electron microscopy (TEM) is an imaging technique that uses the wave-particle duality of electrons. This is analogous to the use of light for optical microscopy. Electrons are extracted from a repository by applying a voltage across a source and are accelerated though a series of electromagnetic lenses at relativistic speeds. As the electrons pass through the lenses they feel forces due to the magnetic fields. The magnetic field inside each lens causes the electrons to spiral and the radius to change, which allow the beam to be dispersed, converged and focused by changing the field via the current in the copper coil of the different lenses in the microscope column. The focal length of the electromagnetic lenses can also be changed by changing the current and in turn, the magnification of the image is also changed. Once the electrons exit the field they do not spiral anymore, but their trajectory may be in a different direction from before entering the lens due to the spiraling. All electrons that are emitted from the lens at the same time arrive at the image plane at the same time. Electrons emitted at different angles do not travel the same distance and this gives rise to a broadening of the image (decrease in resolution) called spherical aberration. In some microscopes, additional lenses are added below the main lenses to correct for aberrations (primarily objective lens) due to the inherent aberration of previous lenses.

Electrons travel from the source through the lenses and to the sample at the

same energy. Once they interact with the sample they feel the potential of the electrons in the sample, which depends on the type of atoms present in the sample. The beam passes though the sample, which is prepared to be electron transparent using various techniques, where they interact with the atoms in the structure leading to elastic and inelastic scattering. There are imaging and diffraction modes which are projected on a phosphorus screen where an image (or diffraction pattern) of the region interacting with the beam can be observed. Elastically scattered electrons are collected and contribute to the diffraction pattern and the image. The specimen chamber has a base pressure of $\approx 10^{-6}$ Torr. The TEM can be operated in transmission mode, or scanning transmission mode (STEM) and various detectors are located around the column to collect x-rays, and transmitted electrons, as shown in Figure 2.1. TEM observation of the copper covetic samples was carried out in a JEOL 2100F Field Emission TEM operated at 200 kV with a spherical aberration coefficient of C_s= 0.5 mm, point-point resolution of 0.19 nm and lattice resolution of 0.10 nm. The specimen chamber has a base pressure of $\approx 10^{-6} Torr$.

As electrons from the beam interact with electrons in the sample, these incident electrons transfer energy to the electrons in the core and can cause an electron to be ejected (secondary electron). Valence electrons from higher energy states (shells) undergo transitions to fill the vacancy in the lower band left by the ejected electron.. These transitions give rise to reduction in energy, which is released as photons (x-rays) that are collected by a detector. X-rays are used in generating EDS spectra and mapping images which give information about the composition of the sample and the distribution of elements in the sample. These x-rays have a characteristic

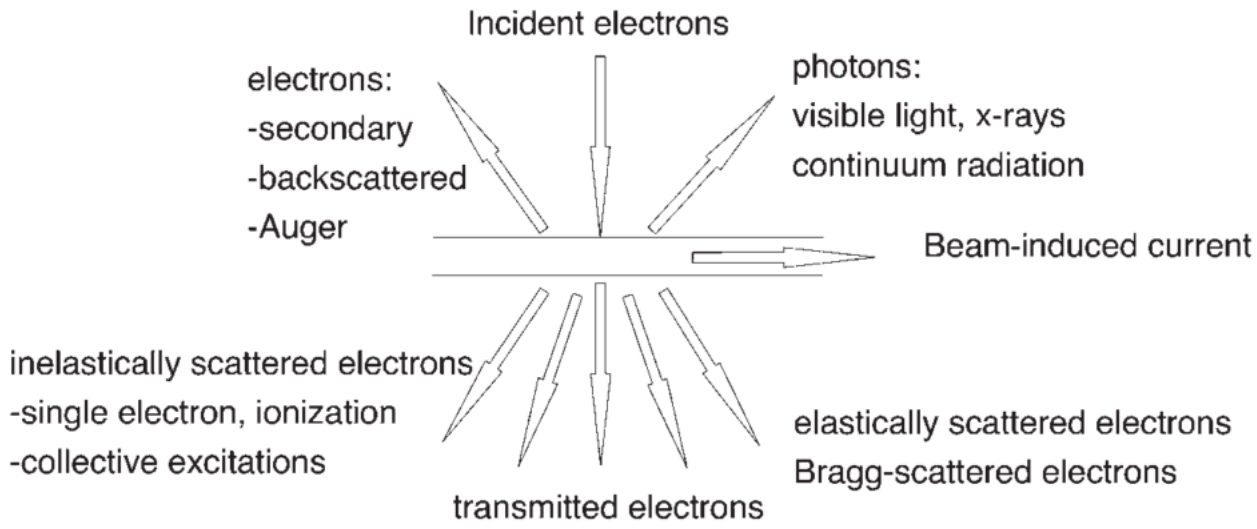

Figure 2.1: Schematic showing electron beam interaction with a sample in the TEM

energy for each atom where a high intensity peak indicates higher concentration of that element. EDS in the TEM was performed with an Oxford Inca EDS detector, energy resolution 124 eV. The concentration of an element is determined from the integrated intensity of its peak, eg. for an alloy containing two elements A and B, the weight fractions $c_A + c_B = 1$. The integrated intensity of A, I_A is given by:

$$I_A = k c_A \omega_A \sigma_A a_A t / A_A \tag{2.1}$$

where k is a proportionality constant, ω_A is the fluorescence yield of x-rays from element A, σ_A is the ionization cross-section, t is the thickness of the sample and A_A is the atomic weight of element A. Equation 2.1 is the thin film approximation and assumes no absorption.

$$\sigma_A = \frac{6.51 \times 10^{-20}}{E_c V} n_s b_s \ln[c_s U] \tag{2.2}$$

where n_s is the number of electrons in shell s, b_s and c_s are constant for a particular shell, E_c is the ionization energy, and U the overvoltage, defined as $U = E_o/E_c$ where E_o is the incident electron energy. a_A is the fraction of total K or (L, M, N) line intensities used in the calculation is given by:

$$a_{K_\alpha} = \frac{I_{K_\alpha}}{I_{K_\alpha} + I_{K_\beta}} \tag{2.3}$$

2.2.1.1 Electron Energy Loss Spectroscopy

Electron Energy Loss Spectroscopy (EELS) is a critical tool for chemical analysis as well as for probing the electronic structure of materials. As the incident electrons pass though the sample most electrons pass through without losing any energy and form the zero-loss peak (ZLP), but electrons that pass close enough to the nucleus of atoms in the sample lose some of their energy through inelastic scattering. The loss of energy can be due either to plasmon resonance excitations due to core electron excitation. The plasmon resonance can be used to probe the local electronic density of states of the material. In the case where core electrons receive the energy, they are excited to unoccupied energy levels above the Fermi level. Electrons giving rise to transitions from a 1s level form the K edge while those from the 2p level form the $L_{2,3}$ edge. The magnitude of the decrease in energy of the incident electron is related to the ionization energy of the atom from which the excited electron originated, and so the atom can be identified by the amount of energy lost by the incident electron. These electrons are collected by a detector that

uses an aperture from a narrow window - up to 2 mm in diameter to filter electrons that are scattered at an angle greater than or equal to the entrance angle to the spectrometer. The EELS spectrum is a plot of the energy loss vs. intensity and shows electrons that lose no energy (ZLP), energy equal to the plasma peaks and elemental edges (core loss). The onset of the edges reflect the difference in energy between the core level and the first unoccupied bound states. The integrated intensity under the peak is equal to the concentration of that element in the sample and is given by:

$$I_k = P_k I_T \tag{2.4}$$

where $P_k = N\sigma_k \exp(-1/\lambda_k)$. P_k is the probability of ionization of the K-edge, N is the number of atoms emitting K-edge in the sample under the electron beam, σ_k is the cross-sectional area for the K-edge excitation, and λ_k is the mean free path of the electrons exciting the K-edge. Since λ_k is very large for thin samples $P_k \approx N\sigma_k$, the integrated intensity can be written as:

$$I_k = N\sigma_k I_T \tag{2.5}$$

where I_T is the transmitted intensity. We assume $I_T \approx I_o$, the incident intensity if the sample is thin, so $I_T = F_o n\tau$, where F_o is the incident flux, n is the number of channels and τ is the dwell time. For an alloy with elements A and B

$$\frac{N_A}{N_B} = \frac{I_K^A}{I_K^B}\frac{\sigma_k^B}{\sigma_k^A} \tag{2.6}$$

where N_A is the number of atoms A contributing the K_α^A-edge, while I_K^A and σ_k^A are functions of r_o, the electron beam size, β the divergence angle and δ, the energy

window. For element A:

$$N_A = \frac{I_A}{\sigma^A_{k_\alpha} I_T} \tag{2.7}$$

After data acquisition, we subtract the background (B) by modeling it with a power law $B = AE^{-r}$.

One unique advantage of EELS over EDS is that different compounds can be determined, because changes in the valence state of an ion's polarization will change the position and shape of the edge. This modulation in the edge, called energy loss near-edge structure (ELNES) is visible in the first 10-30 eV from the edge threshold. When operated in STEM mode, small regions in a sample can be mapped quite accurately. A full energy spectrum can be taken at every pixel and is useful for identifying the intensities of weak signals using short acquisition times. A Gatan Tridiem spectrometer with energy resolution of 1 eV, was used in this study for EELS acquisition.

2.2.2 X-ray Diffraction

In X-ray diffraction (XRD) a beam of X-rays is incident upon the sample surface at an angle of incidence which is varied within a range. The interaction between the incident X-ray beam and the electrons in the sample gives rise to scattered waves which interact and give constructive interference along preferred directions that satisfy Bragg's Law. The maxima of these interference is analyzed to obtain the interplanar distances (and thus, the structure) of the sample.

This process can be modeled as a plane wave (of X-rays) incident on a collec-

tion of scatterers (atoms). By convention the angle between the incident wave and scattered wave is 2θ. The scattering is elastic, and momentum is transferred from the incident wave to the scattered wave. In the simple case the periodic structure of a crystal can be modeled as having discrete planes. X-rays will constructively interfere whenever the path difference of waves scattered by planes = $2n\lambda$, where n is an integer. Constructive interference gives rise to sharp peaks, which is an indication of an ordered periodic structure, broad peaks are an indication of disorder. The x-ray detector measures the intensity of the x-rays and plots of intensity vs. angle are generated.

XRD spectra of bulk samples were measured on a D8 Advance ($2\theta_{min} = [5^0]$) with either $MoK\alpha$ or $CuK\alpha$ radiation. Thin film samples were measured on a Bruker C2 Discover powder diffractometer using $CuK\alpha$ radiation from a sealed tube, graphite Gobbel mirror with 0.5 mm pinhole collimator, and Vantec500 area detector. Six 2D frames were integrated over 10 min yielding the diffraction spectra from $2\theta = 10^0$ to 90^0 with steps of 0.02^0.

2.2.3 Atomic Force Microscopy

Atomic Force Microscopy (AFM) was developed to image the topography of surfaces with a height resolution on the order of 0.1 nm. A sharp tip on a flexible cantilever is placed above the sample in question and the deflection of the tip due to the interaction between the tip and the atoms on the surface of the sample is monitored. If a constant force is applied between the cantilever and the surface,

the tip will trace the topography of the surface. In order to measure the deflection accurately the cantilever must respond to the force and force gradient between the tip and sample. This is determined by the spring constant and resonant vibrational frequencies of the cantilever. The deflection, Δz, of the end of a cantilever due to an applied force (F) is

$$\Delta z = -\frac{l^3}{3EI}F \tag{2.8}$$

where E is the elastic modulus of the material,β is , and I is the bending modulus, which for a rectangular bar is given by $I = wt^3/12$, where w and t are the width and thickness respectively. The spring constant is:

$$K = \frac{3EI}{l^3} = \frac{Ewt^3}{4l^3} \tag{2.9}$$

Typical values for the spring constant range between 0.06 N/m - 50 N/m. The resonant frequency of the cantilever is given by:

$$\omega_o = \sqrt{\frac{K}{m_{eff}}} \tag{2.10}$$

where the effective mass (m_{eff}) for the cantilever: $m_{eff} = m_c + 0.24m_d$ is comprised of the concentrated mass (m_c) and the distributed mass (m_d) of the beam. Typical values for cantilever resonant frequencies are from 10-400 kHz. The force of a deformed spring is:

$$F = -K(z - u) \tag{2.11}$$

where u is the equilibrium position of the end of the cantilever in the absence of external forces and z is the current position. Since $F = -\nabla W$, we can write:

$$W = \frac{1}{2}K(z - u)^2 \tag{2.12}$$

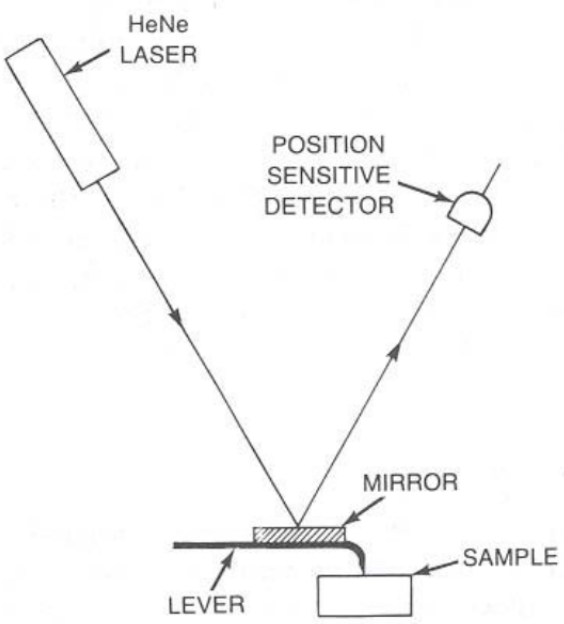

Figure 2.2: Schematic of AFM apparatus.(*51*)

and $K = \delta^2 W/\delta z^2$. The force on the cantilever will also include a contribution due to the interaction of the tip with the sample. The displacement (z) dependence of the total force can be expanded in a Taylor series about equilibrium (u) in the presence of external forces.

$$F(z) = F(z_0) + \frac{\delta F(z_0)}{\delta z}(z - z_0) + ... \tag{2.13}$$

so the total force on the cantilever is $F(z) = -K(z-u) + F_{ST}(z)$, where F_{ST} is the force due to the interaction between the sample and the tip. Expanding the total forces gives:

$$F(z) \approx -\left(K - \frac{\delta F_{ST}(z_0)}{\delta z}\right)(z - z_0) \tag{2.14}$$

and the effective spring constant (K^1) is:

$$K^1 = K - \frac{\delta F_{ST}(z_0)}{\delta z} \tag{2.15}$$

Therefore an attractive interaction between the tip and sample opposes the restoring force, and corresponds to a positive gradient, decreasing K^1. A repulsive interaction corresponds to a negative gradient and thus a larger K^1. This results in a shift of the resonant frequency (Equation 2.10) to:

$$\omega_o^1 = \sqrt{\frac{K^1}{m_{eff}}} \tag{2.16}$$

where an attractive interaction leads to a lower resonant frequency. Equation (2.16) indicates that an instability will occur when $K^1 \to 0$. This occurs when the magnitude of the attractive force gradient is equal to the spring constant of the cantilever. This results in the tip position jumping spontaneously to a different value to a position where K^1 is non-zero, but where the overall force is zero. The force-displacement curve for the tip-surface interaction shows this instability. To avoid this instability a tip with large K can be used, but this decreases the sensitivity of the measurement to small changes in force. The force-displacement curve contains three regimes: close to the surface, bonding forces within the sample are dominant, while far away electrostatic/magnetic forces are prominent and between these extremes, Van der Waals forces are predominant.

The deflection of the position of the cantilever is measured with high precision using a laser beam incident on the back of the cantilever which is reflected into a detector split into two halves (see Figure 2.2). The change in the relative intensity of the two halves can be used to measure the deflection accurately. Before approaching the surface with the tip the cantilever response must be tuned by varying the frequency of the cantilever until the amplitude response is a maximum.

As the tip approaches the sample the interaction between the tip and the sample becomes significant. Depending on whether the force is attractive or repulsive there is a resulting change in the spring constant, which in turn results in a change in the frequency of vibration of the tip through a feedback loop. The feedback loop maintains a constant cantilever deflection, which is essential for maintaining the force that allows for the surface to be mapped.

The AFM can be operated in contact or tapping mode. In tapping mode the cantilever tip is positioned 1 - 10 nm above the surface, this is typically within the attractive portion of the force-displacement curve, which is usually dominated by Van der Waals or other long-range forces. The displacement is modulated slightly above its resonant frequency where the amplitude is sufficiently large to move the tip close to the surface. This causes the resonant frequency to shift downwards. When the tip approaches the surface it moves into the repulsive region of the force-displacement curve, which pushes the tip up, leading to a tapping action. As the sample position is rastered, the amplitude is monitored and the signal sent to the feedback loop so that the tip is moved up or down as necessary to maintain a constant amplitude. This prevents the need to drag the tip across the surface as is done in contact mode.

In this dissertation a Dimensions 3000 or Asylum Research Cypher AFM was used to characterize the surface roughness of the films in tapping mode using Si N-type tips purchased from App Nano with resistance 0.01 - 0.025 Ohm-cm, cantilever dimensions 125 μm x 30 μm x 4 μm with a tip radius $<$10 nm and height 14 - 16 μm. The resonant frequency is 200 - 400 kHz and spring constant (K) of 13

- 77 N/m. A complementary technique, Kelvin probe force microscopy (KPFM), was used to map the surface potential of films at fly-height ≈10 nm above the sample sufrace. KPFM probes (PtSi-FM, Nanosensors) had a spring constant and resonance frequency of approximately 5 Nm^{-1} and 75 kHz, respectively. The tips had a nominal radius of curvature of 25 nm and included a conductive Platinum Silicide coating. Measurements were made in AC mode with a scan rate of ≈ 1 Hz.

2.2.4 X-ray Photoelectron Spectroscopy

X-ray Photoelectron Spectroscopy (XPS) is a tool used to investigate the chemical composition of surfaces. Surface analysis involves irradiating a sample in high vacuum with a fixed wavelength x-ray beam and analyzing the energy of emitted electrons from the core shells of the atoms in the sample. The spectrum produced is a plot of the number of electrons detected per energy vs. their kinetic energy. Although X-ray photons penetrate deep into the sample, on the order of 1-10 μm, only the interaction with the atoms on the surface (<10 nm) cause electrons to be emitted from the sample via the photoelectric effect (Figure 2.3). Thus the electrons detected originate from the top few atomic layers of the sample because the mean free path of electrons in solids is small (tens of angstroms), making XPS a surface-sensitive technique for chemical analysis.

The emitted electrons have kinetic energy:

$$KE = h\nu - BE - \phi_s \tag{2.17}$$

where $h\nu$ is the energy of the photon, BE is the binding energy of the core elec-

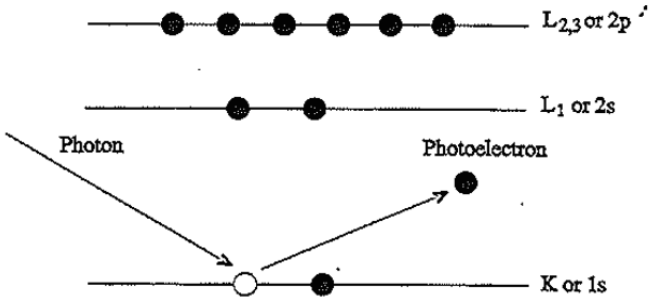

Figure 2.3: The XPS photoemission process whereby an incoming photon causes the ejection of a photoelectron.(*52*)

tron and ϕ_s is the spectrometer work function. The electrons that leave the surface without energy loss (elastic scattering) produce peaks in the spectra, while those that lose energy (inelastic) form the background. XPS can be used to identify and determine the concentration of the elements in the sample, because each element has a unique set of electron binding energies, defined as the difference in energy between the atom before and after photoemission, and corresponding kinetic energies. The binding energy can be red or blue shifted depending on the atom to which the atom of interest is bonded. Additionally, chemical potential and polarization of the compound can cause variations in binding energy (chemical shifts). This chemical shift can be used to identify the chemical state of the material. The electrons leaving the sample are detected by an electron spectrometer according to their kinetic energy. The energy window (pass energy) of the spectrometer is kept fixed to maintain a constant energy resolution and electrons are detected as discrete events. The number of electrons for a given time and energy are displayed in a plot. Ion sputter etching is also used in conjunction with XPS for removing surface contamination

from hydrocarbons and also in producing a depth profile of the sample composition. Ar-ions (Ar^+) are typically used to etch the surface of a standard with known thickness in order to calibrate the sputter rate and convert sputter time of the sample into depth.

XPS was obtained with monocromatic Mg (1287 eV) or Al K_α (1486.6 eV) x-rays using a Kratos Axis 165 or Physical Electronics Model 5400 spectrometer. Survey spectra were collected at constant pass energy of 89.5 eV. Multiplex spectra were collected at constant pass energy of 35.8 - 40 eV and an electron takeoff angle of 45 degrees. The area analyzed by XPS was a spot with a diameter of 1.1 mm. Depth profiling was done with 4 keV Ar-ions using a rastered area of 5 mm x 5 mm. The detection limit is ≈ 0.1 at.%.

2.2.5 Time of Flight Mass Spectrometry

Time of Flight Secondary Ion Mass Spectrometry (TOF-SIMS) is a technique that measures the mass/charge ratio of ions. The ionic concentration of species sputtered from of Cu and Cu covetic samples sputtered using Ga^+ ions were obtained using a TESCAN GAIA3 FIB and measured using a TOFWERK detector where the species are analyzed and displayed as intensity vs. mass charge ratio (m/Q). The intensity is measured in units of counts per extraction (cts/ex). Since the carbon atom has atomic mass of 12 u, the mass/charge ratio of a singly charged ion of carbon is 12 Thomson (Th). If the carbon atom is doubly charged the mass charge ratio is 6 Th. One extraction corresponds to one pulse or one pixel scan in the FIB

and as such, the counts per extraction is independent of the volume from with the data is integrated. This indicates that we can expect the same intensity independent of the depth of the measurement and the number of pixels used in the scan, making comparisons between scans more reliable.

2.2.6 Raman Spectroscopy

In Raman spectroscopy, light induces vibrations of the atoms (phonons). In the case of graphite this gives rise to the so-called D and G peaks as shown in Figure 2.4. The G peak ($\approx 1580\ cm^{-1}$) is emblematic of pristine graphite while the D peak ($\approx 1354\ cm^{-1}$) is due to imperfections in the graphite planes and at edges when there are unsatisfied bonds, where defects such as 5-7 rings, vacancies and sp^3 bonded C are present or when carbon atoms are bonded to other atoms. Deviations from these wavenumber values usually indicate strain in the material.

Raman spectra were obtained using a HORIBA integrated confocal micro-Raman system (LabRAM ARAMIS) equipped with a HeNe (632.8 nm) laser as excitation wavelength source. Measurements of the covetic samples were performed using radiation at 632.8 nm with a real output power of 9 mW. A filter was used to modulate the laser power on the samples by a factor of 0.1. The samples were observed with the attached Olympus BX41 microscope 100x objective, which gives a laser spot of 1 μm. The analyzed areas were pinpointed by using a TV camera attached to the microscope.

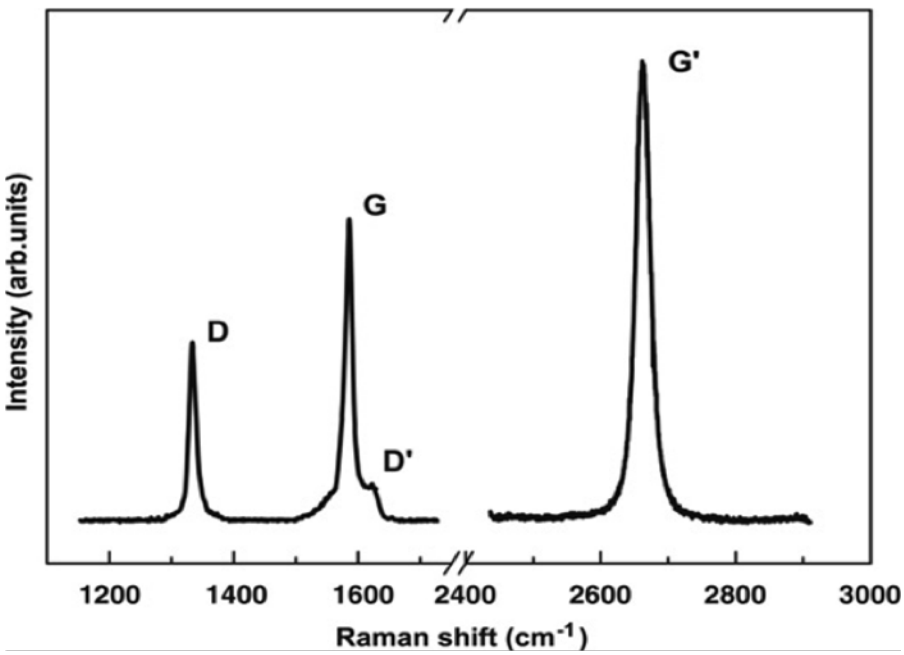

Figure 2.4: Raman spectroscopy of graphene showing the G peak emblematic of pristine graphite and D peaks which is observed at the edges of the graphene sheet.(*53*)

2.2.7 Ellipsometry

A J.A. Woollam M2000 spectroscopic ellipsometer with a wavelength range from 193 nm -1000 nm with variable angle, microfocus, and mapping stage was used to measure the index of refraction of films in this thesis.(*54*) An ellipsometer measures the change in the amplitude (Ψ) and phase (Δ) of light reflected from a material as a function of wavelength of light. The incident light is linearly polarized and the change in the polarization of the reflected light is measured vs. the wavelength of the incident light for several angles of incidence (e.g. 60, 65 and 70 degrees). The ratio of the reflected light on plane p (r_p) to the reflected light on

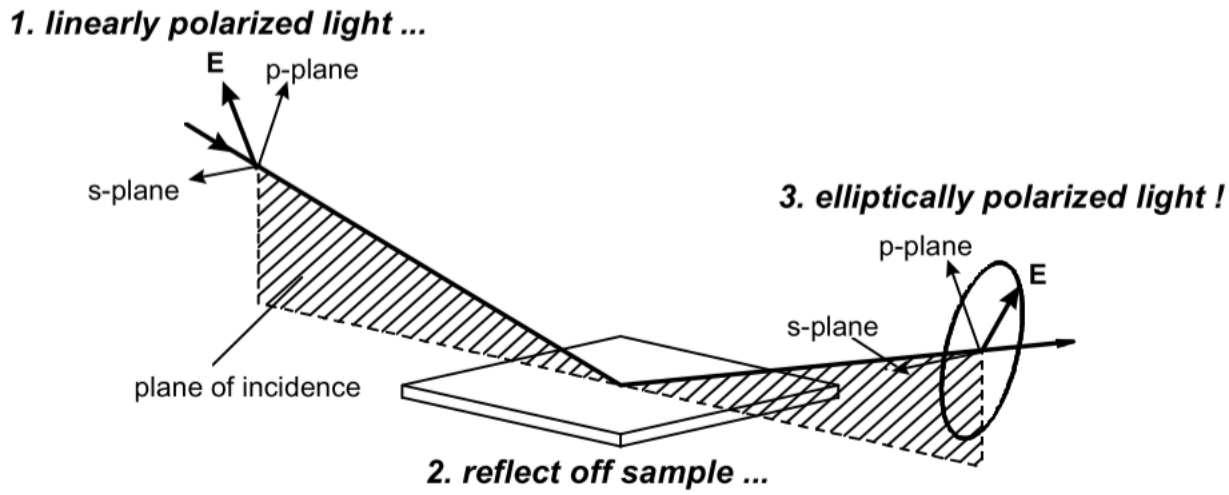

Figure 2.5: Schematic showing the J.A.Woollam Co. Inc. spectrometer.(*55*)

plane s (r_s)(see Figure 2.5) is given by Eq 2.18:

$$p = \frac{r_p}{r_s} = \tan\Psi \exp[i\Delta] \tag{2.18}$$

Ellipsometry data is analyzed assuming a model for the material that consists of a Si substrate, SiO_2 intermixing layer and Cu film. The model takes into account internal reflections at every interface and fits the data for all angles and complete range of wavelengths. The best match is achieved through regression to obtain the mean squared error (MSE), as defined in Eq. 2.19

$$MSE = \sqrt{\frac{1}{3n-m}\sum_{i=1}^{n}[(N_{E_i}-N_{G_i})^2+(C_{E_i}-C_{G_i})^2+(S_{E_i}-S_{G_i})^2]} \times 1000 \tag{2.19}$$

where n is the number of wavelengths, m is the number of fit parameters and $N = cos(2\Psi)$, $C = sin(2\Psi)$ and $S = sin(2\Psi)sin(\Delta)$. The measured data are parameters subscripted with E and model generated data have parameters subscripted with G. Since Cu is a partially absorbing film, we use the B-spline layer provided by the J.A. Woollam software CompleEASE to represent the Cu/Cu covetic film.(*55*) This

layer allows for arbitrary flexibility in the n and k vs wavelength, since the optical constants are not known before the measurement. The B-Spline layer specifies the optical constants versus wavelength using a series of control points which are equally spaced in photon energy (eV). The spacing between the control points is controlled by the resolution. Smaller resolution adds more control points, resulting in more flexibility to accommodate sharp features in the dielectric constant spectra, but if the resolution is too low noise or unphysical artifacts in the dielectic function spectra can arise. Basis spline curves are used to interpolate the optical constant between the control points. The B-spline layer is described by the complex dielectric function: $\epsilon = \epsilon_1 + i\epsilon_2 = (n + ik)^2$, ($n$ and k are the real and imaginary parts of the index of refraction) written as $e1$ and $e2$. The dispersion in $e1$ is specified by one set of control points and $e2$ by another. In this study, we initialize the B-spline layer with control points matching the optical constants of Cu, a resolution of 0.3 eV and use "KK mode" which maintains Kramers-Kronig consistency between the resulting $e1$ and $e2$ spline curves by constraining the optical constants to a physical shape, providing further confidence that the resulting optical constants are reliable.

Chapter 3: Incorporation of C into the Cu lattice

3.1 Characterization

Quantifying the amount of carbon incorporated into the bulk structure has been a critical part of understanding covetic materials. The main challenge when analyzing covetic materials is the presence of surface C contamination in the form of hydrocarbons, which can obscure the carbon network and bonding structure present in the material. The primary spectroscopy techniques utilized to quantify the bulk carbon content are EDS in both TEM and SEM and XPS. These procedures require that great care be exercised to prepare and clean the surface of the material in order to remove carbon contamination. The procedure detailed in Chapter 2 is critical for overcoming these challenges. Figure 3.1(a) shows an optical image of a Cu cv 3% extruded sample that has been cut to reveal the bulk structure. Scratches can be clearly observed on the surface at 5x after cutting while Figure 3.1(b)-(f) shows the polished surface free of scratches that reveal the microstructure of the bulk.

We measured the C concentration using SEM-EDS to get a sense of the global average C content in these bulk samples. EDS is a global technique where we probe tens of microns across the sample surface. This Cu covetic sample exhibits C concentration of 3.67 wt.% ($\approx 15.32 \pm 0.7$ at.%) using 10 kV accelerating voltage as

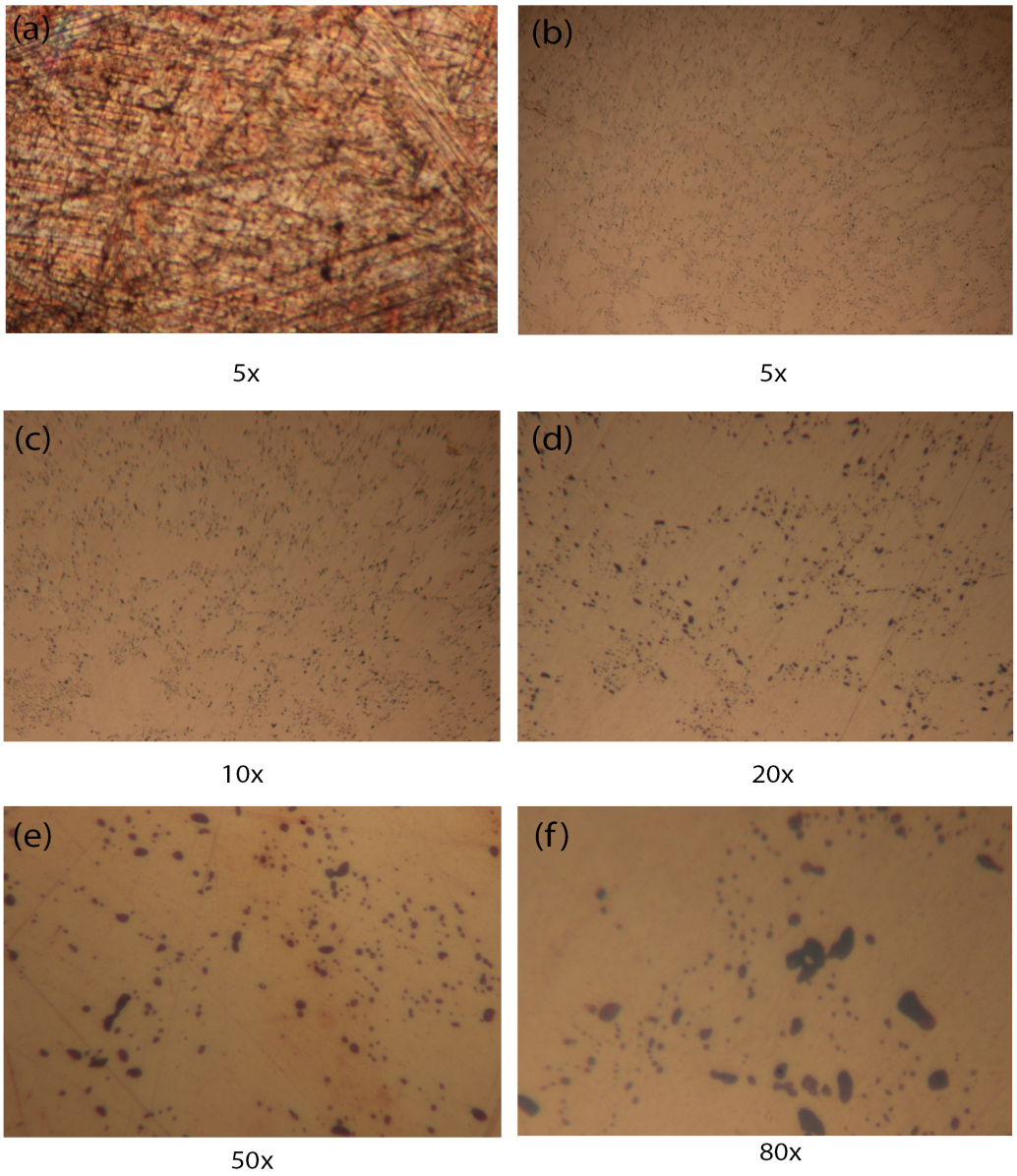

Figure 3.1: Optical images of (a) an extruded Cu cv 3% sample cut to reveal the bulk structure, polished surface (b) 5x, (c) 10x, (d) 20x, (e) 50x and (f) 80x

shown in Figure 3.2 (a). An SEM image of this sample is shown in Figure 3.2(b), with mapping showing the presence of Cu, O, and C in Figure 3.2(c), (d) and (e), respectively with false color images overlaying the secondary electron image. The Cu and O distribution is quite uniform, but in the C image, there are regions with very strong contrast $\approx 1\ \mu m$ in diameter interspersed between a weaker contrast background. This distribution suggested that the carbon content is not uniform throughout the bulk, and variations in the local carbon concentration are present at smaller length scales. Furthermore, SEM-EDS presents challenges with regard to quantifying C content due to the presence of C contamination. Even though samples are cleaned with acetone and IPA prior to examination of the sample surface, the vacuum in the column of the SEM ($\approx 10^{-5}$ Torr) does not maintain a contamination free environment.

XPS is more reliable due to the high vacuum and the ability to sputter below the surface inside the vacuum chamber. Photoemission spectra is collected once the working pressure is better than 5×10^{-8} Torr, which aids in reducing hydrocarbon contamination. In the XPS the sample is mounted to a fixed stage. An x-ray gun mounted at a 45-degree angle is used to bombard the surface of the sample and photoelectrons are produced via the photoelectric effect. In order to measure the bulk C concentration an Ar^+ gun mounted at 45 degrees, but in a different relative position to the sample than the x-ray beam, is used to sputter the sample to expose a fresh surface of the sample in order to obtain a depth profile of the concentration. If the surface of the sample is rough, only the side facing the sputter gun is bombarded with Ar^+ ions and so hydrocarbons remain on the opposite face giving

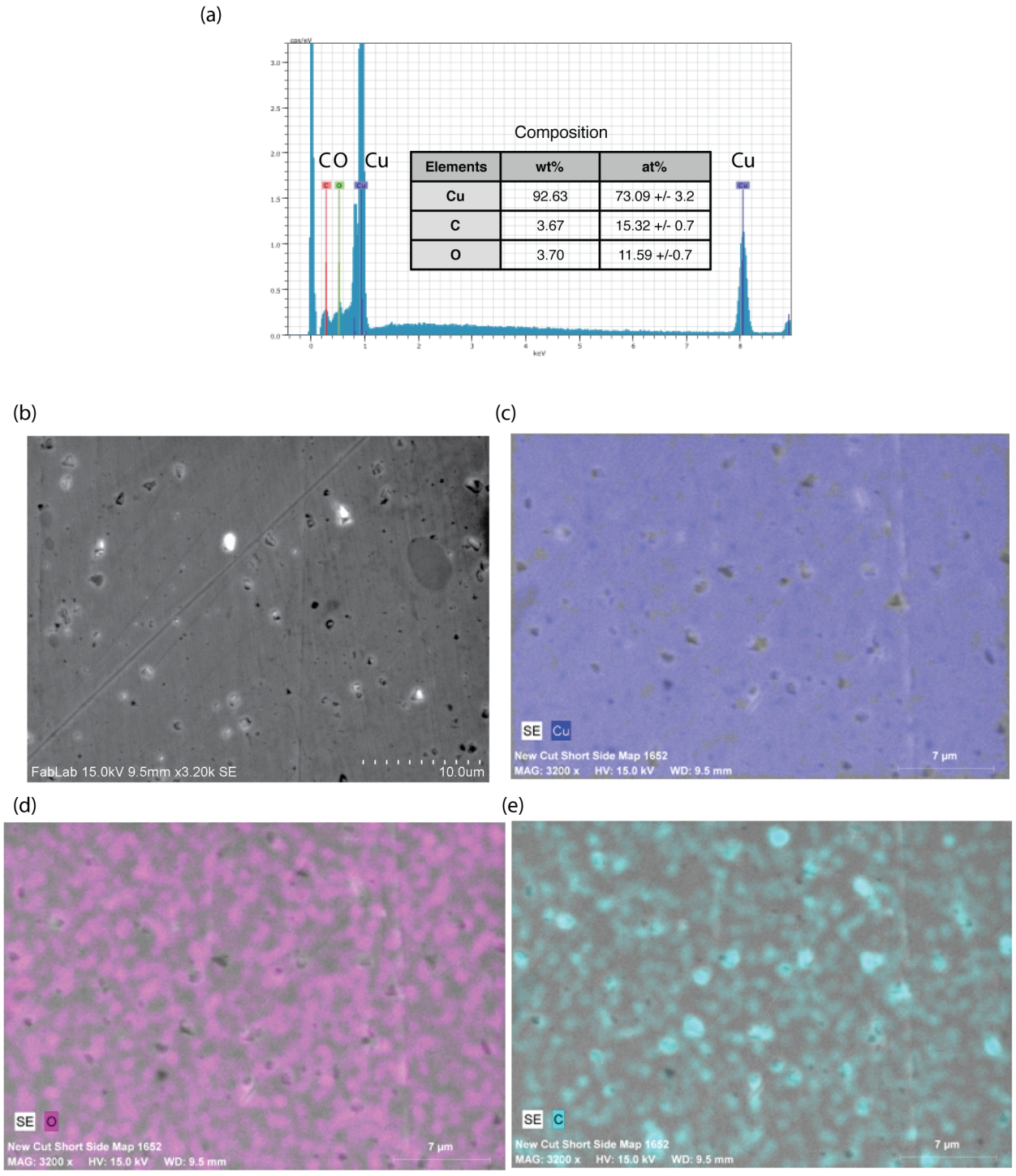

Figure 3.2: (a) SEM-EDS spectrum of a Cu covetic bulk sample with nominally 5 wt.% C showing 3.67 wt.% ($\approx 15.32 \pm 0.7$ at.%) C (b) SEM secondary electron image of the region acquired, with mapping showing the presence of (b) Cu, (c) O, and (d) C with false color images overlaying the secondary electron image

rise to a shadowing effect. Since x-rays penetrate several microns into the material, photoelectrons from the unsputtered regions still contribute to the signal. Sputtering for 24 hours only removes about 1 μm of material, so if the roughness exceeds 1 μm this effect persists during the whole sputtering cycle. Since hydrocarbons often dominate the bulk C signal, we can get an effect where we measure more C than Cu in the bulk if the surface is not flat, therefore polishing and reducing surface roughness is of paramount importance in XPS.

We received several Cu covetic samples from Third Millennium Materials with different nominal C concentrations: 3 wt.%, 4 wt.%, 5 wt.%, 9 wt.%, 10 wt.%, and 15 wt.%. XPS was used to measure the C concentration and bonding type (sp^2 and/or sp^3) in each sample. Typical concentration results are shown in Table 3.1. In general, we measured significantly less carbon than the reported nominal concentration in each case. In this thesis, we generally refer to the nominal C content in wt.% that was added during fabrication process and not the measured C content for consistency. XPS combined with sputtering using Ar^+ ions makes depth profiling possible and is used to identify the bulk composition. A 5×5 mm^2 area was sputtered with 4 keV Ar^+ ions for depth profiling. The C 1s, O 1s and Cu $2p_{3/2}$ multiplex regions were collected after each sputtering cycle. Cu sputters at a rate of $\approx$ 10.2 nm/minute. Due to the beam diameter of 1 mm, we are inherently probing larger areas than EDS.

Figure 3.3(a) shows an XPS survey spectra from the same Cu covetic sample (with nominally 5 wt.% C) that SEM-EDS was performed on (Figure 3.2) as well as a Cu metal foil (99.99%) for comparison. Figure 3.3(b) shows the survey spectra before

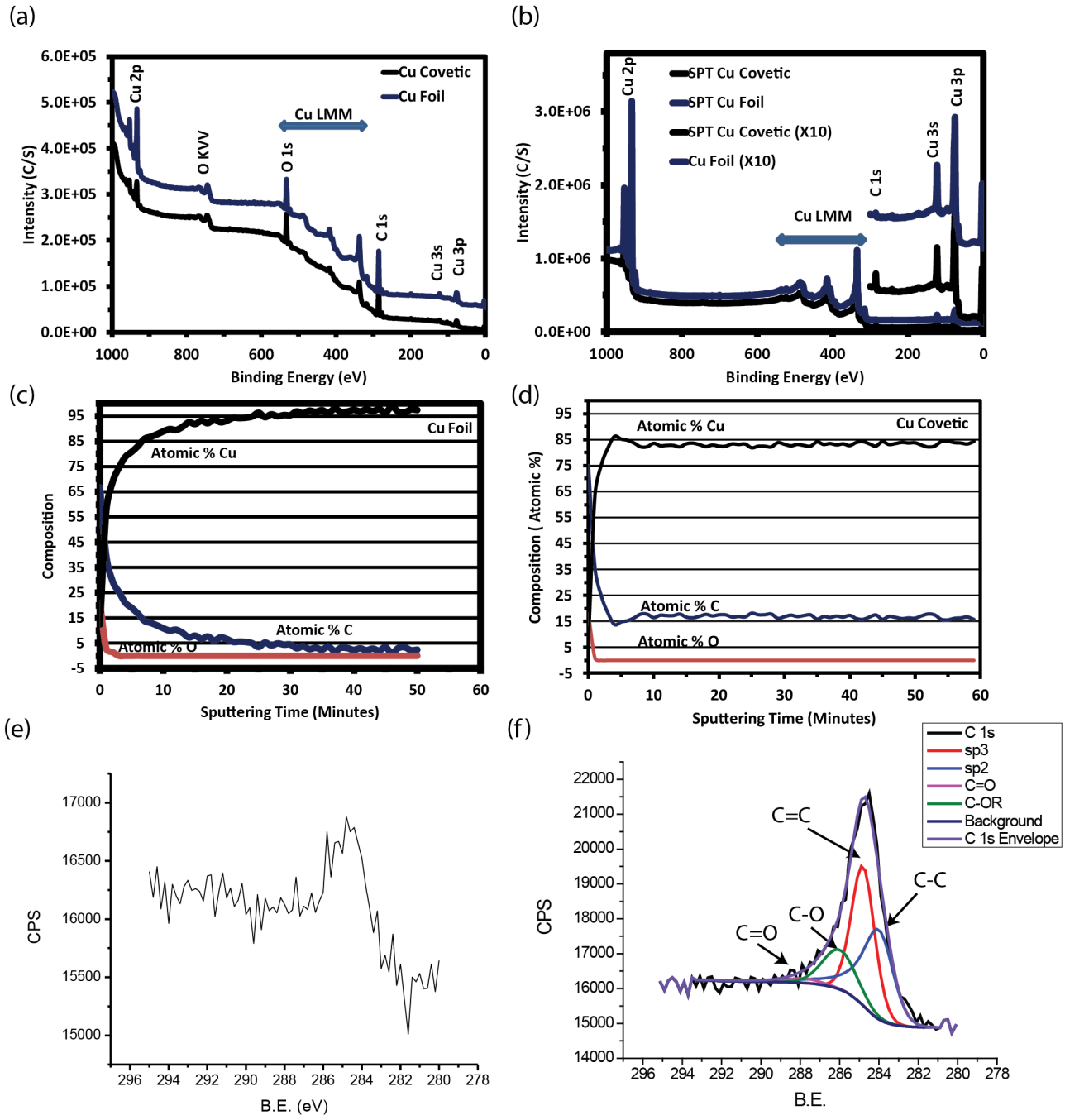

Figure 3.3: XPS survey spectra of a Cu covetic and Cu metal sample showing atomic concentration of C 1s, O 1s and Cu $2p_{3/2}$ (a) before and (b) after sputtering. Depth profile of the (c) Cu metal and (d) Cu covetic samples showing average C concentration of 2 at.% ($\approx$ 0.38 wt.%) and 16 at.% ($\approx$ 3.5 wt.%) respectively after 50 min and 60 min of sputtering respectively. Photoemission spectra of the C 1s peaks after 30 minutes of sputtering of the (e) Cu metal and (f) Cu covetic samples

Table 3.1: Typical nominal vs. XPS measured concentration for bulk Cu covetic

Nominal C Conc. (wt.%)	C 1s (at.%)/(wt.%)	Cu 2p (at.%)	O 1s (at.%)
3	2.27 (0.44)	96.69	1.03
4	2.94 (0.57)	90.77	0.64
5	6.31 (1.26)	93.68	0
9	11.85 (2.42)	82.97	5.17
10	5.39 (1.06)	94.6	0
15	3.67 (0.71)	95.7	6.37

and after sputtering and reveals the importance of sputtering below the surface due to the large amount of surface contamination from the environment on the samples. The Cu metal foil and Copper covetic samples were placed in the chamber at the same time, and therefore subject to the same vacuum and sputtering conditions. The depth profiles of both samples are shown in Figures 3.3 (c) and (d), where an average C concentration of 2 at.% ($\approx$ 0.38 wt.%) and 16 at.% ($\approx$ 3.5 wt.%) was measured for the Cu metal foil and Cu covetic samples after 50 min and 60 min of sputtering respectively. As expected in both cases, the XPS depth profile shows high carbon at the surface of the sample due to hydrocarbon contamination that tapers off to a consistent level within the bulk sample after sputtering.

Though the depth profile gives a global view, it does not say much about how carbon is bonded in the material. In order to elucidate the chemistry of carbon in

these samples, further analysis was done on the multiplex regions. A monocromatic Al x-ray source has an energy resolution of 0.2 eV, but the width of the convoluted multiplex peak depends on a number of factors including: Heisenberg uncertainty principle, lattice vibrations which are always present unless the sample is at 0 K, and the crystallinity of the sample. In single crystalline materials, all atoms are in the same environment and have the same energy, resulting in a narrow peak. Broadening occurs when atoms of the same type are in different environments, such as when they are bonded to different elements. As such, XPS is sensitive to the type of bonding in the material.

C 1s and O 1s peaks were calibrated relative to the Cu $2p_{3/2}$ peak which is fixed at 932.7 eV. The main peak of C 1s is sp^3 bonded C, which is allowed to float around position A ($\approx$ 284 eV). All other peaks are fixed relative to A as shown in Table 3.2. Deconvolution of the C 1s peak shows the contributions from the elements to which C has bonded. Figures 3.3 (e) and (f) show the C 1s peak from Cu metal and Cu covetic respectively. Due to the noisy C 1s photoemission spectra obtained from the Cu metal sample it was not possible to deconvolute the peak shown in 3.3 (e). For the C 1s peak of Cu covetic (Figure 3.3 (f)), a suitable background was demarcated, envelope and peak positions modeled to the data of one scan of the C 1s peak and refined by fitting to the entire dataset until convergence. The deconvolution indicates the presence of sp^2 (C-C), sp^3 (C=C), CO-R, C=O, where R could be either C or H. The peak position of one scan after 30 minutes of sputtering (Figure 3.3 (e)) is detailed in Table 3.2.

At the surface, only sp^3 C is found, which is primarily due to hydrocarbon

Table 3.2: Deconvouluted C 1s peaks position and area of components of one scan after 30 mins of sputtering (Figure 3.3 (e)) with positions constrained relative to sp^3 C.

peak	Constraint	Position	Area
sp^2	A-0.8	284.0	34.62
sp^3	A	284.8	45.00
CO-R	A+2	286.8	18.35
C=O	A+3	287.8	2.03

contamination. As we sputter into the bulk, sp^2 C emerges, and sp^3 C persists. The sp^2 carbon is primarily found in graphitic structures and sp^3 carbon in the structure of diamond. However, we know that the source material used to make covetics, activated carbon, contains both sp^2 and sp^3 C.

The XPS results are corroborated by Time of Flight Secondary Ion Mass Spectrometry (ToF-SIMS). ToF-SIMS of a Cu cv 5% sample was acquired in negative ion mode with a current of 1.5 nA in an area 20 μm x 20 μm and 200 frames deep. The total mass spectrum shown in Figure 3.4(a) is taken from the whole analyzed volume and reveals peaks at 12 m/Q, 13 m/Q and 14 m/Q, corresponding to C^-, CH^- and CH_2^- ions respectively. The mass spectrum of Cu metal shown in 3.4(b) indicates that there is no appreciable peak for C or its compounds in the same range. The spectrum shown in 3.4(b) is essentially noise from the mass spectrometer. Negative ion mode is used for detecting negative ions, so we do not expect to see peaks

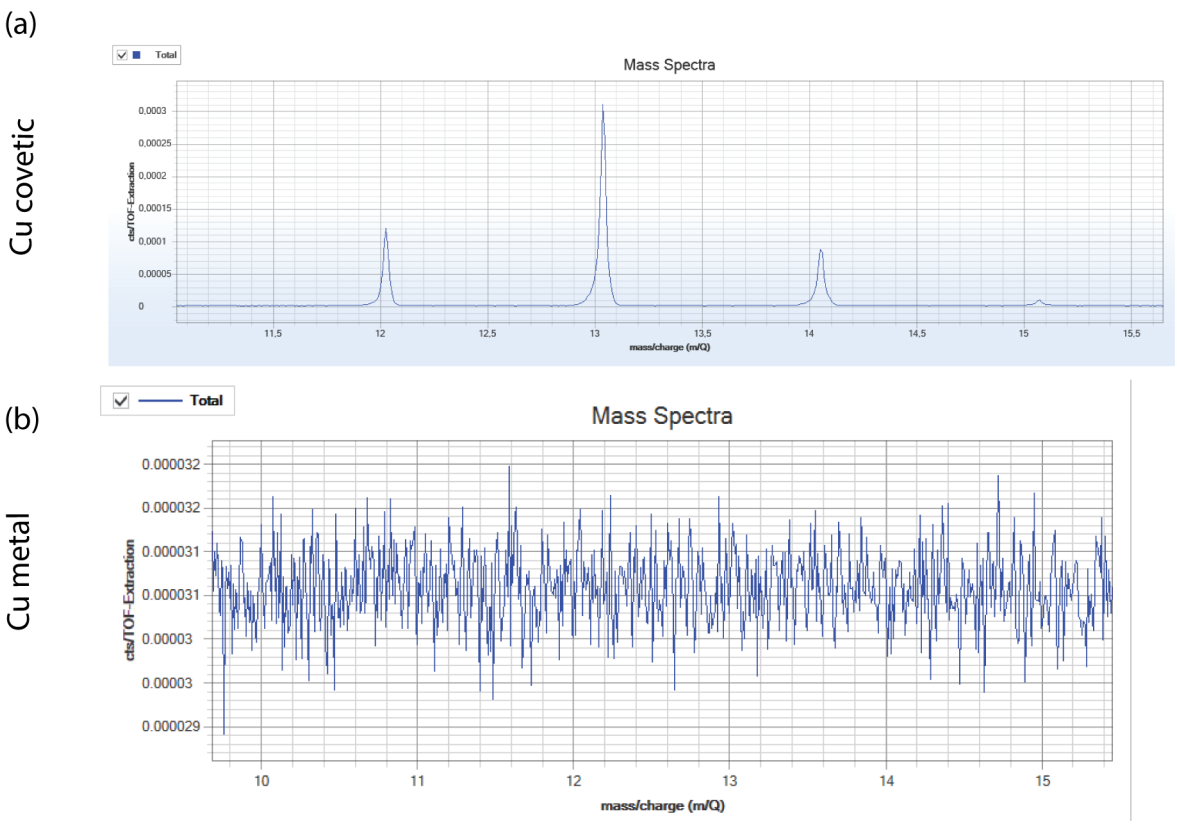

Figure 3.4: TOF-SIMS mapping and mass spectra of Cu and Cu cv 5% sample.

from Cu in this spectrum. An O^{2-} peak is expected at 16 m/Q, and depth profile (not shown) indicates the presence of a thin oxide at the surface for 3 frames, but it quickly diminishes and as such is not enough to produce a significant peak in the spectra.

Once we identified the presence of carbon in Cu covetic samples, we sought to elucidate how the carbon incorporated using XRD. XRD spectra of bulk Cu covetic with nominal carbon concentration of 5 wt.% (21.78 at.%), 10 wt.% (37.02 at.%) and 15 wt.% (48.29 at.%) shown in Figure 3.5, exhibit no impurity phases, no copper oxide phases or any of the allotropes of C, but there is a slight increase in the lattice constant (except for the sample with 10 wt.% C) compared to bulk Cu (a=0.36149

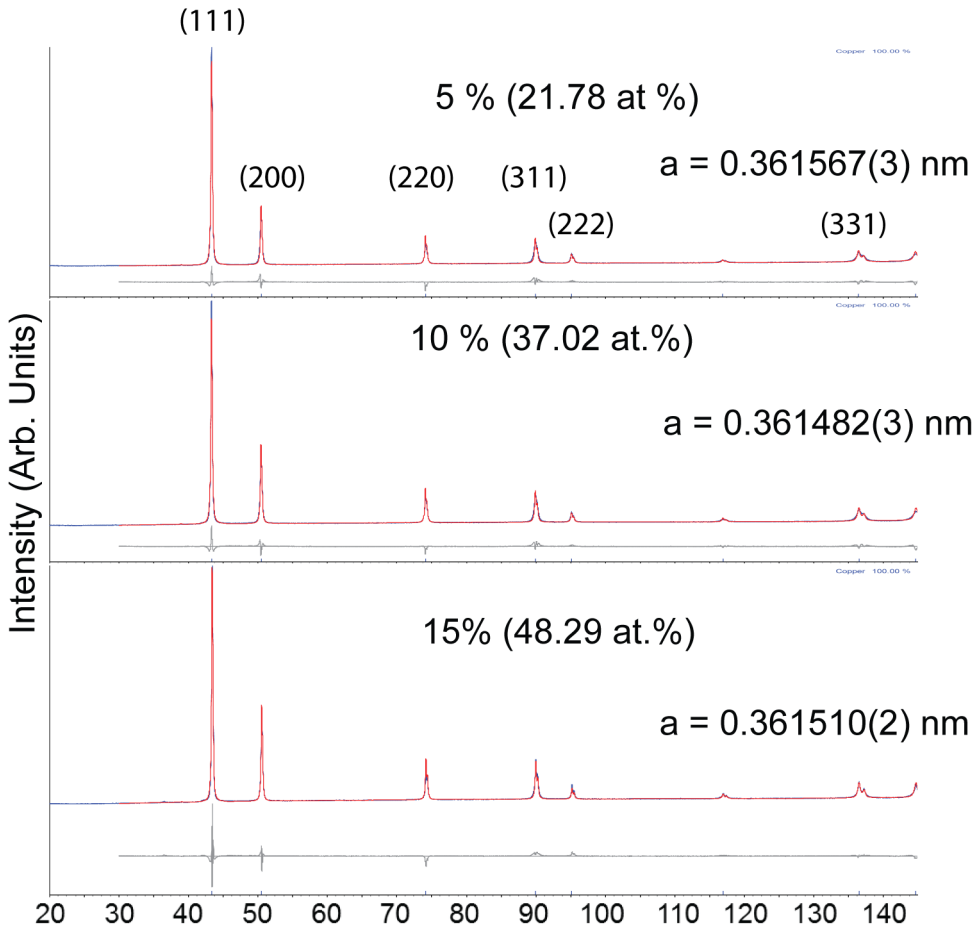

Figure 3.5: XRD spectra of Cu cv 5%, 10% and 15% showing slightly increase in the lattice constant compared to bulk Cu and texturing in <111>

nm). Cu cv 5%, 10% and 15% have lattice constants of 0.361567(3), 0.361482(3) and 0.361510(2) respectively. There is some texturing, difference between the measured and expected orientation, observed in all three samples in the <111> direction, which indicates either a preferred orientation or possibly a difference in the structure of Cu covetics compared to Cu metal.

Given the inhomogeneity present in these Cu covetic samples, we sought to identify and study the structure of covetics at smaller length scales, where we could

identify the regions with high carbon content shown from EDS to be $\approx 1\ \mu m$ in diameter and study how carbon incorporation affects the Cu lattice in these regions. We prepared TEM samples by mechanically polishing a disc of 3 mm in diameter on a polishing wheel and thinning to electron transparency using Ar^+ ion milling. Figure 3.6 (a) shows a bright field image of bulk Cu cv 5% at the end of thinning, where there is a hole in the center of the sample (right side of image), and thin areas next to the hole that are electron transparent. These samples have a thickness gradient, with thicker areas further away from the hole (left side of image). In the lattice structure, nanocarbon regions with a modulation of ≈ 1.6 nm are observed along several crystallographic directions of the sample as shown in the high resolution TEM (HRTEM) image in Figure 3.6 (b). The $(01\bar{1})$-electron diffraction pattern from this area presents weak satellite spots (marked by arrows) corresponding to the modulation observed in the HRTEM image in Figure 3.6(c). This region of the sample contains a relatively high concentration of carbon of 7.4 ± 0.8 wt.% (29.72 at.%) as measured by EDS (Figure 3.6(d)) in the TEM and suggests that the carbon is incorporated into the copper lattice. Other areas of the sample showed lower nor no concentration of C.

In-situ TEM measurements have shown that it is possible for nucleation of carbon nanostructures to occur from the end faces of metal particles inside larger host tubes when multi-walled nanotubes containing encapsulated Co, Fe, FeCo, and Ni nanowires are irradiated with a strong electron beam.(*56*) It is thus likely that during the fabrication of covetics, the high electric current applied to the molten metal leads to self-organization, or self-assembly, of carbon nanostructures within

the lattice of the metal giving rise to the observed modulation in the structure of the covetic. (*57*)

In order to understand the bonding of C in Cu covetics, we performed EELS on bulk samples, with particular emphasis on the C K-edge. Nistor et, al.(*58*) have shown that it is possible to distinguish different allotropes of C: diamond, amorphous and graphitic, based on the shape of the C K-edge as shown in Figure 3.7 (a). Diamond has only sp^3-bonded carbon, graphite has purely sp^2 bonding and amorphous carbon contains a mixture of sp^2 and sp^3 bonded carbon. All forms of carbon produce an edge at $\approx$ 285 eV in the EELS spectra. This peak (shown in Figure 3.7 (b)) is indicative of sp^2 bonding and is characteristic of the transitions of electrons from 1s occupied state to π^* unoccupied states in sp^2- bonded carbon.(*59*) The stronger the sp^2 bonding is (as it is for graphite) the higher the intensity of this peak. This edge occurs just below the main absorption threshold at $\approx$ 290 eV, which corresponds to transitions from the 1s occupied state to the σ^* state found in both sp^2 and sp^3- bonded C.

An EELS spectrum image was acquired from a region of a Cu cv 5% bulk sample shown in the high angle annular dark field (HAADF) image in Figure 3.8(a). The dark region in the bottom right hand corner of the image is a hole in the sample and the area where the spectrum image was acquired includes a region at the edge of the sample and is delineated by a rectangle. In dark field, lighter elements appear dark and heavier elements appear brighter in contrast. A high magnification of the acquired spectrum image is shown in Figure 3.8(b). The spectrum image is a three-dimensional dataset where the electron beam scans the demarcated area

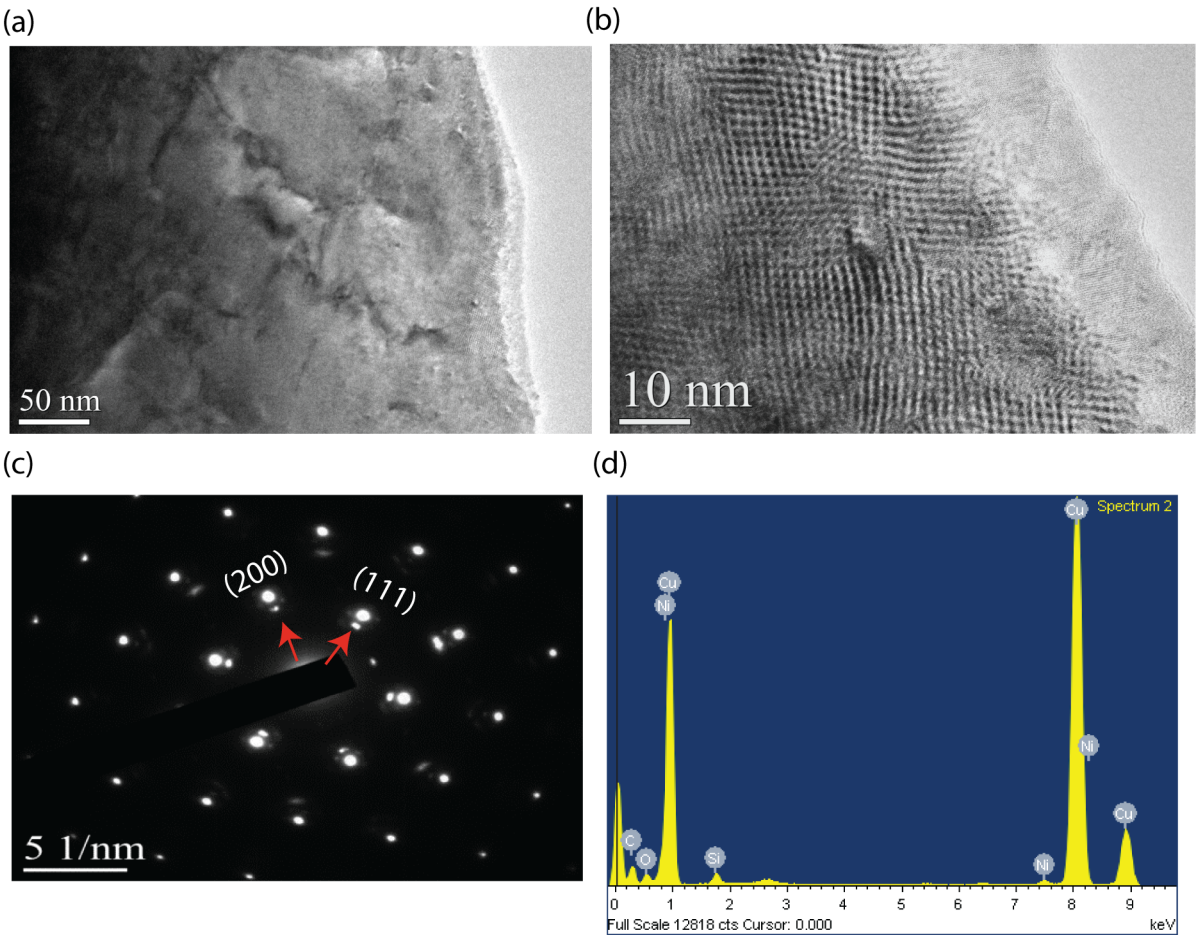

Figure 3.6: (a) Bright field TEM image of a sample with nominally 5 wt.% C in the Cu covetic bulk, (b) is the HRTEM image from the area shown in (a) showing a modulated structure. (c) Electron diffraction pattern from the modulated region, (d) EDS spectrum from the area in (a)

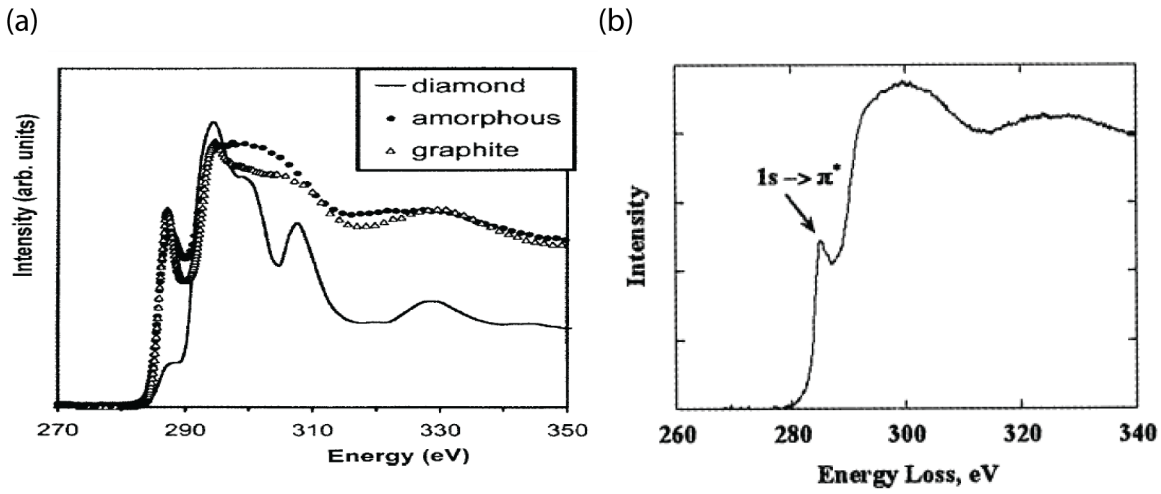

Figure 3.7: EELS C K-edge spectrum of (a) different allotropes of C: diamond, amorphous C and graphite,(*58*) (b) single crystals of single walled CNTs formed by self-assembly.(*59*)

and an EELS spectrum is collected from each pixel in the scanned area. The spot size and dwell time of the beam as well as the step size determine the resolution of the spectrum image, but there is a tradeoff between resolution and build up of contamination. A long dwell time collects more data at each pixel, but makes it more likely that the sample will drift or be contaminated since the electron beam attracts contaminants inside the chamber. The contrast observed in the spectrum image is an indication of the intensity of the spectrum at each pixel, and does not provide information about the elemental distribution within the scanned region. When analyzing EELS data, we subtract the background contribution of the tails of lower energy edges by approximating it with a power law to reveal the characteristic edge of the target element e.g. C K-edge shown in Figure 3.8(c). In order to do this, an energy window pre-edge must be selected. Once the background it removed, the

signal is revealed. Due to the nature of the EELS edge, where intensity decreases significantly at high energy losses, the signal is often integrated over an area of the sample to increase the signal to noise ratio. This curve-fitting model is based on the physics of particle interaction with the material.

The C K-edge of the sample reveals peaks at 285 eV and 290 eV (Figure 3.8(c)). Figure 3.8(d) shows a Gaussian fit of the C K-edge, which can be compared to that of activated carbon in Figure 3.8(e), the source material used in making covetics. Ratio of the peak intensities $\pi^*/(\pi^* + \sigma^*)$ indicates the degree of graphitization that is preserved upon conversion to covetics. The ratio for this sample is 0.125 compared with 0.126 in activated carbon and indicates that Cu covetics retain the graphitization of the source material. Additionally, though all carbon, such as that present in hydrocarbon contamination, leads to a rise in the C K-edge at 284 eV, the fine edge structure (shape) of the C K-edge obtained from Cu covetic is similar to that acquired from CNTs,(*59*) with an edge at 285 eV, further indicating that sp^2 (graphitic) C is present in Cu covetic samples.

Another approach to analyzing EELS spectrum images is to use the multivariate analysis method (MVA). In this approach, EELS spectra can be described as a parametric model, composed of a finite number of components with some noise. The most commonly used MVA method is principal component analysis (PCA). Decomposition algorithms including PCA and blind source separation (BSS) have been used to analyze the EELS spectra taken from materials that have elements with overlapping edges.(*60*) We have used MVA to elucidate the fine structure of the C K edge in Cu covetic samples and to distinguish between C contamination

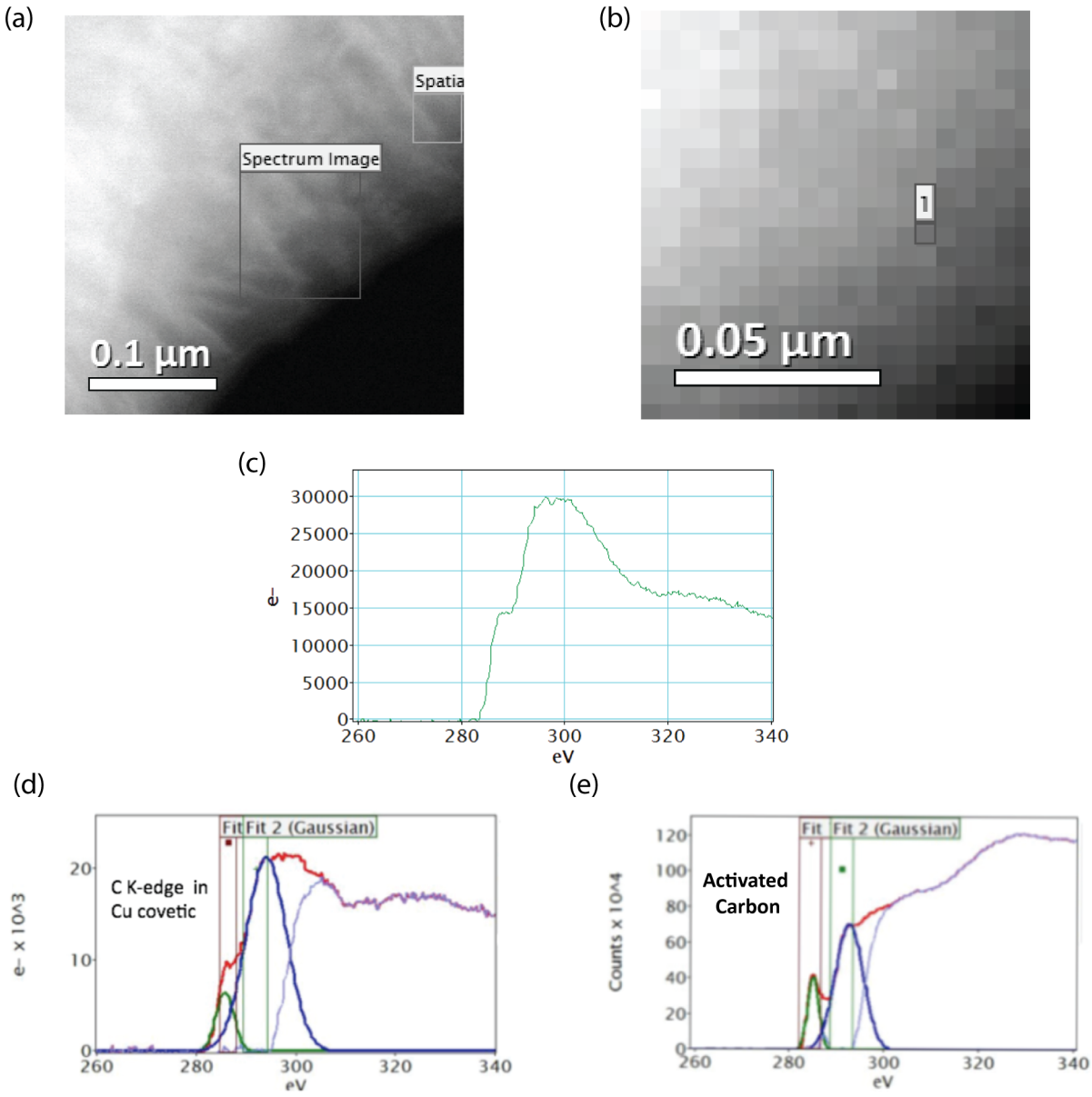

Figure 3.8: (a) HAADF image of Cu cv 5% bulk sample showing the regions where a spectrum image was obtained. (b) High magnification of spectrum image from the area shown in (a), (c) C K-edge after background subtraction of one pixel labeled 1 in (b) showing pre-peak at 285 eV and peak at 290 eV, (d) Gaussian fitting to edge in (c), (e) C-K edge of activated carbon fitted with Gaussian peaks

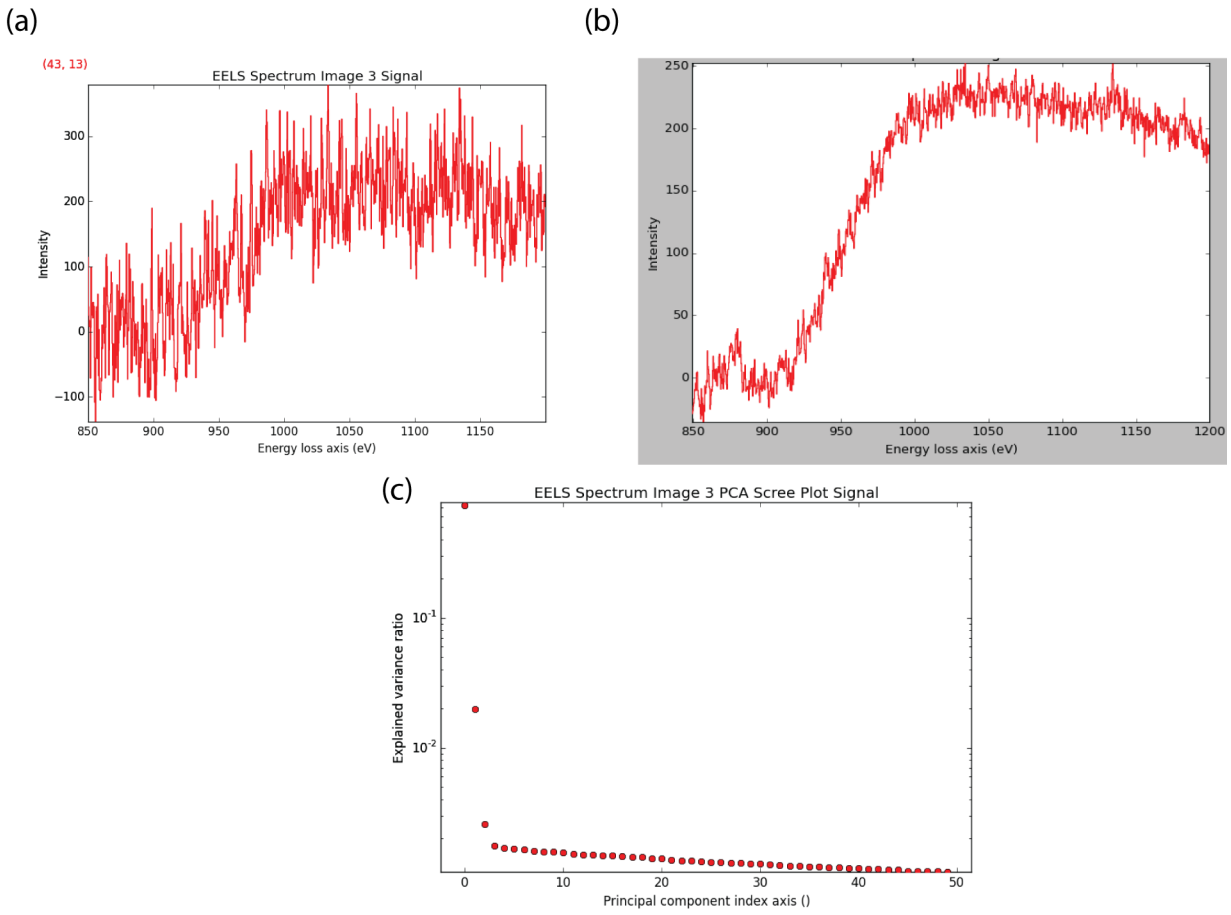

Figure 3.9: (a) EELS spectrum from a single pixel of the Cu M edge before decomposition, (b) Spectrum after PCA decomposition, (c) scree plot showing three principal components.

and C in the sample structure. The Hyperspy Python library provides convenient access to several algorithms, and was used to analyze EELS data in this thesis.(*61*)

Decomposition is primarily used to reduce the noise of a dataset or for dimensionality reduction. There are several methods to decompose a tensor into several factors; one of the most frequently used is PCA. We assumed a Gaussian distribution of the data and used PCA to denoise data by using a limited set of components

(principal) to make a model of the original dataset (spectra). Figure 3.9(a) shows an EELS spectrum of the Cu M-edge before decomposition using PCA. Removing higher components only has the effect of reducing the noise (3.9(b)). Several algorithms exist for performing PCA, such as singular value decomposition (SVD) as well as non-negative matrix factorization (NMF), but we have primarily used SVD in the data analysis because negative data points can be produced after background subtraction. PCA sorts the components in order of decreasing variance. The dimensionality of the data is estimated by plotting the variance against the component index in a logarithmic scale in what is termed a scree-plot (Figure 3.9(c)). The point at which the scree plot becomes linear is generally judged to be a good estimation of the dimensionality of the data and is therefore used as the number of components that should be retained to keep fidelity with the experimental dataset (in the example of Figure 3.9 there are three (3) components). Re-plotting the data with limited number of components, in fact, shows a reduction in the noise (Figure 3.9(b)), and yet resembles the original dataset (Figure 3.9(a)). The principal components are difficult to interpret physically, so PCA can only complement traditional mapping.

In order to obtain more physically meaningful components from the data decomposition, Blind Source Separation (BSS) was carried out on the dataset after decomposition. One instance of BSS is independent component analysis (ICA). ICA is a computational method that can separate mutually independent components from a mixture, and is generally used when conventional mapping techniques are challenging. The starting point of ICA is that the components are statistically independent and have non Gaussian distribution. By entering the number of prin-

cipal components that describe the data into an ICA algorithm, we were able to retrieve independent components that represent the different compounds present in the sample and the mixing matrix of their distribution. Hyperspy decomposes the dataset into a signal space and a navigation space. From these, we were able to resolve the contribution from each component. Figure 3.10 shows the decomposition of the spectrum image from Figure 3.8(b), where the spectra in 3.10(a) shows the signal space with three unique signals (components) in the region of the C-K-edge (250 - 350 eV). In conjunction with the navigation space in Figure 3.10(b), we have identified three distinct regions: carbon bonded in the Cu covetic, the background and copper. The C K-edge in the covetic region starts to rise at 284 eV as expected and shows clear peaks at 285 eV and 290 eV. This analysis corroborates the result obtained from peak fitting shown in Figure 3.8(d). The intensity in the background region is uniform throughout the region mapped and hydrocarbon contamination can be distinguished from C in covetic by the shape of the edge in the signal space, which should be similar to the carbon signal but without a defined sp^2 or sp^3 peak.

We investigated the inclusions observed in the optical images of a Cu cv 3% extruded rod (shown in Figure 3.1). Figure 3.11(a) shows an SEM image of the surface of the sample with the inclusions that are elliptical in shape and $\approx 1\ \mu m$ in diameter. They are persistent within the bulk structure as shown by the cross-section of the bulk sample (Figure 3.11(b)). We prepared a TEM lamella using FIB which included a few of these inclusions as shown in the low magnification TEM image in Figure 3.11(c). A higher magnification image of one such inclusion, shown in Figure 3.11(d), measures ≈ 830 nm $\times 1090$ nm. HRTEM image of a region

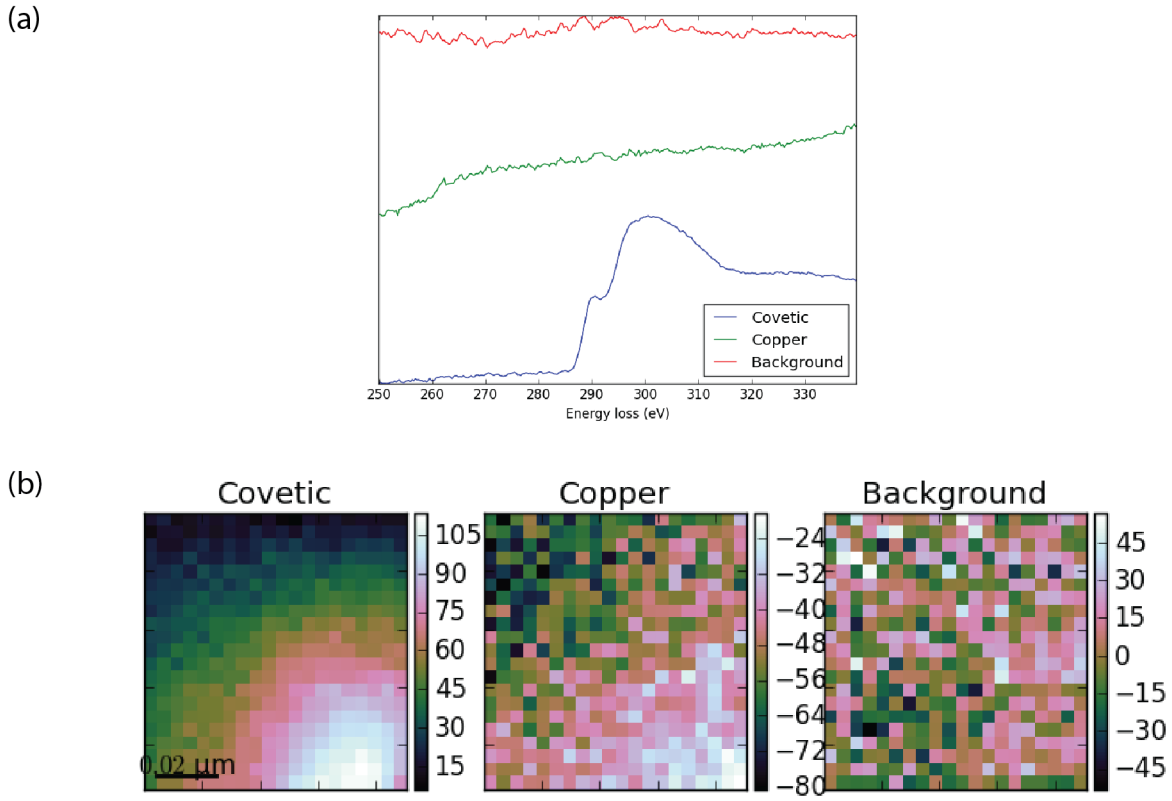

Figure 3.10: Decomposition of the C K-edge from the spectrum shown in Figure 3.8(b) resulting in the (a) signal space and (b) navigation space

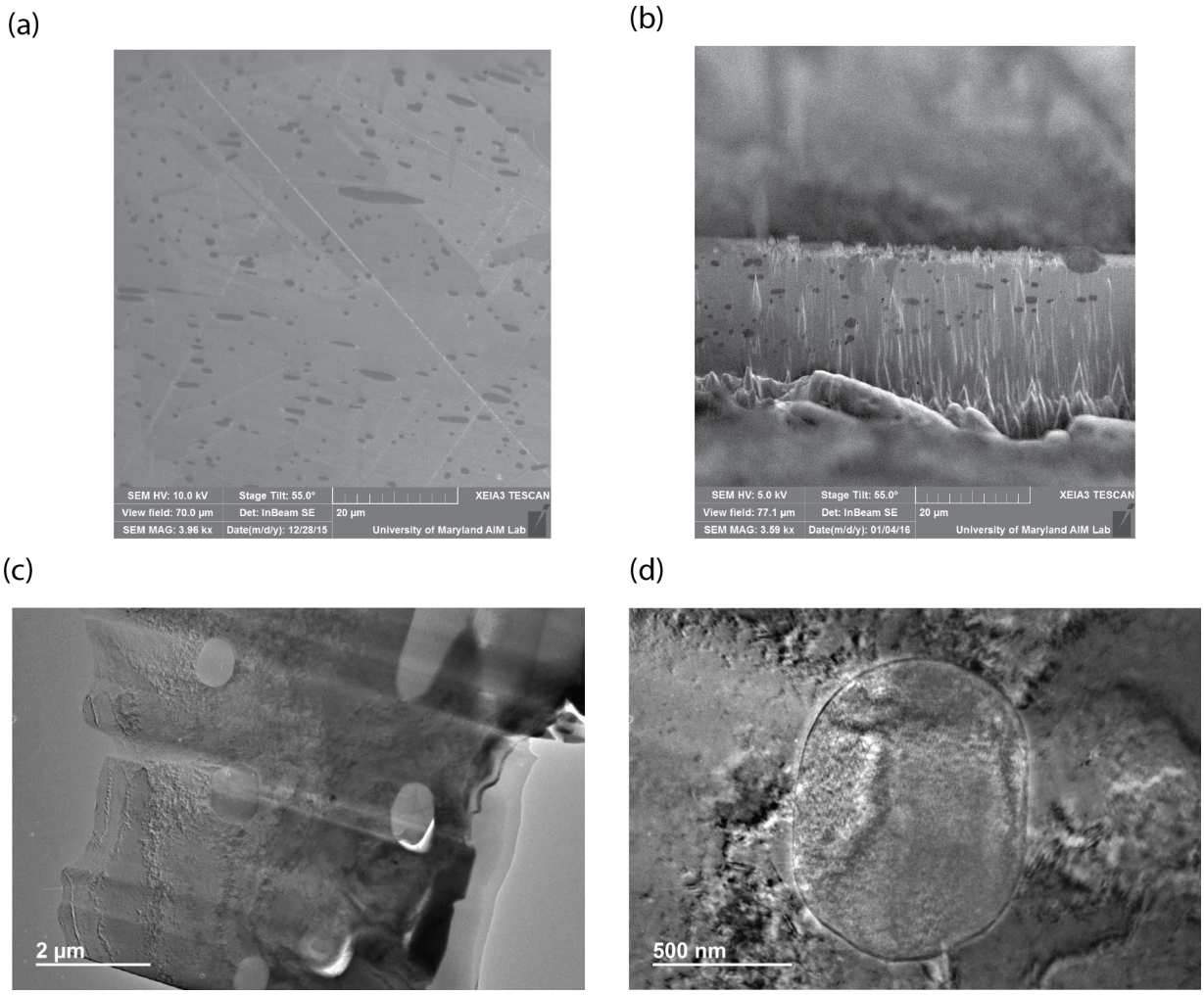

Figure 3.11: (a)SEM image of surface of a Cu cv 3% sample showing inclusions (b) Cross-section of the same sample showing that inclusions are persistent within the bulk, (c) Low magnification TEM image of lamella made from the same sample showing a few inclusions, (d) a single inclusion, elliptical in shape, measuring ≈ 830 nm $\times 1090$ nm

outside the inclusion with the $(1\bar{1}0)$ diffraction pattern in the inset (Figure 3.12(a)) indicates a region that has a d-spacing of 0.208 nm, which can be identified as Cu (111). The other crystallographic direction in the diffraction pattern (inset of 3.12(a)) has a d-spacing of 0.181 and corresponds to Cu (200). There are no satellite spots as observed in the modulated region of the Cu cv 5% sample (shown in Figure 3.6(a)). However, diffraction from the region inside the inclusion (inset of 3.12(b))) reveals new reflections with d-spacing of 0.233 nm and 0.283 nm, which are neither associated with Cu or either of its oxides, and one orientation Cu (200) that is common to the region outside the inclusion. HRTEM image of an area within the inclusion (3.12(b)) shows a region that corresponds with the new reflections, d = 0.233 nm and 0.283 nm.

TEM-EDS taken outside and inside the inclusion are shown in Figures 3.12(c) and 3.12(d) respectively. No C peak is observed outside the inclusion (0 ± 0.18 wt.%), while 2.33 ± 0.23 wt.% (7.78 at.%) C is measured inside the inclusion. It is therefore likely that C incorporation in these regions leads to a change int eh structure of Cu allowing for new reflections in the electron diffraction pattern.

EELS spectra were acquired within the inclusion where C is known to be present with a spot size of 1 nm, step size of 0.7 nm, dwell time of 0.5 sec/pixel and a dispersion of 0.3 eV/channel. Decomposition of the C K-edge of the Cu cv 3% is shown in Figure 3.13. Four components are identified from the navigation and signal space. There are two regions labeled Carbon 1 and 2 in Figure 3.13(a), which have similar spectral profile in Figure 3.13(b), but with slightly different energy. We expect the C edge to start to rise at 284 eV, as shown in the spectra labeled

(a)

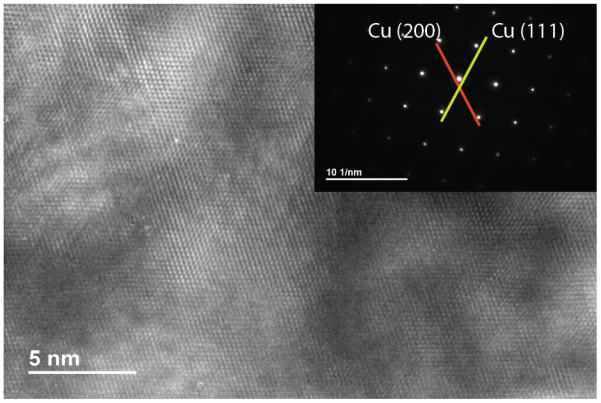

(b)

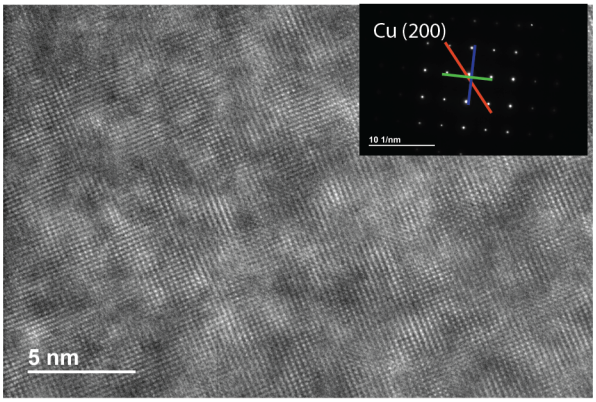

(c)

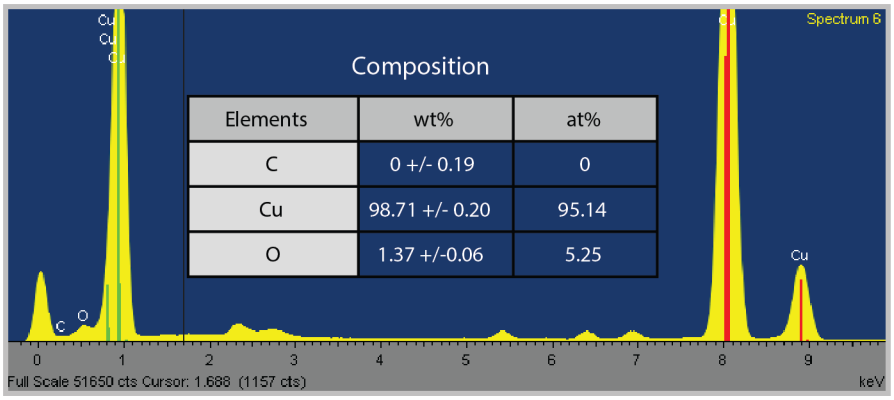

(d)

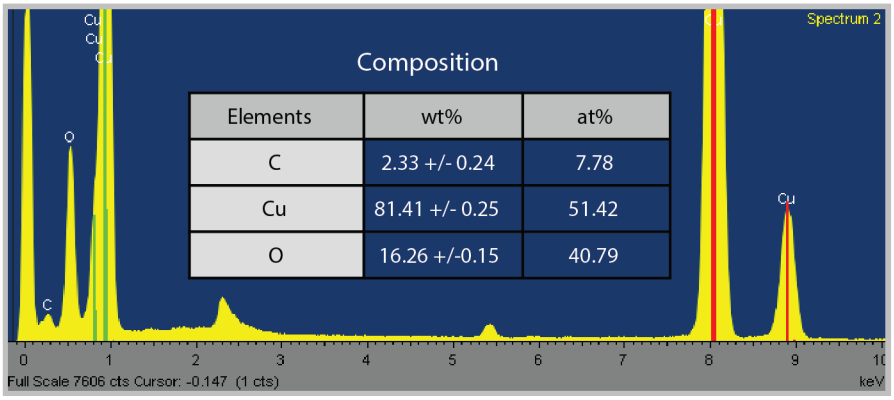

Figure 3.12: HRTEM image of a region outside the inclusion. The inset of (a) is the $[1\bar{1}1]$ electron diffraction pattern from the same region, (b) HRTEM image of a region inside the inclusion with a d-spacing measuring 0.233 and 0.283. The inset of (b) is an electron diffraction pattern taken inside the inclusion. TEM-EDS spectrum of regions (c) outside and (d) inside the inclusion, showing 0 wt.% and 2.33 wt.% C respectively.

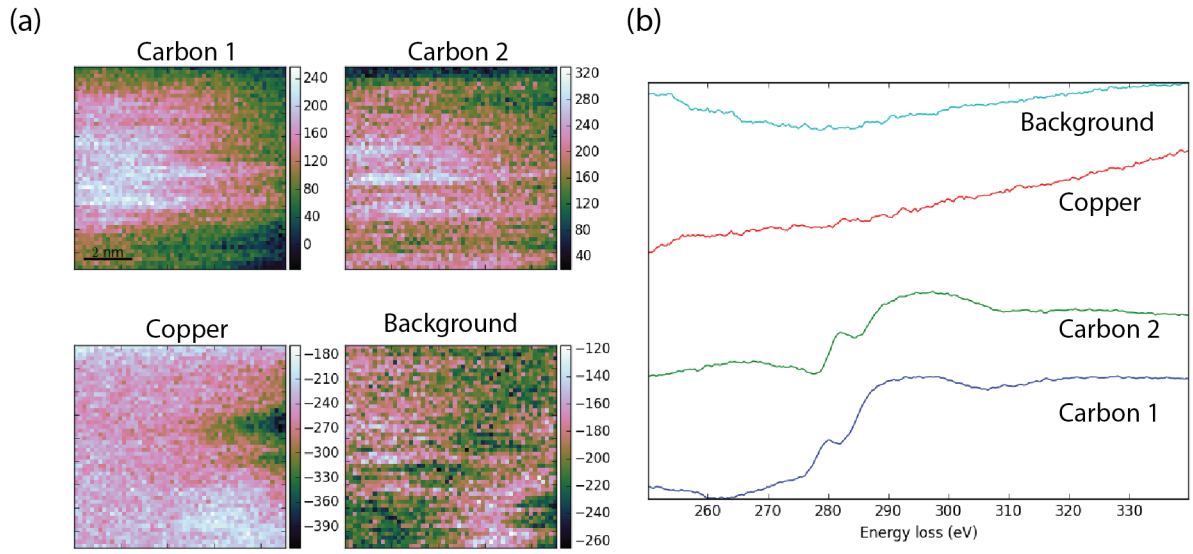

Figure 3.13: Decomposition of the C K-edge from the inclusion in the Cu cv 3% sample resulting in the (a) navigation space and (b) signal space

"Carbon 2", but the spectra labeled "Carbon 1" starts to rise at a lower energy. This difference in energy between "Carbon 1" and "Carbon 2" is indicative of carbon that is in two different environments such as Cu-C and C-C. We have also identified regions associated with Cu and the background signal as indicated.

3.1.1 Modeling Bulk Cu covetics

In attempting to model the structure of Cu covetics we were informed by the modulation observed in TEM. Modulation suggests a layered structure, and as such we sought to combine Cu with C in the form of graphene. Cu has a face-centered cubic (fcc) structure with a lattice constant of 0.3610 nm. Graphene is hexagonal with C-C interatomic separation of 0.142 nm. The lattice mismatch between the Cu

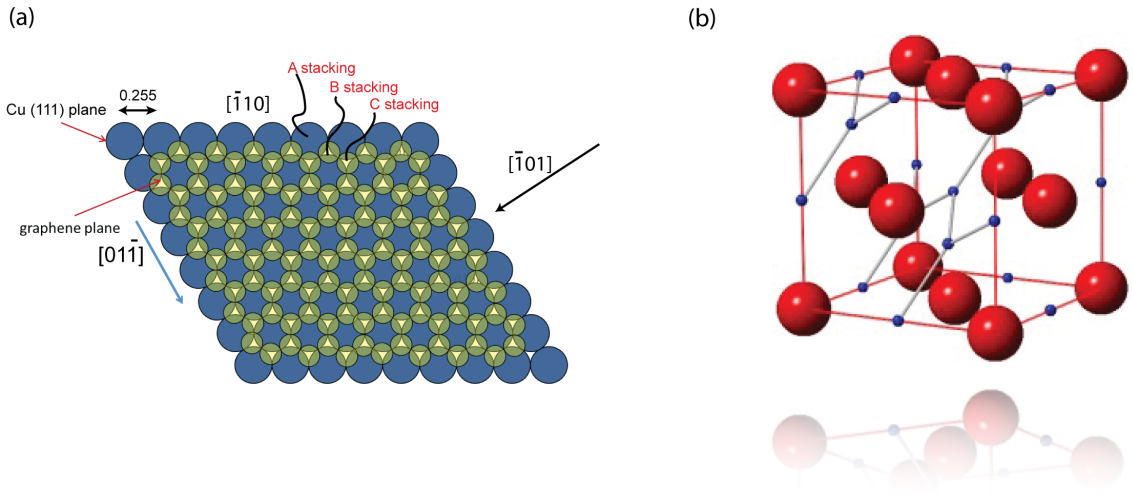

Figure 3.14: (a) 2D model showing the graphene plane (yellow) superimposed on the B and C sites of the Cu (111) plane (blue), (b) 3D model showing the C atoms (blue) at the interstitial sites in the Cu (red) fcc lattice

low potential sites on the (111) plane and the C-C interatomic distance in graphene is only 3%, thus, graphene fits well in the interstitial sites of the Cu (111) plane as shown in Figure 3.14(a). The challenge is that unbonded, Cu has an atomic radius (r_{Cu}) of 128 pm and C (r_C) of 77 pm. If we assume the C is incorporated into the interstitial positions of the Cu fcc matrix (Figure 3.14(b)) the interatomic distance would be $d_{Cu-C} = a/2 - r_{Cu} - r_C = -0.0245$ nm, so there is not enough space to accommodate C in Cu. Additionally, the next layer of Cu in the A/B/C stacking of fcc Cu lies on top of the C atoms on the (111) plane.

Another model of Cu covetic was developed using Density Functional Theory (DFT) by Sergey Rashkeev. In order to investigate the role of different atomic scale and nanoscale features in the epitaxial accommodation of graphene layers and graphene ribbons on the Cu surfaces and between layers with (111) orientation, a

significant number of different graphene–Cu periodic supercells were constructed and their geometries optimized using DFT. We used "slab" supercells (three layers of graphene on top of four layers of Cu (111). A periodic hexagonal supercell with parameters: $a = 1.475$ nm and $c = 3.010$ nm was used. The value of the parameter a corresponds to ≈ 5 lattice constants of the 2D periodic structure in Cu (111) plane and ≈ 6 lattice constants of the graphene structure, which reasonably takes into account most of the lattice mismatch between the two structures. For slab supercells, a vacuum layer was added between slabs of ≈ 1.6 nm in the c direction which guarantees that different slabs will not overlap. The positions of Cu atoms in the lower layer of the slab (opposite to the "free" graphene surface) were fixed. The DFT calculations were based on the generalized gradient approximation (GGA) for exchange and correlation, and plane waves.(*62*) The GGA functional of Perdew, Burke, and Ernzerhof (PBE) was used, which gives good results for chemisorption of molecules at transition metal surfaces.(*63*) Projected augmented wave (PAW) scalar relativistic pseudopotentials (*64*)(*65*) and the VASP code (*66*)(*67*) were used. The energy cut-off for the plane-wave basis was set at 500 eV, and all integrations over the Brillouin zone were done using the Monkhorst–Pack scheme with one to four k points in the relevant irreducible wedge.(*68*) Inclusion of additional k points were found to have minimal effect on the total-energy differences of interest. The total number of atoms varied between 300 and 750 atoms for different periodic supercells. For each supercell, all atoms were relaxed until the quantum-mechanical force on each atom became smaller than 0.02 eV A^{-1}. Most of the calculations were spin-polarized. Activation barriers were calculated using the nudged-elastic-

band (NEB) method.(*69*) In some cases (when the potential energy curve was very steep around the transition state) the adaptive NEB approach was employed,(*70*) because the conventional NEB sampling did not provide satisfactory results. The pre-exponential factors and reaction rates were not calculated for the considered reactions. Although such calculations could be performed,(*71*) they are very difficult and time consuming. Comparison between the activation barriers at different surface sites provides only qualitative information which is quite sufficient for most of the practical purposes.

We found that if the graphene sheets are perfect, there is no bonding between the metal layers and the graphene sheet, because all the C-C bonds in perfect graphene are satisfied. Conversely, if periodic defects are introduced into the interfacial graphene layer then, there are unsatisfied bonds, and bonding between the Cu atoms in the metal layer and C atoms in the graphene sheet at the defect sites takes place as shown in Figure 3.15. The presumption of defects in the Cu covetic structure is not an unreasonable one since our EELS spectra indicate a weak peak in the C K-edge at 285 eV corresponding to transitions from the 1s occupied state to the π^* unoccupied state in sp^2 graphitic carbon. Incorporating a large amounts of C into the Cu structure could also create point defects, dislocations and stacking faults in the lattice.

First principles calculations of the dynamic matrix for this structure provides the phonon density of states as well as any bonding (covalent or metallic bonding) present in the final structure. We can identify atoms associated with each peak in the plot of the calculated phonon density of states as a function of energy. The

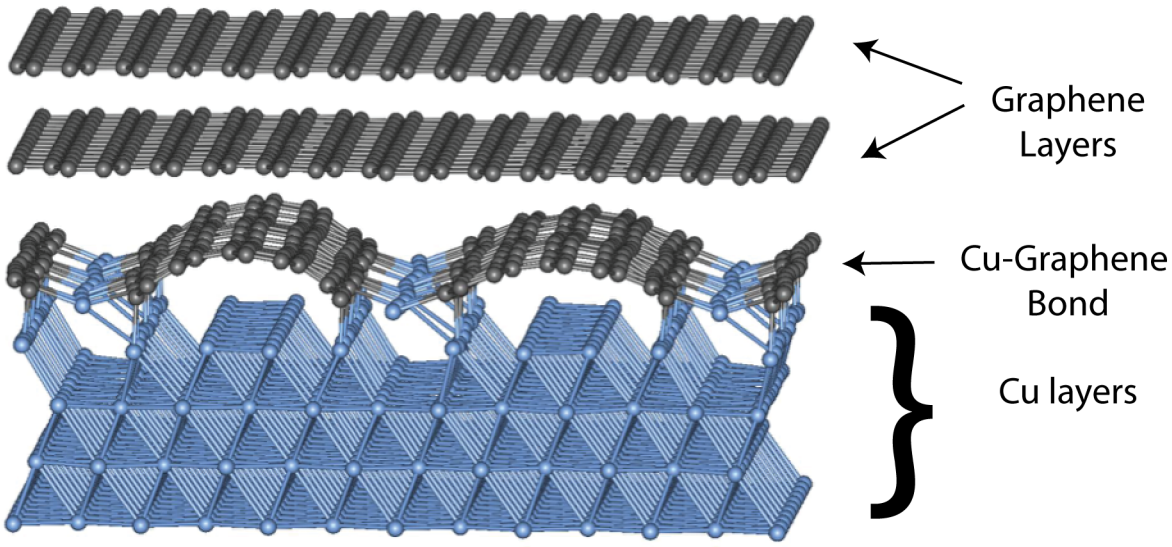

Figure 3.15: DFT model of the covetic supercell after relaxation to the lowest energy state

modes could be symmetric or asymmetric and may be either Raman or Infrared (IR) active, which gives us a tool to verify the simulated structure experimentally.

In order to compare Raman spectra from Cu covetic it is instructive to first analyze the Raman spectra of Ag covetic since these show very clear presence of graphitic carbon. Raman spectroscopy of Ag cv 6% shows clear D and G graphitic peaks in all 20 points along a 300 μm line that was integrated twice using 600 grating for 6 seconds as shown in Figure 3.16 (a).(*72*) The G band, typically located from 1,540 - 1600 cm^{-1}, is observed at $\approx 1,601 cm^{-1}$ in the average spectrum from the 20 points in Figure 3.16(a) and corresponds to the E_{2g} mode at the BZ center of nanocrystalline graphite.(*73*) This is highly indicative of not only having highly ordered carbon species infused in metal, but also a high ratio of sp^2 to sp^3 bonding and high strain.(*73*)(*74*) The D band at 1,354 cm^{-1}, normally in the range 1,300

- 1,400 cm^{-1}, corresponds to defects and is active in defective graphite, amorphous carbon, carbon nanotubes, and at the edges of graphene but is not observed in perfect graphite or diamond.(*75*) The peak at 2,625 cm^{-1} in the Ag covetic sample corresponds to the G^* overtone of the D mode of graphite (also known as 2D). In contrast, Raman spectra of 10 points on Cu cv 5% along a 400 μm line integrated twice using 600 grating for 30 seconds, do not show D or G peaks (Figure 3.16(b)). However, we are probing inclusions that are ≈ 1 μm in diameter, so Raman spectra every 40 μm is not likely to be probing regions with significant C content. Additionally, half of the spectra have peaks at 525 cm^{-1} and 615 cm^{-1}, which are known to correspond to the Cu_2O phase.(*76*)(*77*), but the broad peak from 300 - 700 cm^{-1} is associated with C-Cu bonding modes. Phonon density of states calculations suggest that D and G peaks should arise if there are two or more layers of graphene above the interfacial layer containing graphene nanoribbons over the metal, as is the case in Ag covetics where two layers of graphene above the bonded layer in the supercell produces a good fit to the data (Figure 3.16(c)). However in the case of Cu covetics, the best fit to the Raman spectra is achieved when only the layer with the graphene ribbons is bonded to the metal with no unbonded layers present above the bonded layer (Figure 3.16(d)). This leads us to believe that the structure of Cu covetic may be different from Ag covetic, possibly due to the smaller space to accommodate the C atom in copper compared to silver.

We modeled the inclusion structure using CrystalMaker®: a crystal and molecular structures modeling program for Mac and Windows. We started with a 3 x 3 x 3 unit cell fcc structure of Cu with A/B/C/A... stacking and replaced the B and C

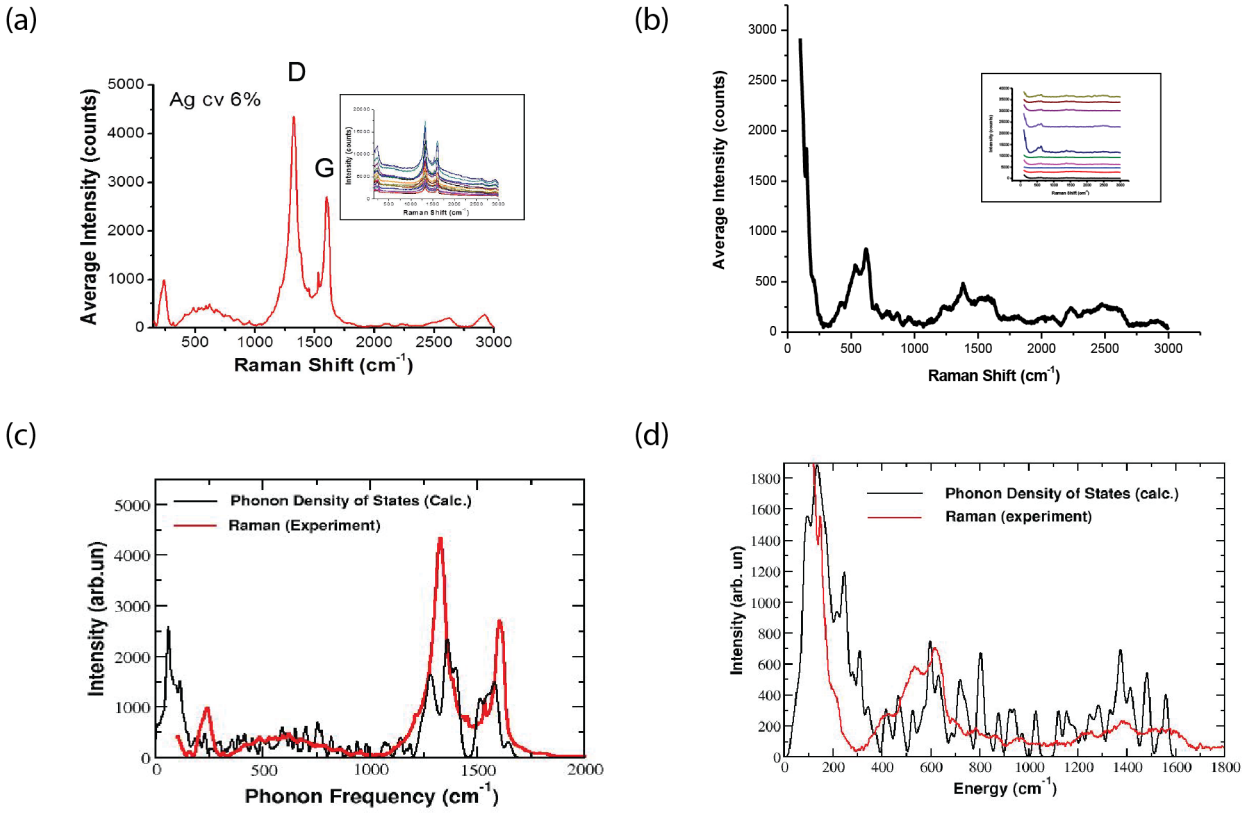

Figure 3.16: (a) Average Raman Spectrum from 20 points along a 300 μm line from Ag cv 6%, each spectrum is shown in the inset, (b) Average Raman spectrum from 10 points along a 400 μm line of a Cu cv 5% sample with each spectrum is shown in the inset, (c) Phonon Density of states shows a good fit with the experimental data acquired in (a), (d) Phonon density of states plotted with the experimental average data in (b) indicates the best fit occurs when only one layer of graphene nanoribbons is bonded to the top Cu plane.

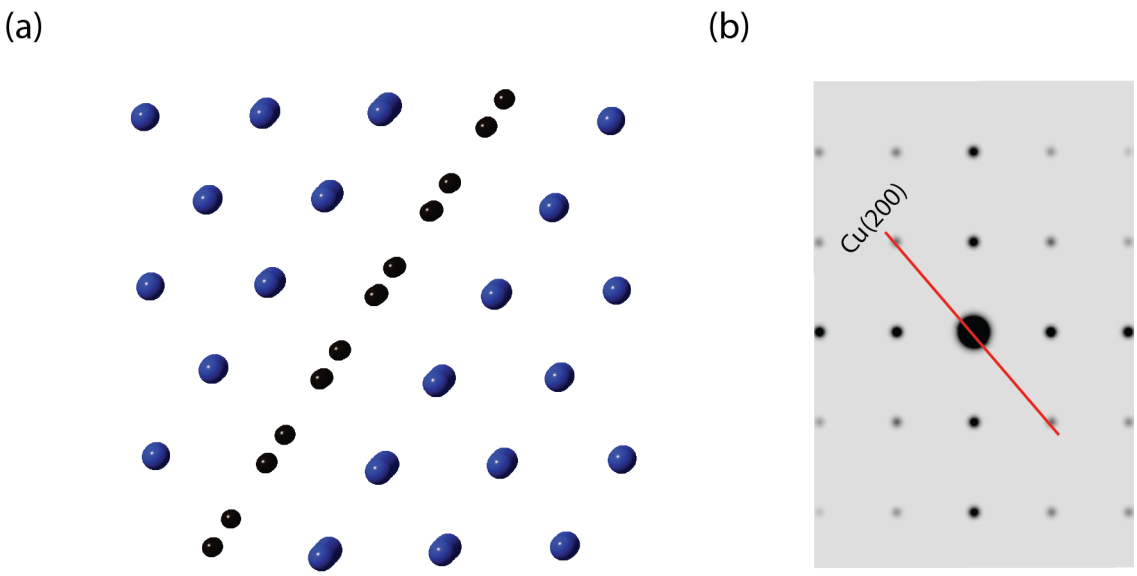

Figure 3.17: Model of the Cu covetic generated using CrystalMaker®, (b) simulated electron difraction pattern from the structure in (a) using SingleCrystal™

layers of Cu with a graphene sheet (G). This solved the problem where the B layer of Cu sits on top of the C atoms in the graphene plane. The resulting structure has a stacking of A/G/A/B/C... as shown in Figure 3.17(a) where the Cu atoms are colored blue and the C atoms in the graphene layer are colored black. Performing electron diffraction on this structure in SingleCrystal™ produces the diffraction pattern shown in Figure 3.17(b), which is in agreement with that observed from inside the inclusion (inset of Figure 3.12(b)). The symmetry and angles agree with these experiential results and as such we propose this as a likely structure of Cu coveitcs.

3.1.2 Electrical Properties of bulk Cu covetic

Given evidence for graphene-like structures in Cu covetics we investigated the effect this had on the electrical conductivity. Numerous attempts have been made to design new materials with higher conductivity than copper (5.8×10^5 S/cm) and with higher resistance to oxidation. However, many of the new conductors, though impressive in some characteristics have yet to surpass the conductivity of Cu. For example, CNTs have shown electrical conductivities of 3×10^4 S/m,(*6*) and CNT-Cu composites have shown conductivities of $2.3 - 4.7 \times 10^5$ S/cm.(*5*) In order to compare the conductivity of Cu covetic with other novel conductors, bulk Cu covetic with nominal C content of 3%, 5% and 9% was drawn into 8 gauge wires and the electrical resistivity measured. The weight of each wire was measured using a triple beam balance. Assuming the density of copper does not change with C content, the volume was calculated. The area was calculated from the diameter of each wire, measured using a micrometer and reported as the average of 4 points along the length. The volume and area were used to calculate the length of the wires. Each wire was anchored between two busbars and I-V measurements made. Each data point is the average of 4 measurements and used to calculate the resistance. The error in the resistivity was calculated from the errors in the diameter and I-V data using Eq 3.1 for the standard deviation of the mean (σ_x),

$$\sigma_x = \sqrt{\frac{1}{N-1}} \sum_{i=1}^{N} (x_i - \bar{x})^2 \tag{3.1}$$

Table 3.3: Measured quantities used in the resistivity calculation of Cu cv 3%, 5%, and 9% wires compared to pure copper.

Sample Conc. (%)	Weight (g)	Diameter (cm)	Resistivity (Ohm-cm)	Conductivity (S/cm)
3	430.3 ± 0.5	0.3269 ± 0.0004	$1.8 \times 10^{-6} \pm 3 \times 10^{-8}$	5.6×10^{5}
5	403.5 ± 0.5	0.3256 ± 0.0004	$1.77 \times 10^{-6} \pm 3 \times 10^{-8}$	5.65×10^{5}
9	430.1 ± 0.5	0.3251 ± 0.0004	$1.72 \times 10^{-6} \pm 3 \times 10^{-8}$	5.81×10^{5}

where N is the number of measurements and x is the value of each measurement. Table 3.3 presents the measured resistivities and conductivities for three samples with different C concentrations compared to a pure copper wire and indicates that the resistivity of Cu covetic first increases for 3% and then decreases with increasing C content for 5% and 9%. Figure 3.18 shows the electrical conductivities of Cu cv 3% compared to Cu metal as a function of temperature; measured using a Physical Property Measurement System (Quantum Design) with a temperature range from 1.5 K - 350 K. Cu cv 3% has a similar temperature dependence as the Cu metal, but at a higher slope.

Given the electrical properties of bulk Cu covetic wires, we sought to investigate whether it would be possible to transfer carbon from the bulk into thin films and how carbon would affect the optoelectronic properties of these films. We first deposited Cu covetic and pure Cu films by e-beam deposition. Though these films

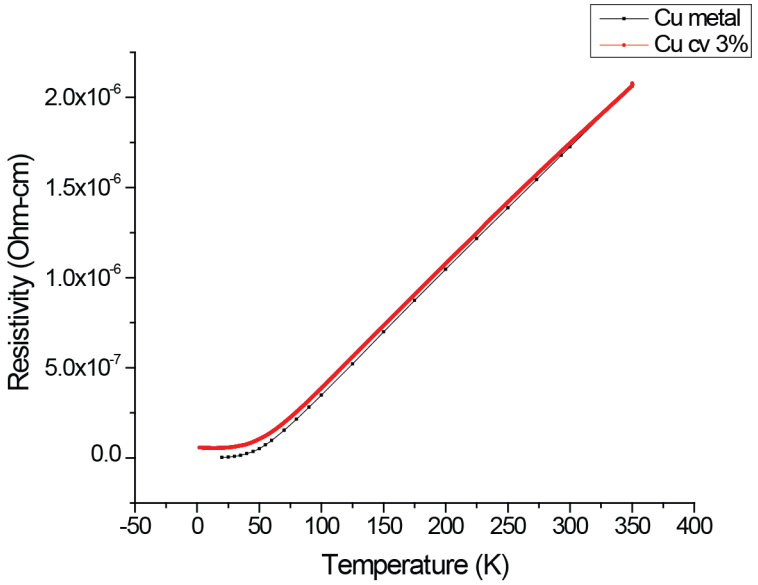

Figure 3.18: Electrical conductivity of Cu cv 3% and Cu metal wires as a function of temperature

showed higher transmittance and resistance to oxidation, their carbon content was negligible. Therefore, we decided to deposit films by PLD to asses if this technique would give flms with higher C content and better properties. Next chapter presents the results of the films.

Chapter 4: E-beam deposited Films

4.1 Structural Characterization

Cu cv 5% films grown by e-beam deposition on Si (100) using pieces of the bulk Cu cv 5% sample as target exhibit 1.24% C concentration as measured by SEM-EDS shown in Figure 4.1(a). This value is higher than the actual C concentration because of carbon contamination on the surface of the sample since the vacuum in the SEM is not as high as in XPS. AFM height image (Figure 4.1(b)) of the same film shows a smooth surface, exhibiting an average RMS roughness of only 1 nm which can also be seen in the HRTEM image of Figure 4.1(c) for an 18 nm thick Cu cv film. The XRD spectrum from this sample shown in Figure 4.1(d) exhibits crystalline structure with Cu (111) preferred orientation. The crystalline grains form a columnar structure where the grains extend from the interface with the Si substrate to the film surface. No copper oxide or any of the allotropes of carbon are present in either TEM or XRD. Very low C content is also observed from the EELS Spectrum of another 20 nm Cu cv 5% shown in Figure 4.2. Figure 4.2(a) shows a HAADF image consisting of the substrate with dark contrast and Pt with bright contrast. The region analyzed lies between these two layers and includes the film as well as a thin area of the substrate and is demarcated with the green box.

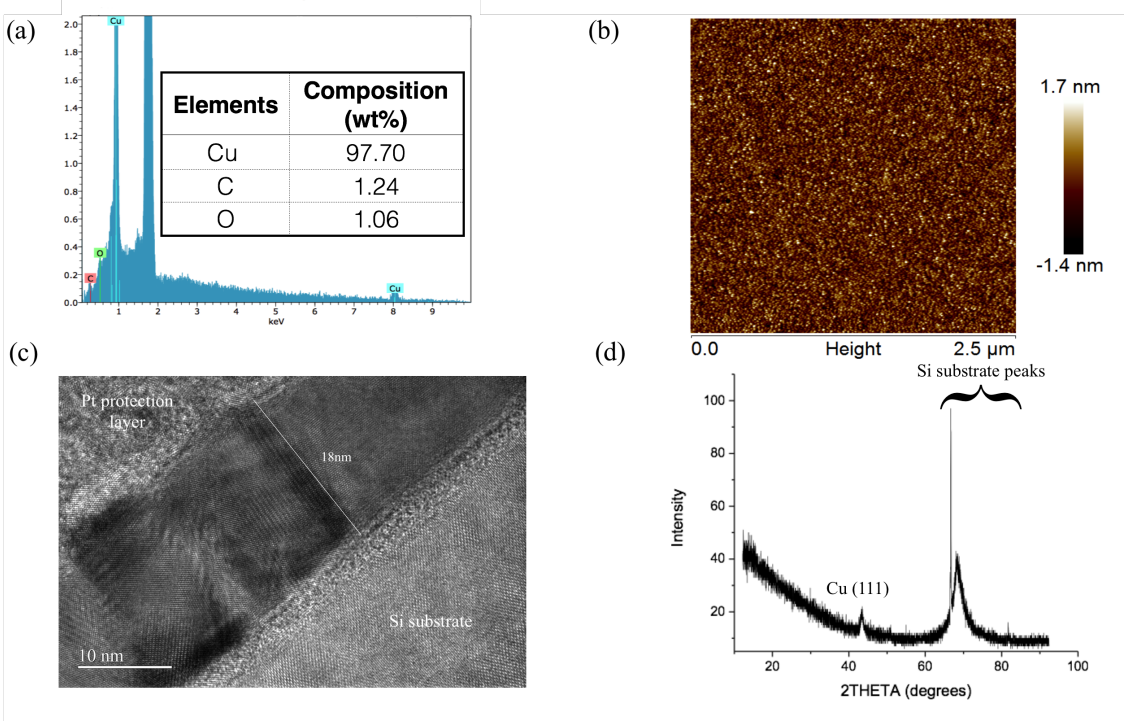

Figure 4.1: (a) SEM-EDS of an 18 nm thick Cu cv 5% film deposited by e-beam on Si. (b) AFM of surface of the film with roughness ≈1 nm (c) cross section HRTEM image of a region within this film, (d) XRD spectrum of the same film displaying a crystalline structure with Cu [111] texture.

The EELS spectrum image was acquired using a spot size of 1.5 nm, step of 1 nm, dwell time of 1 second and dispersion of 0.3 eV/channel and is shown in (Figure 4.2(c)). At each pixel in the image a spectrum is acquired. The sum spectrum of the film layer indicated in the red rectangle is shown in Figure 4.2(b) and individual maps of the constituent elements Cu M-edge, C K-edge and O K-edge in Figure 4.2(d)-(f) respectively. Figure 4.2(g) shows line profile of these elements. Cu is present throughout the region as expected, and there are notably weak but extended regions containing C in the film, and small amounts of O present, predominantly at the interface with the Si substrate where we expect the native SiO_2. Clearly, bulk covetic carbon structures cannot be transferred as-is to the thin film using e-beam evaporation. Since we could not obtain an accurate value of the C content (< 1 at.%) in the films we refer to the nominal concentration of the bulk Cu covetic target used for film deposition. Nevertheless, the presence of carbon in the copper matrix in the e-beam deposited films is evident by the improved properties compared to pure Cu films shown below.

4.1.1 Optoelectrical properties of e-beam deposited films

In order to measure the optical properties, films were deposited simultaneously on Si and glass substrates as can be observed in Figure 4.3(a).(*78*) Figure 4.3(b) compares the transmittance of Cu covetic to Cu metal films, measured at wavelengths ranging from 250 to 1100 nm. The peak at $\approx$ 580 nm is due to the spectral nature of Cu. At this wavelength the reflectance increases and absorbance

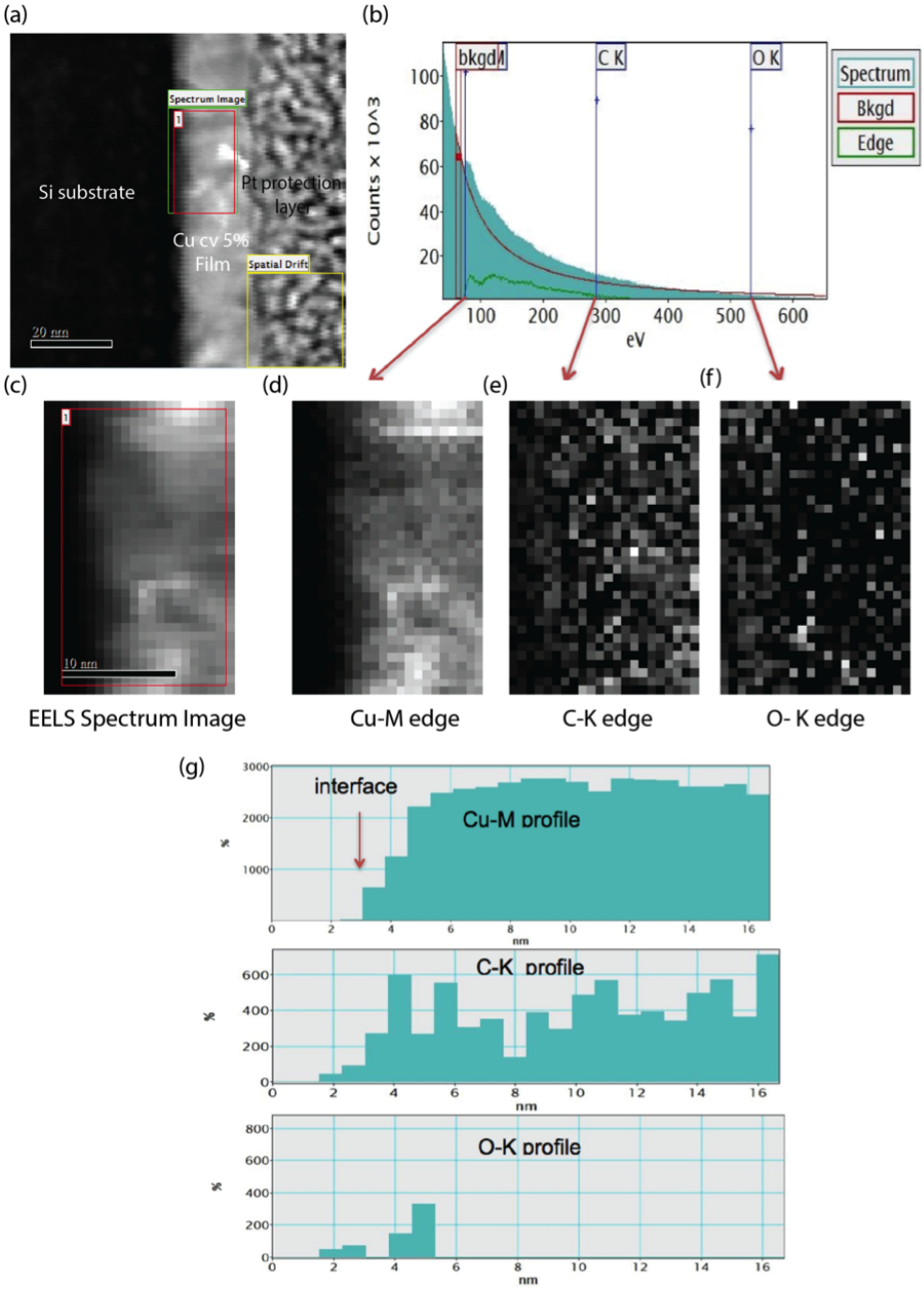

Figure 4.2: (a) HAADF survey image showing target region for EELS spectrum imaging in green and spectra sum in red, (b) integrated spectra of the target (red) region showing Cu M-edge, C K-edge and O K-edge, (c) Magnified spectrum image of target region. Maps of (d) Cu M-edge, (e) C K-edge, (f) O K-edge and (g) line profiles of the Cu, C and O respectively.

decreases more significantly. (*79*) Calculations by Ramirez-Porras et al. for copper suggest that at long wavelengths free carrier absorption dominates, but this effect decreases with wavelength due to screening by free carriers, which increases the reflectance (decrease in transmittance). At short wavelengths, reflectance is low and absorption dominates due to excitation of d-electrons into the conduction band. The combined effect gives rise to a crossover with a maximum at ≈ 580 nm. This peak is also observed in the e-beam Cu cv 5% films. Remarkably, Cu cv 5% films are consistently more transparent than pure Cu films of the same thickness. The greater transparency in the covetic films may be due to the filling of interstitial sites in the Cu lattice resulting in a lower reflection coefficient. It is also possible that the additional electrons from the incorporation of carbon atoms in the covetic films raise the Fermi level, blocking the optical transition and increasing the transmittance.(*78*)

In order to ascertain the electrical properties and stability of the Cu and e-beam Cu covetic films, contacts were made by painting silver stripes onto the samples. The films were kept in air at room temperature and periodic measurements of the resistivity of the films were taken to assess the progression of the electrical properties with time. Covetic films show a perpetually lower resistivity than pure copper films of the same thickness (Figure 4.3(c)). The resistivity of the pure 10 and 20 nm Cu films degrades rapidly with time, while the 30 nm Cu film is stable over the time tested. The 20 and 30 nm covetic films are stable up to almost 80 days after deposition, but the resistivity of the 10 nm Cu covetic film increases quickly with time although not as much as the 10 nm Cu film. This is attributed to a 10% variation in thickness given by the RMS roughness of the 10 nm covetic film, which

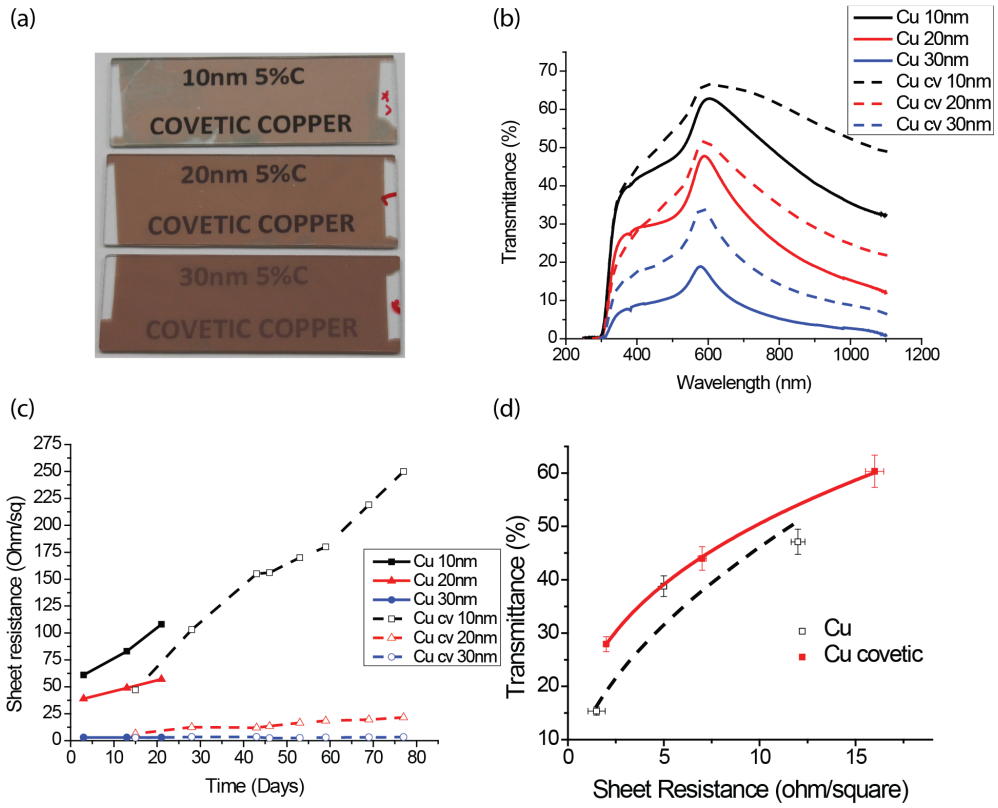

Figure 4.3: (a) Optical Image of 10 nm, 20nm and 30 nm e-beam Cu covetic films (b) Transmittance measurement comparing Cu metal (0% C) with e-beam nominal Cu cv 5% films of 10, 20 and 30 nm thickness. (c) Stability measurement comparing the resistivity of Cu metal with Cu cv 5% films in air. (d) Transmittance vs. sheet resistance of the e-beam covetic and Cu films measured at 550 nm

would significantly increase the surface area for oxidation and therefore degradation. The 20 and 30 nm Cu covetic films, in contrast, show very stable resistivity with time compared to the Cu films. The 20 nm covetic film also has relatively high transmittance above 50% at about 600 nm although it is lower for other wavelengths. The maximum transmittance of 65% for the e-beam films was achieved in the 10 nm Cu covetic film, as shown in Figure 4.3(b). It is well known that nanostructures such as graphene and CNT's have high electron mobility;(*12*) however, highly conductive films formed from carbon nanostructures are obstructed by a high contact resistance at each CNT junction or through each graphitic plane.(*48*) Previous DFT calculations of the interface between graphene and metal substrates show that the electronic structure of graphene is preserved by weak adsorption on Cu substrates.(*80*),(*81*) We believe that in Cu covetic the electronic structure of graphene is not preserved since there is some bonding between C and Cu and we do not have perfect graphene within the metal lattice.

For thin metal films, the relation between optical transmittance (T), and sheet resistance (R_s) can be modeled using Eq.4.1.(*41*)

$$T = \left(1 + \frac{188\sigma_{opt}}{R_S\sigma_{DC}}\right)^{-2} = \left(1 + \frac{188}{R_S r}\right)^{-2} \tag{4.1}$$

The figure of merit is defined as the ratio (r) of the DC conductivity (σ_{DC}), and the optical conductivity (σ_{opt}). Cu covetic films demonstrate higher figure of merit than copper metal films, namely; r = 79 and 105 for the 30 nm Cu and Cu covetic films, respectively (see Figure 4.3(d)). The electrical degradation of copper films with time is due to the formation of an insulating oxide layer on the film's surface as has been

observed in Al films that were exposed to air.(*82*) Tian et al,(*15*) have shown that the presence of graphene on a Cu surface can be an impenetrable barrier against oxidation. Unfortunately, the bonding between graphene and the copper surface is via van-der Waals forces and, consequently, it is very weak. In contrast, carbon in Cu covetic films provides resistance to oxidation by forming a network throughout the copper lattice with a strong bond between the carbon and the copper atoms. An oxide layer still develops on Cu covetic films, but with a slower rate than pure metal. It is possible however, that higher C content in the film will improve the resistance to oxidation even further.

A Cu cv 15% (nominal C content) was used as a target to deposit films via e-beam deposition in a similar manner to the Cu cv 5% films described above. XPS measured an average C concentration of 3.67 at.% (0.72 wt.%), in the bulk samples. Notably the bulk concentration measured in the sample with nominally 15% C is significantly less than was measured in the Cu cv nominally 5% (15 at.% = 3.2 wt.%)). A similar trend of transmittance can be observed in the case of the Cu cv 15% compared to the Cu cv 5% as shown in Figure 4.4(a). The peak transmittance at 550 nm is approximately the same for both, except in the case of the 10 nm films where the Cu cv 5% is slightly higher. Overall the Cu cv 15% exhibits flatter transmittance at higher wavelengths. 4.4(b) shows stability measurement of the 20 nm and 30 nm films shown in 4.4(a) over a period of 40 days, where the 30 nm film is more stable.

We investigated the role of temperature on the opto-electrical properties, by comparing Cu cv 15% films deposited at room temperature (25^0 C) and high tem-

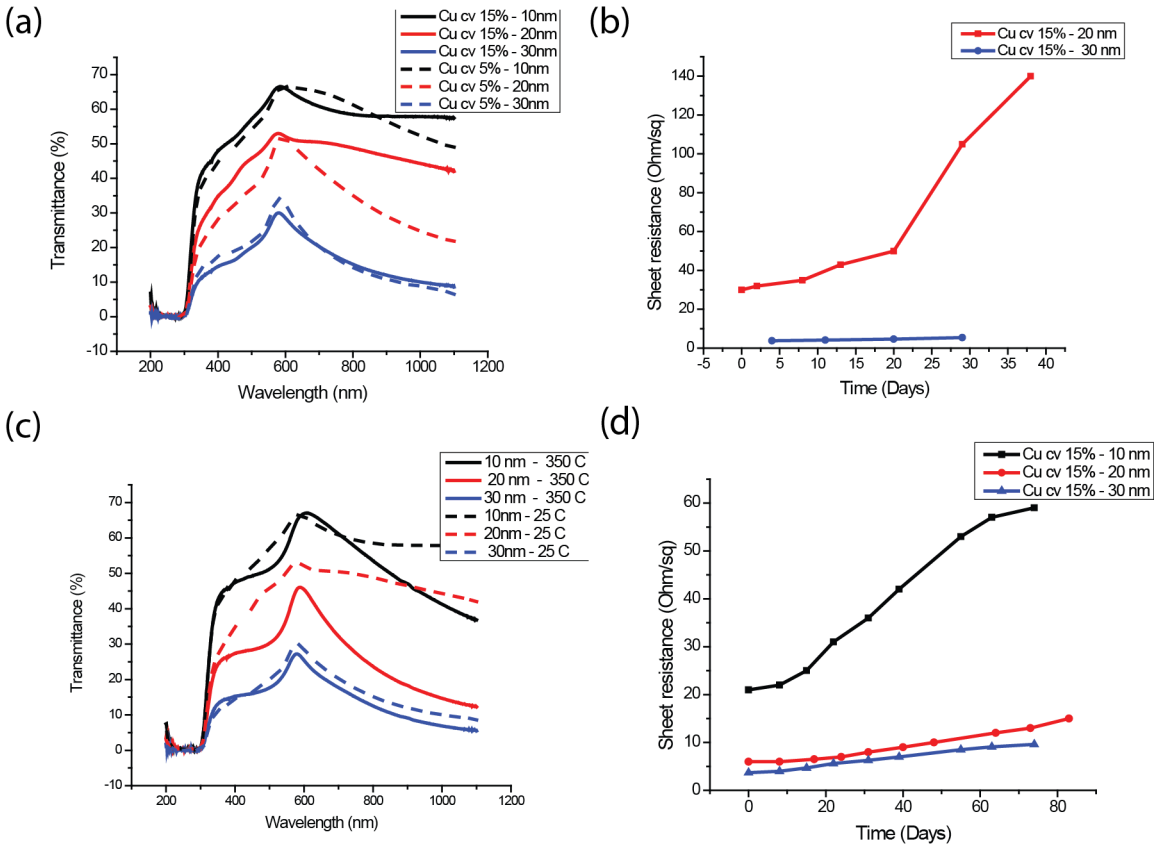

Figure 4.4: (a)Transmittance measurement comparing e-beam Cu cv 5% and Cu cv 15% films grown at room temperature, (b) Electrical stability measurement of the Cu cv 15% films grown at room temperature (25^0 C), (c) Transmittance measurement so Cu cv 15% films grown at 25^0 C and 350^0 C, (d) Electrical stability of the films Cu cv 15% films grown at high temperature (350^0 C).

perature (350^0 C) as shown in Figure 4.4(c). The films deposited at higher temperatures show lower transmittance than the films deposited at room temperature at higher wavelengths, but the transmittance at 550 nm remained approximately the same except in the case of the 20 nm film where the transmittance of the room temperature film is slightly higher. The electrical stability of the Cu cv 15% films grown at high temperature is shown in Figure 4.4(d). The sheet resistance of the films grown at high temperature is lower than the films grown at room temperature (Figure 4.4(b)). A higher deposition temperature has the effect of producing larger grains that reduce scattering at grain boundaries and therefore increase conductivity. A longevity study of the 20 nm Cu cv 15% e-beam film deposited at 350^0 C shows that e-beam films are stable at least up to 3 months. AFM images shown in Figure 4.5 indicate that over a three-month period the grain sizes remain the same in the height image and minimum change in phase contrast is observed. In contrast, significant changes were observed in Cu metal films as Cu oxide changes the phase contrast of the image (not shown).

In order to better understand why the transmittance of Cu covetic films is higher than Cu metal films we obtained ellipsometry data from the films on Si substrate to extract the index of refraction constants n and k. The starting conditions used a B-spline model of the film consisting of three layers: The Si substrate with known optical constants, intermixing layer (native SiO_2) and the Cu film. Known n and k values of Cu at a specific wavelength were also supplied as a starting point for the model. The thickness of the SiO_2 layer was fixed at 1.5 nm since it is known to be self-limiting, and thickness and optical constants fitted. The data for Cu cv 5%

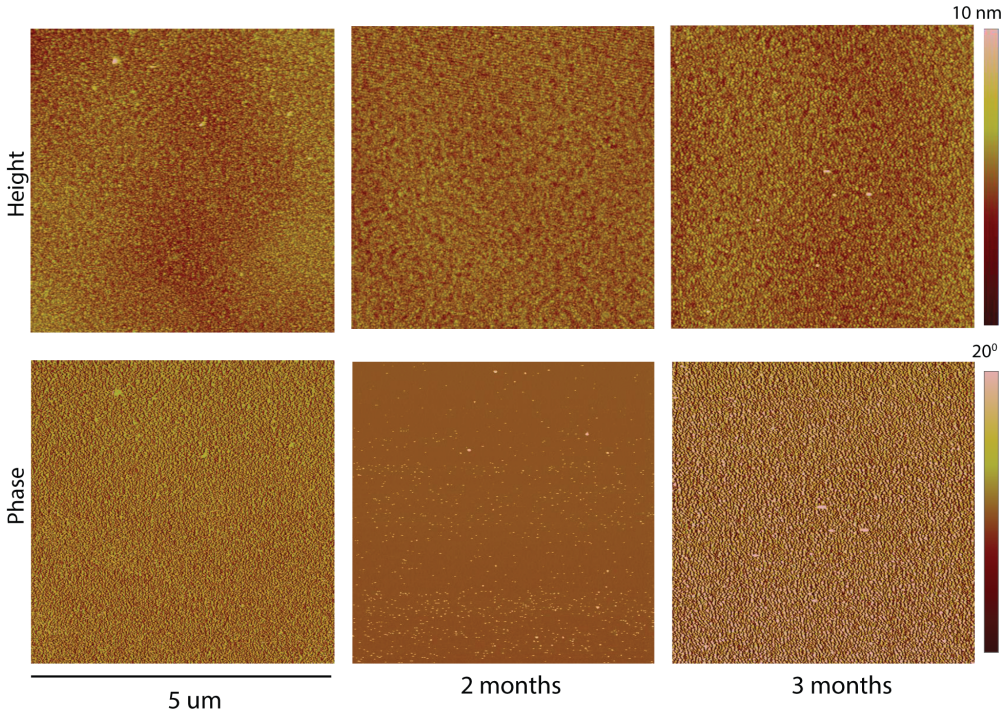

Figure 4.5: AFM height and phase of a Cu cv 15% film grown at 350^0C measured over a three month period shows very little change in the height and phase contrast, indicating a stable structure.

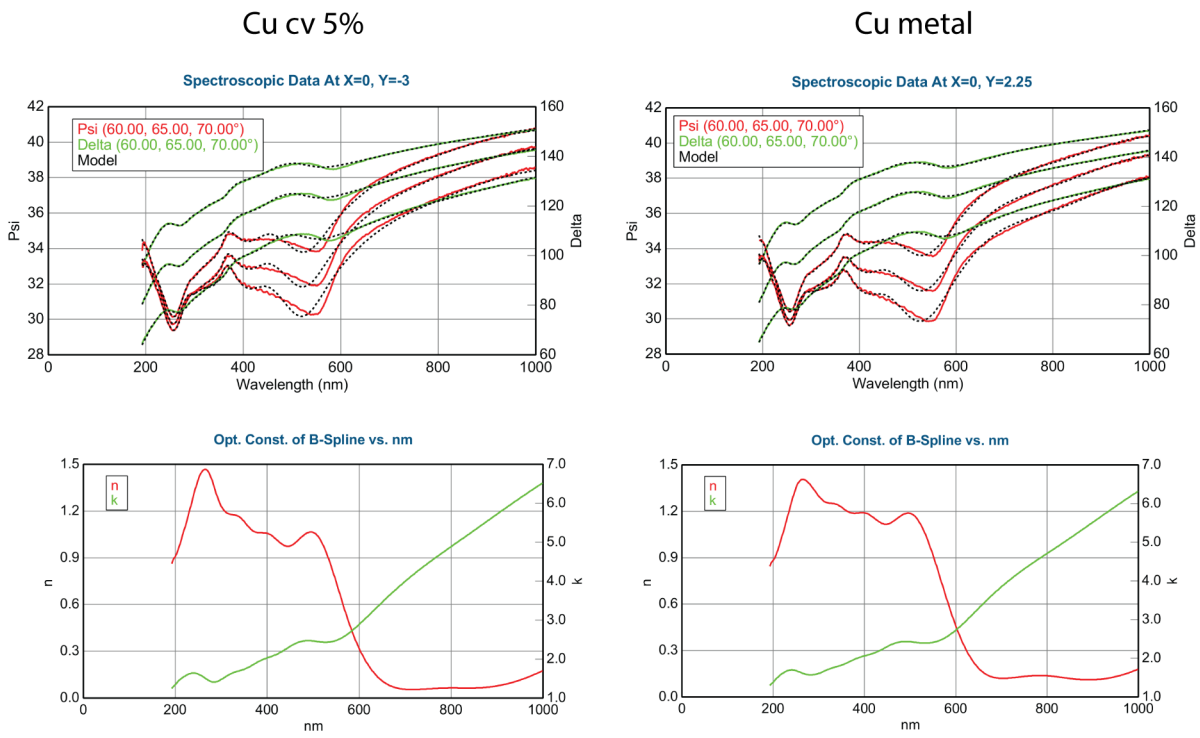

Figure 4.6: Ellipsometry of Cu cv 5% and Cu metal e-beam films on Si substrate using the same B-spline model and the corresponding optical constants.

and Cu metal e-beam films on Si substrate using this model with the corresponding optical constants n and k is shown in Figure 4.6. Our results agree with the known optical constant of Cu,(*83*) but subtle differences are observed between Cu cv 5% and Cu metal. A good visual fit of the model to the data is observed in the plots, but Cu metal fits better to the model than Cu covetic, as is evidenced by the MSE values of 3.264 and 3.423 respectively. We know that in ellipsometry a wide range of thickness give the same MSE value, and the optical constants will adjust to compensate. In this case we know the thickness of the films is $\approx$ 30 nm and the model fitted both thickness to be 28.74 nm and 28.41 nm respectively for the Cu cv 5% and Cu metal films. In order to get the most physical result, we indepen-

dently measured the thickness from using an N&K spectrometer, so we concluded that the MSE values measured do not just correlate with the optical properties, but are unique. This indicated that the difference observed between Cu metal and Cu covetic films is due to the structure of the film in general and the presence of C in particular.

4.2 Improvement in Ampacity

The ampacity, maximum allowed current, of the 20 nm Cu and Cu covetic films was estimated using Equation 4.2 derived by D'Amore et. al,(*84*) for transparent metal films.

$$I_L = \sqrt{\frac{2h(w+d_s)wd_s\sigma_s(T_s - T_e)}{1+\alpha_s(T_s - T_e)}} \tag{4.2}$$

where I_L is the film current-carrying limit, T_e is the environmental temperature surrounding the conductor, d_s, w, α_s and σ_s are the film's thickness and width, temperature coefficient of resistance and the electrical conductivity measured at T_e, respectively. The thermal limit is the maximum working temperature T_s, below which the film integrity is not compromised. The conductivities of a 20 nm Cu metal ($\sigma_{Cu} = 1.74 \times 1067$S/m) and Cu covetic ($\sigma_{covetic} = 1.77 \times 10^7$ S/m) films were obtained from the sheet resistance. The temperature coefficient of resistance of Cu is $\alpha_{Cu} = 3.94 \times 10^{-3}K^{-1}$.(*85*) α was determined for Cu covetic (Cu cv 3%) bulk sample using a Physical Property Measurement System (Quantum Design) with a temperature range from 1.5 K - 350 K. At room temperature $\alpha_{covetic} = 3.825 \times 10^{-3}K^{-1}$. The coefficient h in Eq. 4.2 depends on factors including the

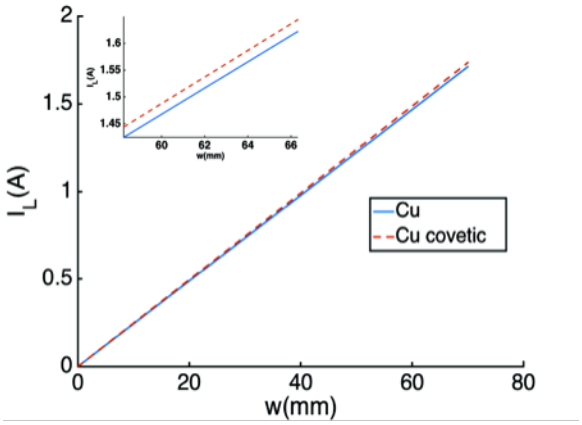

Figure 4.7: Current at thermal limit as a function of the sample width for 20 nm films.

thermal and dynamical properties of the fluid (air) surrounding the sample and the geometrical configuration and heat absorption coefficient of the material sample.(*84*) In the case of natural convection, typical values of h range from 5 to 25 W/m^2K. Figure 4.7 shows the current I_L of the two films on glass as a function of sample width assuming a value of $h = 10W/m^2K$, and $d = 20$ nm, $T_e = 200^0$ C, and $T_s = 150^0$ C. These data show that e-beam Cu cv 5% films have comparable or slightly higher ampacity than Cu metal films due to the presence of C in the film structure.

In order to obtain Cu covetic flms with higher C content we deposited films by pulsed laser deposition (PLD). PLD is a technique that can transfer atoms, molecules and larger particles to the film, so we wanted to investigate whether PLD could transfer more C to the films than was possible using e-beam deposition.

Chapter 5: Pulsed Laser Deposited Films

5.1 Fabrication

Our best Cu covetic film made by e-beam deposition exhibited 2 Ohm/sq at 28% transmittance, so in order to improve these optoelectrical properties we sought to introduce more carbon into the film using pulsed laser deposition (PLD). We were able to produce a 50 nm thick Cu cv 4% film with 0.13 Ohm/sq at 25.5% transmittance grown by PLD. PLD of copper, under similar conditions as described here, has been previously studied in great detail.(*86*) Laser light incident on a target in a vacuum chamber causes the temperature of the surface to increase. Ablation occurs when the temperature of the heated surface reaches the boiling point, since the vapor pressure is a function of temperature. When sufficient energy is absorbed in the target material, mechanical coupling, rather than surface absorption dominates. The boiling temperature is achieved for a critical value of fluence (energy per unit area), which is determined by the laser power, chamber pressure and target composition. As the fluence is increased above this critical value the density of the vapor increases and a plasma is produced. This causes cold mass fragments to accelerate towards the substrate, giving rise to ablation of the target material. The figure of merit that describes the interaction for a particular laser-target system is given by

Equation 5.1, the mechanical coupling coefficient, C_m.(*87*)

$$C_m = \frac{P_a}{I} = \frac{J}{W_L} \tag{5.1}$$

where P_a is the ablation pressure, I is the incident laser intensity, J is the total momentum imparted to the target and W_L is the laser energy. C_m usually ranges from 1-10 for endothermic surface absorbers, which includes all metals and many C-H materials in the UV-IR range.

In order to produce a transparent conducting film from the copper covetic bulk, the optimum photoablation parameters must be ascertained to ensure that the carbon structures are transferred from the target to the film. The substrate temperature and deposition time also influence the structure and properties of the film. Cu covetic is comprised of Cu and C, where each element has a different interaction with the laser beam and can give rise to preferential sputtering of one element over the other. In order to produce a homogenous film, the deposition parameters were altered and the resulting structure of the film analyzed. Spectroscopy techniques such as XRD, XPS, Raman, EDS and EELS as well as microscopy techniques such as AFM, KPFM, and TEM were used to characterize the PLD films. 4 point-probe, and UV-VIS spectroscopy were used to investigate the electrical, and optical properties, respectively, of the films. Table 5.1 presents the conditions used to grow the PLD films in this study. Just as in the case of the e-beam films, PLD films were grown on glass (or quarts and sapphire for the films grown at 500^0 C) and Si substrates placed side by side in the PLD chamber. Also, films of pure copper were grown by PLD for comparison.

Table 5.1: Deposition Conditions used for Cu cv 4% films prepared for this study.

Sample No.	Laser (W)	Chamber Pressure (mTorr)	Substrate Temp. (C)	Deposition Time (mins)	Film Thickness (nm)	C conc.* (at.%)/(wt.%)
1	1.88	100	150	15	15	no C
2	3.55	100	150	20	11	no C
3	3.3	100	350	64	20	no C
4	3.2	95	150	60	13	seg. C
5	2.3	100	150	60	30	2.94 (0.57)
6	2.4	98	150	60	10	2.62 (0.44)
7	2.6	97	500	60	21	5.30 (1.1)
8	2.0	97	500	120	50	19.14 (4.1)

* based on carbon and copper only, oxygen excluded from calculation

Films (1) and (2) grown at laser powers <2W and >3.5 W, respectively, show no C content as measured by XPS (not shown). At these laser powers Cu is preferentially sputtered from the target, and is soon oxidized to CuO and Cu_2O. Increasing the substrate temperature from 150^0 to 350^0 C, as demonstrated by films (2) and (3), respectively, did not help alter the film structure, but as expected a longer deposition time resulted in a thicker film. Reducing the laser power for film (4) enabled C to be transferred to the substrate, but the film produced was segregated into a Cu layer and a C layer, where C sputtered first then Cu. The sputtering rate of 10.2 nm/min, 5 nm/min, 2.7 nm/min was measured for Cu, SiO_2 and C, respectively. In order to obtain a homogeneous uniform film, the power was further reduced, to 2.5 ± 0.2 W, as shown in films (5) and (6). While homogeneous, these films were amorphous and exhibited high resistivity. Films (7) and (8) show that by increasing the substrate temperature to 500^0 C we were able to produce homogeneous crystalline film with uniform carbon content throughout the film thickness.

5.1.1 Structural Characterization

A Cu metal and Cu covetic film (6), were grown using the same conditions within 24 hours of each other. After deposition, the roughness of both samples was ≈ 1.5 nm, but differences between their structures can be clearly seen by inspecting the AFM images in Figure 5.1 taken 28 and 34 days after deposition respectively for the Cu metal and Cu covetic films. From the phase contrast it is evident that the Cu covetic film is homogeneous, while the Cu metal film shows regions of high

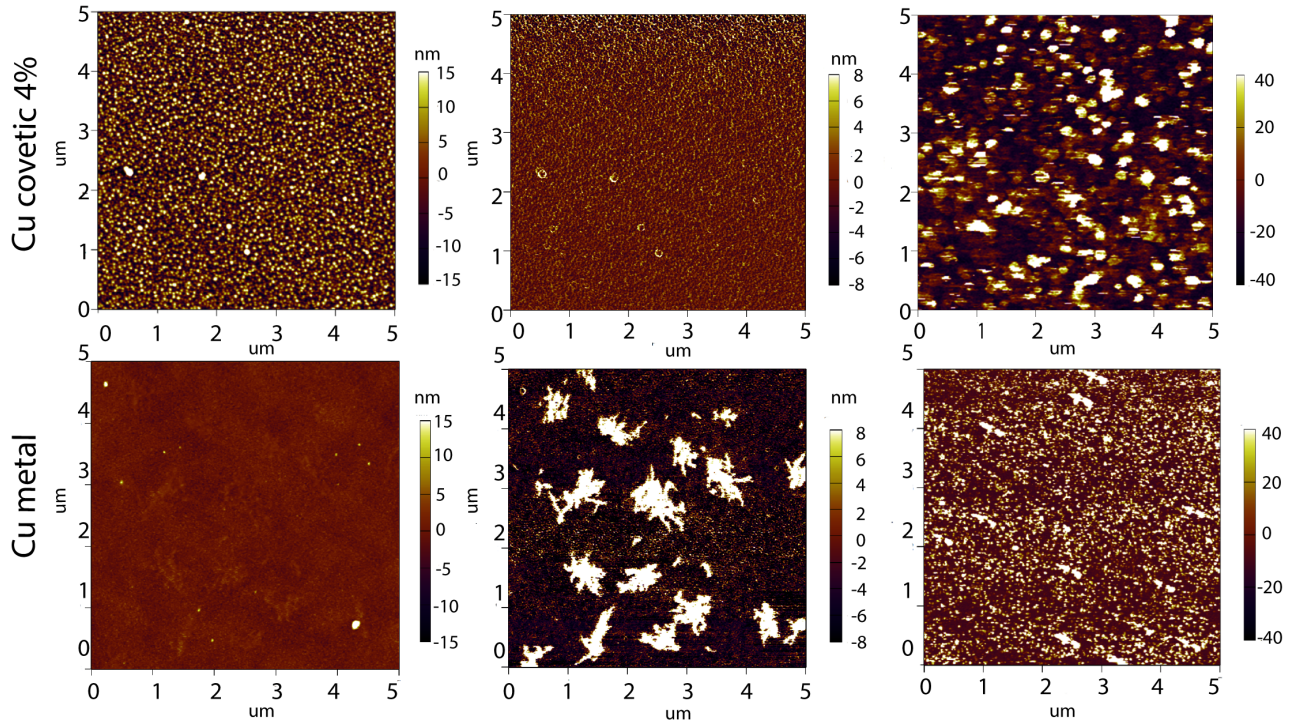

Figure 5.1: AFM images comparing the grain structure in the height image (left column) the phase contrast (center column) and KPFM images (right column) mapping the surface potential of a Cu covetic and Cu metal sample

contrast where the film has oxidized. No such oxidation is evident in the covetic film over the same time period. Kelvin Probe Force Microscopy (KPFM) was used to measure the surface potential of the films for comparison. Dual pass scans was used to correct the topographic variation within the scanned area. For a given raster, the first scan determines the height and the second scan with fly-height ≈10 nm, probes the surface potential. The Cu cv 4% film shows regions of low contrast compared to the Cu metal film. Since Pt and C have similar work functions, the regions with C have low contrast as can be observed in the Cu cv 4% image. XRD spectra from films (2)-(7) are shown in Figure 5.2(a). Films (2), (3) and (4) show mostly Cu_2O, while films (5) and (6) are amorphous as no clear peak is observed in the spectra from these films. In contrast, film (7) shows strong Bragg peaks at 2θ=44 and 52 degrees corresponding to Cu (111) and (200) reflections, respectively. XPS from this same film in Figure 5.2(b) measured C content of 1.1 wt.% (5.30 at.%) in the film region. The inset of Figure 5.2(b) shows the C 1s peak from the film region indicating Cu-C bond at ≈ 283 eV, sp^2 (C-C) and sp^3 (C=C) bonds overlapping at their conventional binding energy (0.8 eV apart) and a shoulder at 286 eV corresponding to C-O. The peak for Cu-C bonding at 283 eV is relatively strong and suggests that copper covetic has a different structure from a simple copper carbon composite.

A cross section TEM lamella (shown in Figure 5.3(a)) of the Cu cv 4% film (7) was prepared using a FEI Helios 650 FIB and milled using gallium (Ga^+) ions to electron transparency. The TEM image of the ≈ 20 nm Cu cv 4% film deposited on a Si (100) substrate and covered with a Pt protection layer is shown in Figure 5.3(b), and exhibits a continuous surface with RMS roughness of 4 nm in agreement

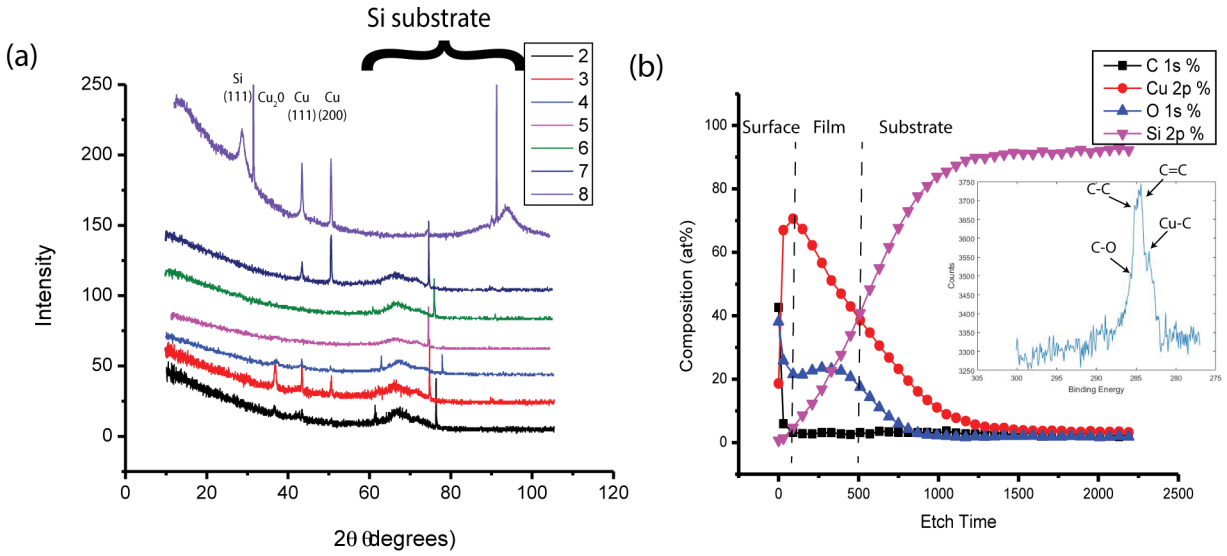

Figure 5.2: (a) X-ray diffraction of the Cu cv 4% films grown via PLD described in table 3, (b) XPS of film (7) showing 0.55 wt.% (2.87 at.%) C concentration in the film region, with the inset showing the C 1s peak.

with the value measured by AFM. Crystalline grains can be observed from the HRTEM image (Figure 5.3(c)) and electron nanodiffraction from the film shows spots associated with the Cu and C (Figure 5.3(d)). There are spots with d-spacing of 0.250 nm and 0.257 that correspond to the (002) and $(\bar{1}\bar{1}1)$ of CuO as well as one set of spots with d of 0.348 nm that correspond to (002) interplanar distance of graphite.

EELS from the Cu cv 4% film (7) was acquired in scanning TEM mode (STEM) using a JEOL high angle annular dark field (HAADF) detector. Figure 5.4(a) shows a HAADF image consisting of the substrate with dark and Pt with bright contrast. The region analyzed lies between these two layers and includes the film as well as thin areas of the substrate and Pt layer and is demarcated with the green box.

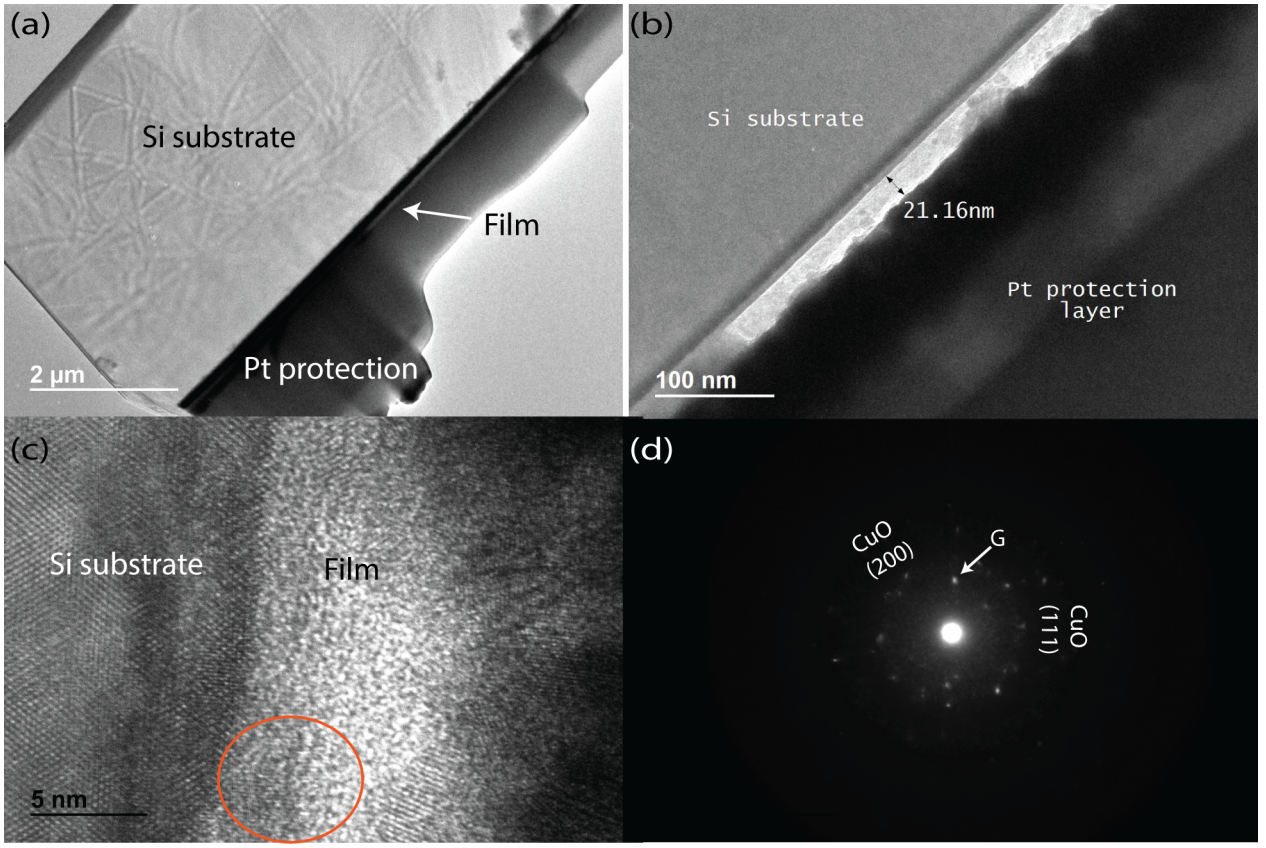

Figure 5.3: (a) Low resolution image of a TEM cross section lamella made using FIB, (b) TEM bright field image of the Cu cv 4% PLD film (7) measuring 21.16 nm on Si (100) with Pt protection layer, (c) HRTEM of film and substrate, (d) nanodiffraction from film region.

A higher resolution image of this region is shown in the HAADF image in Figure 5.4(b). The C-K edge spectrum image acquired using a spot size of 1.5 nm, dwell time of 0.05 sec and dispersion of 0.3 eV/channel is shown in (Figure 5.4(c)). At each pixel in the image a spectrum is acquired. The total spectrum of the film layer indicated in the red rectangle is shown in Figure 5.4(d), where the background signal has been subtracted to reveal the intensity corresponding to the C K-edge. This signal is weak due in part to the short dwell time used in order to minimize contamination during data acquisition and also because of the low carbon content in the film. Nevertheless, it shows the presence of C in this region. Figure 5.4(e) is a line profile of the C content across the region and shows a band in the map of the C-K edge (Figure 5.4(f)) clearly indicating the presence of C within the film layer, which is neither present in the substrate or Pt protection layer. Thus, carbon in the Cu covetic target can be transferred to the film by PLD within a narrow range of growth parameters.

We were able to use BSS to decompose the EELS spectra of Film 7 into three components that could be easily identified as shown in Figure 5.5: the background where the intensity distribution is quite uniform, C contamination that is present everywhere in the scanned region, and carbon that is found in the film region of the sample. C in the film region has a rise at $\approx$ 284 eV where the carbon K-edge is located. This MVA of the EELS spectrum image not only reproduces the result obtained from the background subtraction in Figure 5.4(d), but also gives more information about the fine structure of the C K-edge. There is some sp^2 character to the edge as evidenced by the peak at 285 eV, indicating transitions from the 1s

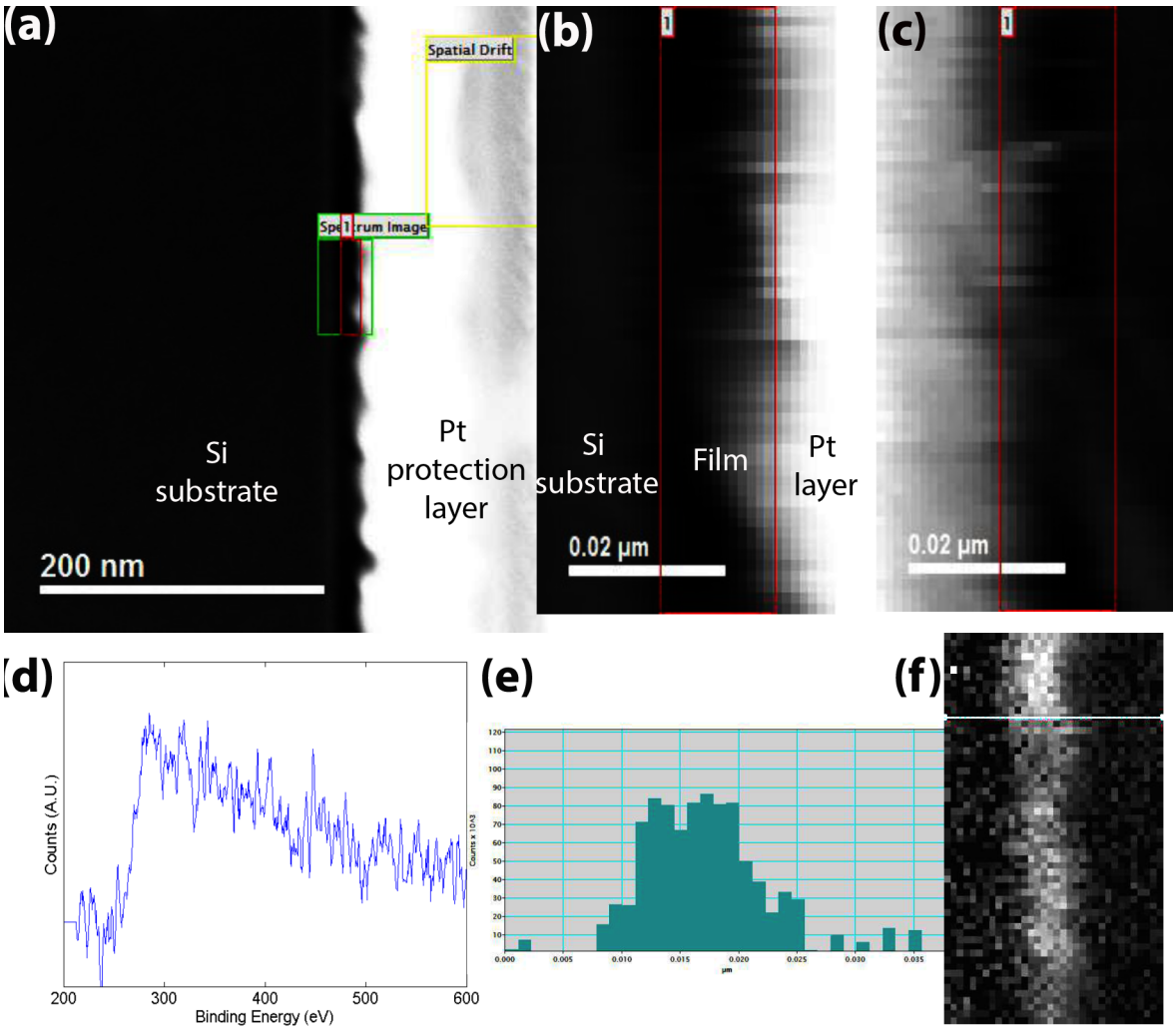

Figure 5.4: (a) HAADF survey image showing target region for EELS spectrum imaging in green and region for spectra sum in red, (b) Magnified HAADF image of target region, (c) spectrum image of the target region in the energy range of the C K-edge, (d) integrated spectra from region highlighted in red after background subtraction, (e) Line profile across the scanned region, (f) C K-edge distribution in scanned region.

occupied state to the π^* unoccupied states, but the dominant feature is the peak at 290 eV, corresponding to both sp^2 and sp^3 C. In Film 8 (Figure 5.6) we deposited for twice as long as film (7) to produce a 50 nm film as shown in Figure 5.6(a). Diffraction from the film region shows spot corresponding to Sapphire (111) and (110) as well as Cu (111) (Figure 5.6(b)). EELS spectra from the film region after background subtraction shows a profile of the C K-edge that is quite similar to that obtained from film (7), but with π^* more dominant, indicating more sp^2 C.

Cu covetic PLD films made from nominally 4% target show uniform integration of carbon in these film, with some modulation, but the inclusions observed in bulk samples are not present in these films. These films show up to 19.14 at.% (4.1 $\pm$ 0.6 wt.%) C, which indicate that under the right conditions PLD can transfer the same concentration of C from the bulk to the films. We observe evidence of sp^2 carbon in PLD Cu covetic films and a peak in the C K-edge in EELS indicative of transitions from 1s to π^* anti-bonding unoccupied state similar to that observed in bulk samples, suggesting that the C transfered is graphitic in nature.

5.1.2 Electrical and Optical Properties of PLD Films

The optical transmittance of the Cu cv 4% PLD films with C present in the structure in Figure 5.7(a) exhibits higher transmittance over a larger range of wavelengths compared to the Cu cv 5% and Cu cv 15% films grown by e-beam deposition. Films 10 nm -30 nm thick also lack the characteristic peak of Cu at 580 nm and instead show a flatter transmittance curve over the range of wavelengths tested. No-

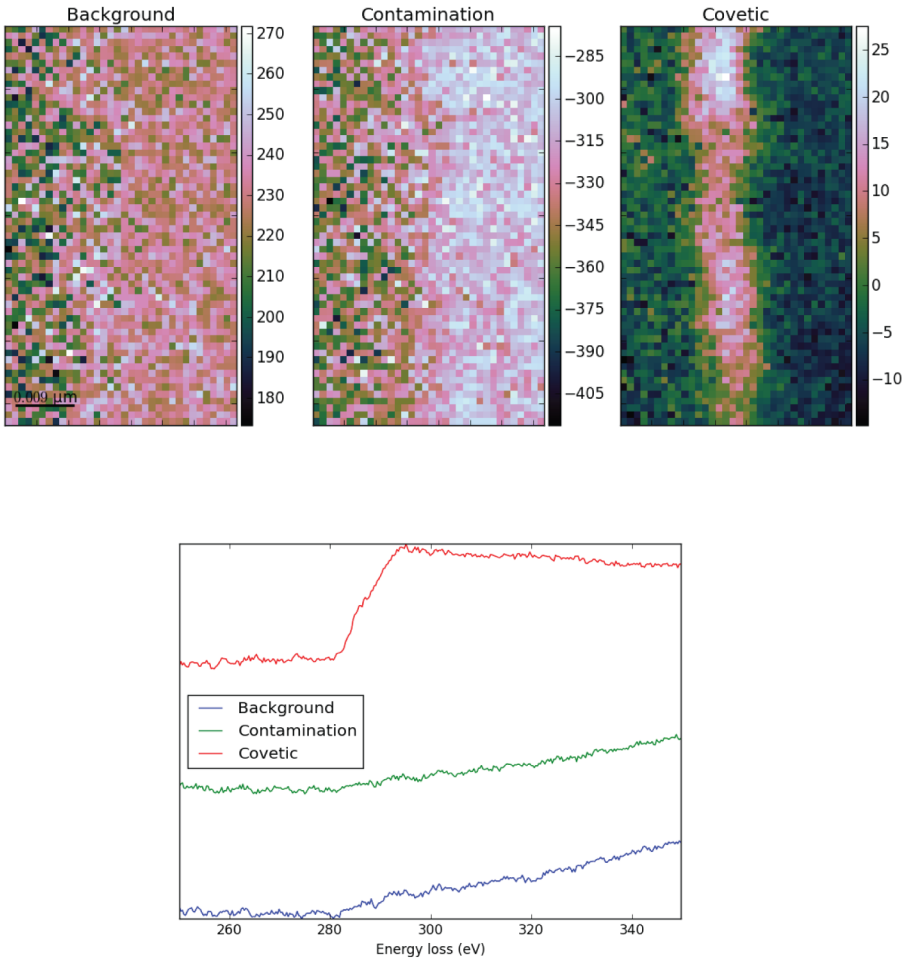

Figure 5.5: Decomposition of the Spectrum image of Film 7 using Blind Source Separation, shows three clear regions in the navigation and signal spaces: background, C contamination and C from the covetic film region.

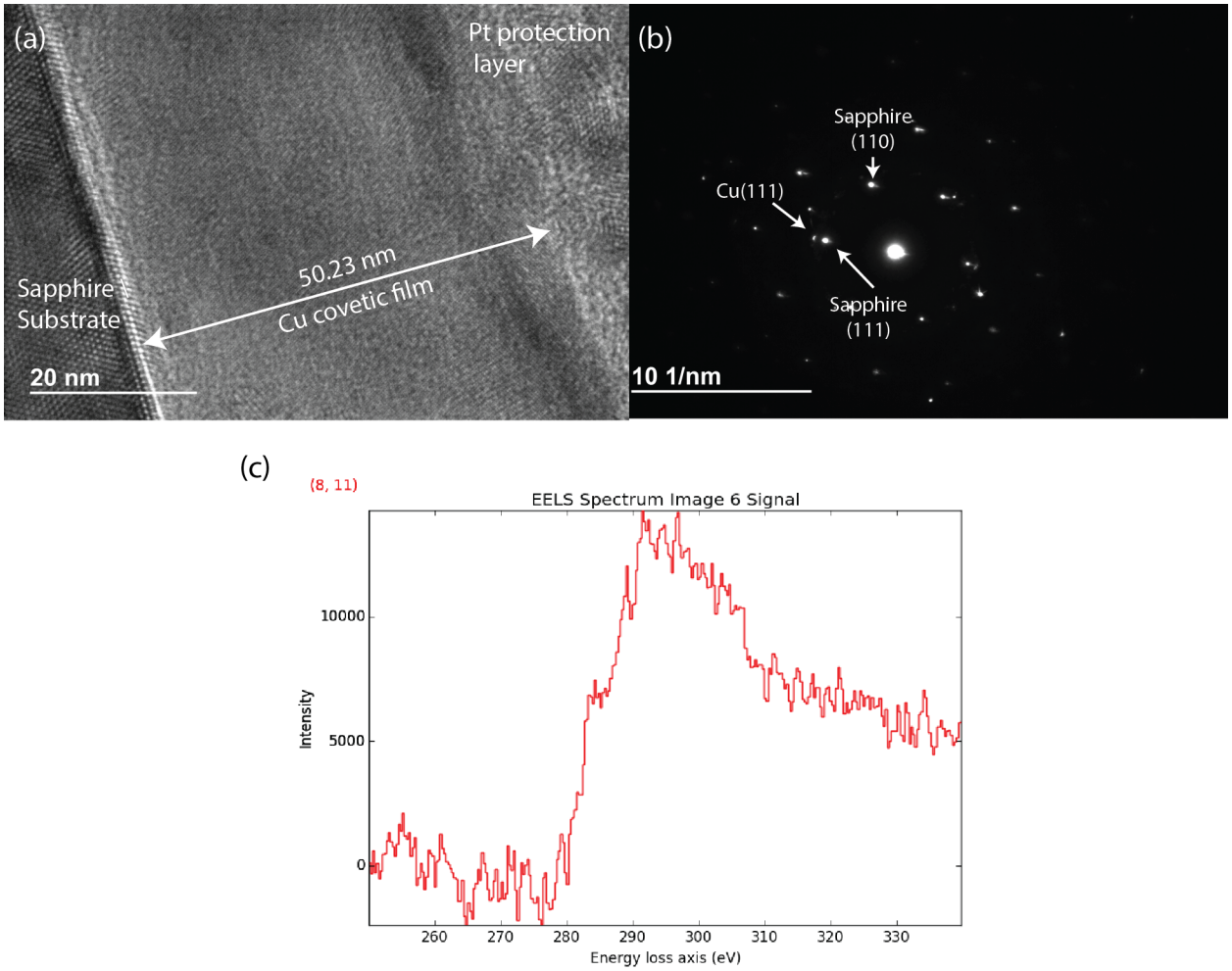

Figure 5.6: (a) TEM bright field image of a cross section lamella of the Cu cv 4% PLD film (8) made using FIB measuring 50.23 nm (b) Diffraction from film region including some of the substrate, (c) EELS spectrum from the film after background subtraction.

tably, the 20 and 30 nm films, seem to be more transparent than the 10 nm film, but the 20 nm and 30 nm also have higher C content which could increase their transmittance. This thickness difference could also be due to the location from which the TEM lamella was taken, from which the thickness is then measured. Given that PLD is known for producing a thickness gradient away from the center of the plume, site selection is of critical importance in determining an accurate measurement of the thickness. Film (8) at 50 nm thick shows a noticeably lower transmittance than the thinner films fabricated by PLD, and regains the profile of the e-beam films with characteristic peak of Cu at 580 nm. However, Film (8) is conducting, exhibiting sheet resistance of 0.13 Ohm/sq, two orders of magnitude lower than all e-beam films. The resistance increases with time as shown in Figure 5.7 (b), but not as high a rate as films fabricated by e-beam deposition. Notably, film (8) at 50 nm thick has a slightly higher transmittance than the 30 nm thick e-beam film shown in Figure 4.3(b). This combined with the significantly lower electrical resistance of the former results in a high figure of merit as a transparent conductor (Figure 5.7(c)).

We compared the optical constants of Cu covetic films made by PLD and e-beam deposition by using the same model detailed previously: Si substrate with known optical constants, intermixing layer (native SiO_2) and a B-spline layer representing the Cu covetic film. The spectroscopic data and fitted optical constants for PLF film (8) are shown in Figure 5.8. We observe that the fit of the model to the data is not as good as pure Cu deposited by e-beam (Figure 4.6) as shown in 5.8(a) which is corroborated by the significantly larger MSE value of 12.954. A clear difference is also seen the the optical constant of the film vs wavelength of the PLD film (Figure

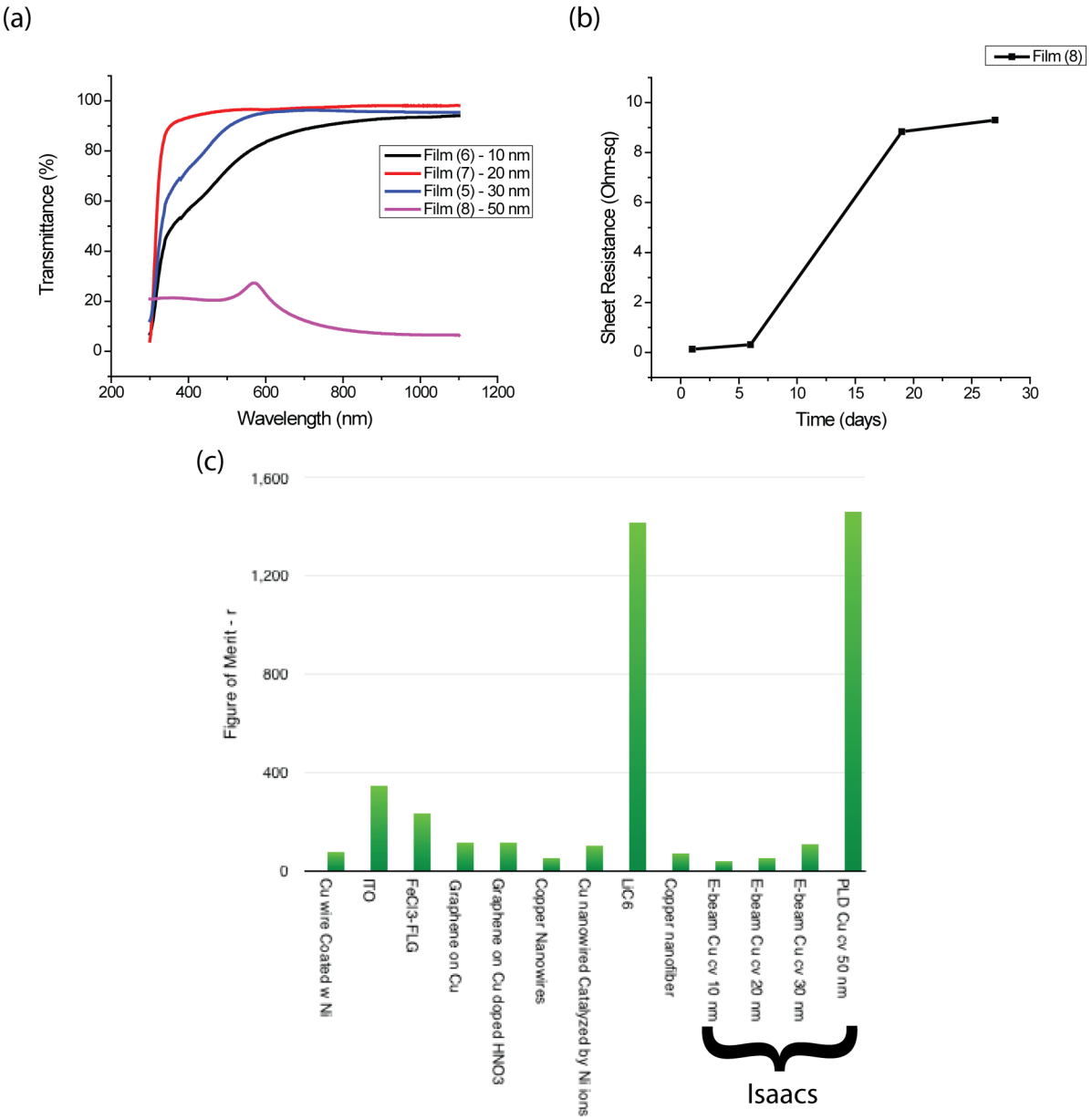

Figure 5.7: (a) Transmittance of Cu cv 4% PLD films, (b) Stability measurement of Cu cv 4% - Film 8, (c) Figure of Merit comparing Cu covetic films with various materials.(*36*),(*37*),(*3*),(*4*),(*47*),(*88*),(*78*)

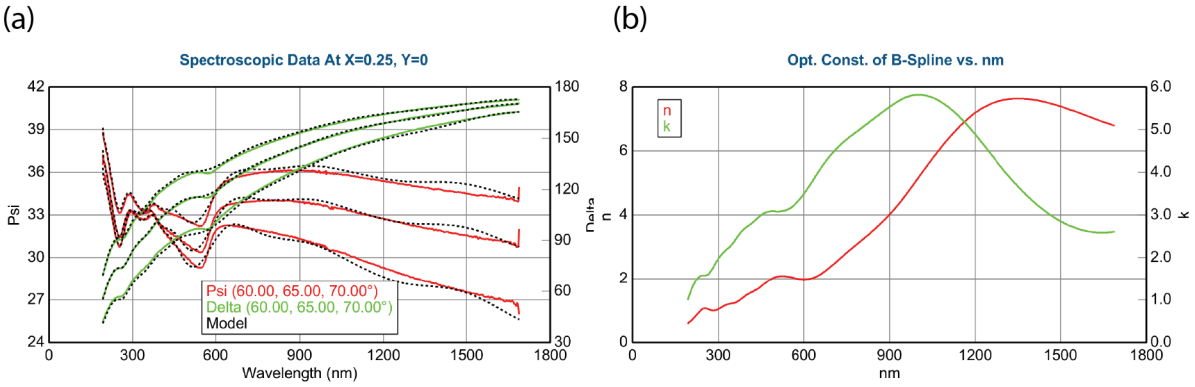

Figure 5.8: (a) Spectroscopic data of Cu coveitc film (8) deposited by PLD, (b) derived optical constant from the data in (a)

5.8(b)) and the Cu cv 5% e-beam film (Figure 4.6). This suggests that an increase carbon concentration results in different optical properties in Cu covetic films.

Chapter 6: Conclusion

6.1 Summary

We have introduced copper covetic, a material that incorporates nanoscale carbon into the metallic structure of copper. Bulk Cu covetic has a number of distinguishing features from pure Cu. The incorporation of C gives rise to modulation ≈ 1.6 nm and expansion of the Cu lattice as observed in TEM. Electron diffraction from these regions shows a unique pattern, with Cu and satellite spots in the area of this modulation, which corresponds to regions showing high carbon content as well as new reflections where the lattice constant has increased. Other regions of the bulk covetic samples show inclusions that contained high carbon and oxygen and which showed a different diffraction pattern that might be explained by the replacing two (111) planes of the copper lattice by a graphene plane but more detailed investigation of this structure is necessary. XPS shows a C 1s peak within the bulk which is comprised of sp^2 and sp^3 bonding. XPS depth profiling determines up to 3.5 wt.% (16 at.%) of C in Cu covetics. ToF-SIMS corroborates this finding by showing mass spectra corresponding to C^{12} throughout the bulk, well below the surface. EELS is able to detect C K-edge with graphene-like structure in bulk Cu covetics. We have used the Raman spectra of Cu covetic to model a likely structure

of Cu covetic based on the result obtained from phonon density of states. Electrical measurements of bulk Cu covetic drawn into wires indicate that C conductivity first decreases and then increases with C content.

Deposition of Cu covetic material using e-beam deposition and PLD into films on transparent substrates gives rise to a transparent and conducting film. Covetic films of comparable thickness have greater transparency, lower electrical resistivity, and greater stability when compared with pure copper films of the same thickness grown under the same conditions. E-beam copper covetic films approximately 30 nm thick exhibit the best combination of electrical stability and transparency and show promise as a transparent conductive layer for optoelectronic devices. We have also demonstrated that PLD films have higher C content in the film which gives rise to increased transparency. Additionally, PLD films deposited under the right conditions show improved optoelectical properties compared to Cu metal and e-beam deposited Cu covetic films. This work is a step forward in the development of a transparent metal conductor, which takes advantage of the low cost, high conductivity of copper, as well as nanocarbon species incorporated in the metal lattice.

Though the study of covetics is in its infancy, based on the results shown in this thesis we believe that Cu covetics are ordered alloys. They are not alloys in the traditional sense where there is a substitution of one atom for another as is the case in the Cu-Au alloy where Cu is substituted for Au atoms. Neither is it a compound like NaCl or SiC. We have defined a unit cell for Cu coveitcs in the supercell structure proposed in Chapter 3.1, which produces a diffraction pattern that is similar to what we observe in the inclusions present in bulk samples. Though

not all defined unit cells are alloys, as in the case of the combined GaAs-AlAs super lattices (a two phase material), the inclusions we observe are a single phase. Our goal is to increase the size of these inclusions until they are interconnected and form a continuous network throughout the bulk. This uniformity in the microstructure could lead to a significant improvement in the bulk properties measured. In this case, Cu covetics could have applications as an electrical conductor, given the promising results shown in this study.

6.2 Future Work

Future investigations of Cu covetic bulk samples involve improving the homogeneity of bulk materials. Samples used in this work were prepared in a foundry designed for large-scale production. These samples were found to be inhomogeneous, making site selection for characterization critical. Small scale processing of bulk material would aid in fine-tuning the conditions that lead to carbon nanostructures throughout the material, and would likely result in uniform distribution of the measured properties.

We propose further study of the inclusions observed in the bulk samples using Raman spectroscopy. Cu coveitcs probed with excitation lasers with wavelengths: 532 and 633 nm do not show D and G peaks, and suffer from fluorescence due to the presence of Cu, but a 784 nm laser may excite different modes and give new insights.

Fundamental understanding of the structure of Cu covetic materials at atomic

length scales have begun with this work using XRD. We were able to detect changes in the lattice constant of Cu covetic as well as texturing in the <111> direction. However synchrotron x-ray sources provide eight orders of magnitude higher flux than lab x-ray sources, which would provide higher angular and energy resolution. Using synchrotron-based x-ray sources we will better understand where C is located in the Cu lattice, as these sources can measure the structure directly on length-scales from 0.1 - 5000 nm.

Bulk samples drawn into wires have received cursory study in this thesis, but large scale testing of the ampacity and conductivity of wires that could be used in commercial applications would be advantageous. Whether the properties observed in lab scale testing will translate into real work application is unknown, so further testing is required. Very rarely is a material performing a single function, as such Cu covetic will have to meet many regulatory requirements before deployment. Therefore, further investigation into the mechanical properties would also be quite useful. Wires are usually under high tension and expected to perform over a range of temperatures. Studies measuring the electrical conductivity as a function of temperature as well as the resistance to oxidation and corrosion of Cu covetic wires would give indications as to its suitability for various commercial applications.

Cu covetic thin films have potential applications in display and solar cells, but integration in a device structure has not been pursued in this work. Embedding a Cu covetic thin films as a transparent electrode in such a structure could help to fine tune the thin film parameters: thickness, optical and electrical requirements that would make a successful transparent electrode. We fabricated films with uniform

C distribution in the bulk using PLD with a visible wavelength laser, but we do not observe the inclusions present in bulk samples. It may be instructive to use a UV wavelength laser to elucidate whether these structures can be transfered and how they impact the properties measured. Though PLD was a useful technique for fundamental study of this new material, Cu covetic, it is not a suitable technique for commercial scale production. Investigating other techniques that will transfer C from the bulk into a thin film reliably, such as sputtering, with a similar structure to the bulk would be necessary for commercial development.

Bibliography

1. M. Lin *et al.*, *Proceedings of the IEEE 2003 Custom Integrated Circuits Conference, 2003.* 533–536, ISSN: 08865930 (2003).
2. A. Raychowdhury, K. Roy, *IEEE Transactions on Computer-Aided Design of Integrated Circuits and Systems* **25**, 58–65, ISSN: 02780070 (2006).
3. I. Khrapach *et al.*, *Advanced Materials* **24**, 2844–2849 (2012).
4. S. Bae *et al.*, *Nature Nanotechnology* **5**, 574–8, ISSN: 1748-3395 (2010).
5. C. Subramaniam *et al.*, *Nature communications* **4**, 2202, ISSN: 2041-1723 (2013).
6. N. Behabtu *et al.*, *Science* **339**, 182–186 (2013).
7. P. Jarosz *et al.*, *Nanoscale* **3**, 4542, ISSN: 2040-3364 (2011).
8. H. P. Kumar, M. A. Xavior, *Procedia Engineering* **97**, 1033–1040, ISSN: 18777058 (2014).
9. K. S. Novoselov *et al.*, *Science* **306**, 666–669, ISSN: 1095-9203 (2004).
10. K. S. Novoselov *et al.*, *Proceedings of the National Academy of Sciences of the United States of America* **102**, 10451–10453, ISSN: 0027-8424 (2005).
11. A. Geim, K. Novoselov, *Nature Materials* **6**, 183–191, ISSN: 1476-1122 (2007).
12. A. K. Geim, *Science* **324**, 1530–4, ISSN: 1095-9203 (2009).
13. X. Li *et al.*, *Science* **324**, 1312–4, ISSN: 1095-9203 (2009).
14. Y. Kim *et al.*, *Nature Communications* **4**, 2114, ISSN: 2041-1723 (2013).
15. J. Tian *et al.*, *Nano Letters* **12**, 3893–9, ISSN: 1530-6992 (2012).
16. Z. R. Robinson, P. Tyagi, T. R. Mowll, C. a. Ventrice, J. B. Hannon, *Physical Review B* **86**, 235413, ISSN: 1098-0121 (2012).
17. S. R. Bakshi, D Lahiri, a Agarwal, *International Materials Reviews* **55**, 41–64, ISSN: 09506608 (2010).
18. J. Wang, G. Fan, Z. Chen, *Scripta Materialia* **66**, 594–597 (2012).
19. C. Gong *et al.*, *ACS Nano* **6**, 5381–5387, ISSN: 19360851 (2012).
20. M. O. Reilly *et al.*, *Applied Surface Science* **91**, 152–156 (1995).
21. M. Dresselhaus, G. Dresselhaus, R. Saito, A. Jorio, *Physics Reports* **409**, 47–99, ISSN: 03701573 (2005).
22. D. S. Hecht, L. Hu, G. Irvin, *Advanced Materials* **23**, 1482–513, ISSN: 1521-4095 (2011).

23. C. Mattevi, H. Kim, M. Chhowalla, *Journal of Materials Chemistry* **21**, 3324, ISSN: 0959-9428 (2011).

24. S. Amini, J. Garay, G. Liu, A. a. Balandin, R. Abbaschian, *Journal of Applied Physics* **108**, ISSN: 00218979, DOI: 10.1063/1.3498815, arXiv: 1011.4081 (2010).

25. S. B. Sinnott *et al.*, *Chemical Physics Letters* **315**, 25–30, ISSN: 0009-2614 (1999).

26. C. Gong *et al.*, *Journal of Applied Physics* **108**, 123711, ISSN: 00218979 (2010).

27. T. Ueno *et al.*, *Synthetic Metals* **159**, 2170–2172, ISSN: 03796779 (2009).

28. M. Zhi, C. Xiang, J. Li, M. Li, N. Wu, *Nanoscale* **5**, 72–88, ISSN: 2040-3372 (2013).

29. W. X. Chen *et al.*, *Carbon* **41**, 215–222, ISSN: 00086223 (2003).

30. H. Dai, E. W. Wong, Y. Z. Lu, S. Fan, C. M. Lieber, *Nature* **375**, 769–772, ISSN: 0028-0836 (1995).

31. G. López, E. Mittemeijer, *Scripta Materialia* **51**, 1–5, ISSN: 13596462 (2004).

32. Y. L. Yang *et al.*, *Materials Letters* **62**, 47–50, ISSN: 0167577X (2008).

33. S. Dorfman, D. Fuks, *Composites Part A* **27A**, 697–701 (1996).

34. S. Dorfman, D. Fuks, M. Suery, *Journal of Materials Science* **34**, 77–81 (1999).

35. J. V. Shugart, R. C. Scherer, *Metal-Carbon Compositions US 2012/0009110 A1*, 2012.

36. A. R. Rathmell, S. M. Bergin, Y.-L. Hua, Z.-Y. Li, B. J. Wiley, *Advanced Materials* **22**, 3558–63, ISSN: 1521-4095 (2010).

37. A. R. Rathmell *et al.*, *Synthesis of Oxidation-Resistant Cupronickel Nanowires for Transparent Conducting Nanowire Networks*, 2012, http://pubs.acs.org/doi/pdf/10.1021/nl301168r.

38. P.-C. Hsu *et al.*, *ACS Nano* **6**, 5150–5156 (2012).

39. L. Hu, H. Wu, Y. Cui, *MRS Bulletin* **36**, 760–765, ISSN: 0883-7694 (2011).

40. H. Wu *et al.*, *Nature Nanotechnology* **8**, 421–425, ISSN: 1748-3395 (2013).

41. Y. Zhou, L. Hu, G. Gruner, *Applied Physics Letters* **88**, 123109, ISSN: 00036951 (2006).

42. J.-Y. Lee, S. T. Connor, Y. Cui, P. Peumans, *Nano Letters* **8**, 689–92, ISSN: 1530-6984 (2008).

43. J. H. Lee, P. Lee, D. Lee, S. S. Lee, S. H. Ko, *Crystal Growth & Design* **12**, 5598–5605, ISSN: 1528-7483 (2012).

44. S. De *et al.*, *ACS Nano* **3**, 1767–1774 (2009).

45. A. Sánchez-Iglesias *et al.*, *Nano Letters* **12**, 6066–70, ISSN: 1530-6992 (2012).

46. P. E. Lyons *et al.*, *The Journal of Physical Chemistry Letters* **2**, 3058–3062 (2011).

47. H. Guo *et al.*, *Scientific Reports* **3**, 2323, ISSN: 2045-2322 (2013).

48. H. Wu *et al.*, *Nano Letters* **10**, 4242–8, ISSN: 1530-6992 (2010).

49. J. Shugart, R. Scherer, *Copper Cabon Composition US Patent No: 2013/0062572 A2*, 2013.

50. J. E. Cornett, O. Rabin, *Solid-State Electronics* **101**, 106–115, ISSN: 00381101 (2014).

51. Burnham, Colton, *Scanning Tunneling Microscopy*, ed. by D. Bonnell (VCH Publishers, New York, 1994).

52. J. F. Moulder, W. F. Stickle, P. E. Sobol, K. D. Bomben, *Handbook of X-ray Photoelectron Spectroscopy* (Physical Eletronics Inc., 1992), ISBN: 0-964812-1-X.

53. L. M. Malard, M. a. Pimenta, G. Dresselhaus, M. S. Dresselhaus, *Physics Reports* **473**, 51–87, ISSN: 03701573 (2009).

54. J. Woollam, *Ellipsometer Manual M-2000 Spectroscopic*.

55. J. Woollam, *CompleteEASE ™ Data Analysis Manual*, 2008.

56. J. A. Rodríguez-Manzo *et al.*, *Nature Nanotechnology* **2**, 307–11, ISSN: 1748-3395 (2007).

57. A. V. Krasheninnikov, F Banhart, *Nature Materials* **6**, 723–33, ISSN: 1476-1122 (2007).

58. L Nistor, V Ralchenko, I Vlasov, *Physica Status Solidi (a)* **214**, 207–214, ISSN: 0031-8965 (2001).

59. R. R. Schlittler *et al.*, *Science* **292**, 1136–1139, ISSN: 00368075 (2001).

60. F. de la Pena *et al.*, *Ultramicroscopy* **111**, 169–176, ISSN: 03043991 (2011).

61. F. de la Pena *et al.*, DOI: `10.5281/zenodo.28025`, `http://zenodo.org/record/28025` (2015).

62. M. C. Payne, M. P. Teter, D. C. Allan, T. A. Arias, J. D. Joannopoulos, *Reviews of Modern Physics* **64**, 1045–1097, ISSN: 00346861 (1992).

63. J. P. Perdew, K. Burke, M. Ernzerhof, *Physical Review Letters* **77**, 3865–3868, ISSN: 0031-9007 (1996).

64. P. E. Blöchl, *Physical Review B* **50**, 17953–17979, ISSN: 01631829 (1994).

65. G. Kresse, D. Joubert, *Physical Review B* **59**, 1758–1775, ISSN: 1098-0121 (1999).

66. G. Kresse, J. Hafner, *Physical Review B* **48**, 13115–13118, ISSN: 01631829 (1993).

67. G. Kresse, J. Furthmüller, *Physical Review B* **54**, 11169–11186, ISSN: 0163-1829 (1996).

68. D. J. Chadi, M. L. Cohen, *Physical Review B* **8**, 5747–5753, ISSN: 01631829 (1973).

69. H. Jónsson, G. Mills, K. Jacobsen, *Classical and quantum dynamics in condensed phase simulations*, ed. by D. F. C. B. U. Bruce J Berne (Columbia University), Giovanni Ciccotti (Universita Roma "La Sapienza") (ed. 1, 1998), pp. 385–404, ISBN: 978-981-02-3498-0.

70. P. Maragakis, S. A. Andreev, Y. Brumer, D. R. Reichman, E. Kaxiras, *Journal of Chemical Physics* **117**, 4651–4658, ISSN: 00219606 (2002).

71. O. Sharia, M. M. Kuklja, *Journal of Physical Chemistry C* **116**, 11077–11081, ISSN: 19327447 (2012).

72. L. G. Salamanca-Riba *et al.*, *Advanced Functional Materials* **25**, 4768–4777, ISSN: 1616301X (2015).

73. A. Ferrari, J. Robertson, *Physical Review B* **61**, 14095–14107, ISSN: 0163-1829 (2000).

74. J. Wagner, M. Ramsteiner, C. Wild, P. Koidl, *Physical Review B* **40**, 1817–1824 (1989).

75. M. Dresselhaus, G. Dresselhaus, A Jorio, A. G. S. Filho, R Saito, *Carbon* **40**, 2043–2061 (2002).

76. B. Balamurugan *et al.*, *Journal of Applied Physics* **92**, 3304, ISSN: 00218979 (2002).

77. Y. S. Gong, C. Lee, C. K. Yang, *Journal of Applied Physics* **77**, 5422, ISSN: 00218979 (1995).

78. R. A. Isaacs *et al.*, *Applied Physics Letters* **106**, DOI: 10.1063/1.4921263 (2015).

79. A. Ramırez-Porras, W. E. Vargas-Castro, *Applied Optics* **43**, 1508–1514 (2004).

80. G. Giovannetti *et al.*, *Physical Review Letters* **101**, 026803, ISSN: 0031-9007 (2008).

81. Z. Xu, M. J. Buehler, *Journal of Physics. Condensed Matter* **22**, 485301, ISSN: 1361-648X (2010).

82. J. M. Camacho, a.I. Oliva, *Thin Solid Films* **515**, 1881–1885, ISSN: 00406090 (2006).

83. H. J. Hagemann, W Gudat, C Kunz, *Journal of the Optical Society of America* **65**, 742–744, ISSN: 0030-3941 (1975).

84. M. D'Amore, M. S. Sarto, A. Tamburrano, F. Sarto, presented at the IEEE International Symposium on Electromagnetic Compatibility, vol. 3, pp. 900–905, ISBN: 0780393805, DOI: 10.1109/ISEMC.2005.1513653.

85. J. H. Dellinger, "The temperature coefficient of resistance of copper", tech. rep. 1, p. 71, DOI: 10.6028/bulletin.161.

86. R. Jordan *et al.*, *Applied Surface Science* **86**, 24–28, ISSN: 01694332 (1995).

87. C. R. Phipps *et al.*, *Journal of Applied Physics* **64**, 1083–1096, ISSN: 00218979 (1988).

88. W. Bao *et al.*, *Nature Communications* **5**, 4224, ISSN: 2041-1723 (2014).